

FLUORESCENT NOBLE METAL NANOCLUSTERS

A Thesis

Presented to

The Academic Faculty

By

Jie Zheng

In Partial Fulfillment

of the Requirements for the Degree

Doctor of Philosophy in Chemistry

Georgia Institute of Technology

April, 2005

Copyright 2005 Jie Zheng

FLUORESCENT NOBLE METAL NANOCLUSTER

Approved by:

Dr. Robert M. Dickson, Chairman
School of Chemistry and Biochemistry
Georgia Institute of Technology

Dr. Mostafa A. El-Sayed
School of Chemistry and Biochemistry
Georgia Institute of Technology

Dr. L. Andrew Lyon
School of Chemistry and Biochemistry
Georgia Institute of Technology

Dr. Zhong Lin Wang
School of Material science and
Engineering
Georgia Institute of Technology

Dr. Robert L. Whetten
School of Chemistry and Biochemistry
Georgia Institute of Technology

Date Approved: April 14, 2005

*dedicated to my parents for their contributions to the
society.....*

ACKNOWLEDGMENTS

I would like to thank my advisor Dr. Robert M. Dickson for bringing me to this amazing field and endless support of my research. I thank our group members, Kewei Xu, Lynn A. Pesyer, Tae-Hee Lee, Jeff Petty, Jose I. Gonzalez, Yasuko Antoku, Caiwei Zhang, Sandeep Patel for the help and friendship. I also thank my committee, Professors Mostafa A. El-Sayed, Andrew Lyon, Zhong Lin Wang, Robert L. Whetten for exciting discussion and great support of my research. I also would like thank Professor Zhenan Bao (Stanford) and Professor Yih-Ling Tzeng (Emory) for the support of my research and career. I also thank my friends Puxian Gao, Dr. Yong Ding and Qian Luo for the assistance of experiments.

Finally and also most importantly, I would like to thank my family - my parents, my brother and my lovely wife Yanping for their endless support and love. My life is fascinating because of them.

TABLE OF CONTENTS

ACKNOWLEDGEMENTS	iv
LIST OF TABLES	ix
LIST OF ILLUSTRATIONS	x
SUMMARY	xiii
CHAPTER I. INTRODUCTION	1
1.1 Motivation	1
1.2 Free electron model	3
1.3 Metallic optical responses at different size scales	5
1.4 Electronic structure of noble metals	7
1.5 Optical response of alkali metal clusters and Jellium model	9
1.6 Optical response from noble metal clusters	13
1.6.1 Absorption and emission of silver clusters	13
1.6.2 Absorption and emission of gold clusters	15
1.7 Antibunching of photon streams out of single quantum systems	17
1.8 Raman scattering and enhancement	20
1.8.1 Selection rule of Raman scattering	21
1.8.2 Enhanced Raman scattering	22
1.8.3 Resonance Raman enhancement	22
1.8.4 Surface enhancement Raman scattering	23

1.8.5	Single molecule surface enhanced Raman scattering spectroscopy	25
1.9	References	28
CHAPTER II. EXPERIMENTAL SECTION		37
2.1	Overall experimental strategy	37
2.2	Synthesis	37
2.2.1	Fluorescent gold clusters	37
2.2.2	Large luminescent gold nanoparticles	39
2.2.3	Fluorescent silver clusters	40
2.2.4	Nonfluorescent silver nanoparticles	41
2.3	Electrospray ionization mass spectrometry	41
2.4	Transmission electron spectroscopy	43
2.5	Photon correlation spectroscopy	46
2.6	X-ray photoelectron spectroscopy	46
2.7	Fluorescence lifetime measurement	47
2.8	Dark field microscopy	49
2.9	Total internal reflection fluorescence microscopy	49
2.10	Single molecule excitation spectroscopy	51
2.11	Single molecule fluorescence/Raman spectroscopy	54
2.12	Single molecule photon antibunching	54
2.13	References	57

CHAPTER III. HIGHLY FLUORESCENT AND SIZE-TUNABLE GOLD NANOCCLUSERS 58

3.1	Introduction	58
3.2	Results and Discussion	63
3.2.1	Excitation and emission spectra of fluorescent gold clusters	63
3.2.2	Size-determination of fluorescent gold clusters	65
3.2.3	Correlation of gold cluster size and its emission	71
3.2.4	Photophysical properties of fluorescent gold clusters	77
3.2.5	Photon antibunching experiments for single Au ₂₃ clusters	82
3.3	Conclusion	86
3.4	References	87

CHAPTER IV. LUMINESCENT GOLD NANOPARTICLES 93

4.1	Introduction	93
4.2	Results and discussion	95
4.2.1	Synthesis	95
4.2.2	Size characterization with transmission electron microscopy	97
4.2.3	Size characterization with photon correlation spectroscopy	101
4.2.4	Photophysical properties of luminescent gold nanoparticles	102
4.2.5	Average oxidation states of gold atoms in the luminescent gold nanoparticle determined by XPS studies	106
4.2.6	Reducing luminescent gold nanoparticles	107
4.3	Conclusion	107
4.4	References	112

CHAPTER V. FLUORESCENT SILVER CLUSTERS AND THEIR RAMAN ENHANCEMENT	116
5.1 Introduction	116
5.2 Results and discussion	121
5.2.1 Growth of fluorescent silver clusters with photoactivation method	121
5.2.2 Comparison of fluorescent silver clusters and nonfluorescent silver nanoparticles	122
5.2.3 Size characterization of fluorescent silver clusters with ESI mass spectrometry	124
5.2.4 Fluorescence spectra of dendrimer encapsulated silver nanoclusters	125
5.2.5 Excitation spectra of fluorescent silver clusters	129
5.2.6 Creating red emitting silver clusters with HeNe laser photoactivation	133
5.2.7 Raman enhancement by fluorescent silver clusters	135
5.2.8 Stokes Raman spectra of single dendrimer encapsulated silver clusters	135
5.2.9 Anti-stokes Raman spectra of red emitting silver clusters	139
5.3 Conclusion	142
5.4 References	144
CHAPTER VI. FUTURE WORK AND OUTLOOK	151
APPENDIX	
List of publications	153
VITA	155

LIST OF TABLES

Table 3-1	Photophysical properties of PAMAM-encapsulated gold nanoclusters in water	80
-----------	---	----

LIST OF ILLUSTRATIONS

Figure 2-3-1	ESI mass spectrum of dendrimer PAMAM G2-OH	44
Figure 2-3-2	Correlation of G2-OH mass abundance with its concentration in aqueous solutions	45
Figure 2-8-1	Schematic of the dark field setup on an inverted microscope	48
Figure 2-9-1	Total internal reflection geometry through a microscope objective	50
Figure 2-10-1	Schematic of the setup for measuring single molecule excitation spectra of fluorescent silver clusters.	52
Figure 2-11-1	Schematic of the setup for measuring single molecule fluorescence /Raman spectra of the silver clusters.	53
Figure 2-12-1	Hanbury-Brown and Twiss experimental setup for antibunching of gold clusters (Au ₂₃) fluorescence.	56
Figure 3-2-1	Excitation and emission spectra of dendrimer encapsulated gold nanoclusters in water	66
Figure 3-2-2	Emission spectra of octadecanethiol encapsulated gold nanoclusters in chloroform	67
Figure 3-2-3	Fluorescent nanocluster size determinations.	69
Figure 3-2-4A	Correlation of the number of atoms, N, per cluster with emission energy	73
Figure 3-2-4B	Schematic of size-dependent surface potentials of gold clusters on the different size scales.	74
Figure 3-2-5	Measurement of photon correlations on individual gold Au ₂₃ nanoclusters and the ensemble of gold clusters	85
Figure 4-2-1	Luminescence images of glutathione encapsulated	

	gold nanoparticles	96
Figure 4-2-2	TEM measurements on the luminescent gold nanoparticles	98
Figure 4-2-3	A lattice image of a single red emitting gold nanoparticle	100
Figure 4-2-4	Absorption spectra of yellow and red emitting gold nanoparticles in aqueous solutions.	103
Figure 4-2-5	Excitation spectra and emission spectra of yellow and red luminescent gold nanoparticles	104
Figure 4-2-6	Lifetime measurement of luminescent gold nanoparticles	105
Figure 4-2-7	XPS spectra of Au 4f Binding energies of glutathione- encapsulated luminescent gold nanoparticles	109
Figure 4-2-8	Absorption spectra of yellow emitting gold nanoparticles before and after adding NaBH ₄ into the solution	110
Figure 4-2-9	A TEM image of reduced yellow emitting gold nanoparticles	111
Figure 5-2-1	Time-dependent photoactivation of aqueous dendrimer-encapsulated silver nanodots and single silver nanoclusters emission patterns on the surface.	123
Figure 5-2-2	Comparison of fluorescence images and absorption spectra of dendrimer encapsulated fluorescent silver clusters and nonfluorescent silver nanoparticles	126
Figure 5-2-3	Electrospray ionization mass spectrum of photoactivated G2-OH PAMAM (MW: 3272 amu) – AgNO ₃ solution	128
Figure 5-2-4	Room temperature single cluster fluorescence spectra from different individual silver clusters and their Photostability	130
Figure 5-2-5	Excitation spectra of fluorescent silver clusters	131
Figure 5-2-6	Fluorescence image and the bulk fluorescence spectrum of the peptide encapsulated red emitting silver nanoclusters	134

Figure 5-2-7	Room temperature fluorescence and Raman spectra from different individual dendrimer encapsulated fluorescent silver nanoclusters	136
Figure 5-2-8	Room temperature bulk Stokes Raman spectra from dendrimer/peptide encapsulated red emitting silver clusters	138
Figure 5-2-9	Room temperature bulk antistokes Raman spectra from dendrimer/peptide encapsulated red emitting silver clusters	140
Figure 5-2-10	Power dependence and a possible mechanism of enhanced antistokes Raman scattering observed by red emitting silver clusters	141

SUMMARY

This thesis focuses on creating water-soluble fluorescent metallic clusters at sizes comparable to the Fermi wavelength of an electron (~0.5 nm for gold and silver) and investigating their photophysical properties at the bulk and single molecule levels.

We employed biocompatible dendrimer and peptide to prepare a series of strong fluorescent gold and silver clusters with chemical or photo reduction methods. Facilitated by the well-defined dendrimer size, electrospray ionization mass spectrometry indicates that the fluorescent silver nanocluster size ranges from 2 to 8 Ag atoms. This method also enabled the direct assignment of the 385nm (Au₅), 455nm (Au₈), 510 nm (Au₁₃), 760 nm(Au₂₃), and 870 nm(Au₃₁) emitting gold species encapsulated within the PAMAM dendrimer scaffold (“Au nanodots”).

The correlation of emission energy with the number of atoms, N, in each gold nanocluster is quantitatively fit for the smallest nanoclusters with no adjustable parameters by the simple scaling relation of $E_{\text{Fermi}}/N^{1/3}$, in which E_{Fermi} is the Fermi energy of bulk gold. Identical to that for gas phase alkali metal nanocluster electronic absorptions, the transition energy scaling inversely with cluster radius indicates that electronic structure can be well described with the spherical jellium model and further demonstrates that these nanomaterials are “multi-electron artificial atoms”. Fluorescence from these small metal clusters can be considered protoplasmonic, molecular transitions of the free conduction electrons before the onset of collective dipole oscillations occurring when a continuous density of states is reached. In

addition, very strong single molecular Stokes and Antistokes Raman enhancement by fluorescent silver clusters was observed.

Pushing to larger sizes, we also created ~ 2 nm diameter glutathione encapsulated luminescent gold nanoparticles. Distinct from similarly sized but nonluminescent gold nanoparticles, these 2 nm gold nanoparticles show bright, long lifetime emission but no plasmon absorption. The emission might arise from charge transfer between gold atoms and the thiol ligand.

Providing the “missing link” between atomic and nanoparticle behavior in noble metals, these highly fluorescent, water-soluble gold and silver nanoclusters offer complementary transition energy size scalings at smaller dimensions than do semiconductor quantum dots. The unique discrete excitation and emission and strong Stokes and antistokes Raman enhancement coupled with facile creation in aqueous solution open new opportunities for noble metal nanoclusters as biological labels, energy transfer pairs, and other light emitters in nanoscale electronics.

CHAPTER 1

Introduction

1.1 Motivation

Noble metals exhibit a particularly wide range of material behavior along the atomic to bulk transition.^{1,2} While high conductivity and beautiful surface luster are generally accepted as the characteristics of bulk noble metals, the beauty of metals on the nano scale is far more than imagined¹⁻⁴. Motivated by the complete understanding and manipulation of size-dependent properties, researchers have intensively investigated noble metals in different size domains for many decades.¹ Among these investigations, the study of few-atom metal clusters has attracted great interest because they bridge the evolution of properties from isolated atoms to nanoparticles and even to the bulk.⁵⁻¹⁰

According to the number of metal atoms, nanoscale metals are roughly classified into three size domains: large nanoparticles, small nanoparticles and clusters, corresponding to three different characteristic length scales respectively.^{1,11} The first characteristic length scale encountered in shrinking from bulk to nanoparticles is the wavelength of light. Optical responses of large metal nanoparticles ($R \approx \lambda$) to external electromagnetic fields are simply dependent on their sizes, free electron density and therefore their dielectric function relative to that of the surrounding medium. This size-dependent effect is extrinsic because optical

properties such as dielectric functions (i.e. refractive indexes) of the nanoparticles are similar to those of bulk metals¹. These optical properties can be quantitatively described with Mie theory proposed in 1908 for small metallic spheres¹. Applying Maxwell's equations with appropriate boundary conditions in spherical coordinates, Mie found that optical absorption, light scattering and extinction of a metal sphere depend on its volume and bulk dielectric functions.^{1,2} When particle size approaches the second characteristic length, electron mean free path (the average distance an electron travels between two adjacent collisions, and ~50 nm for gold and silver),¹¹ the dielectric function and refractive indices become size dependent. As a result, the optical responses such as plasmon absorptions of small metal nanoparticles ($R \ll \lambda$) have different size-dependences compared with large nanoparticles. This is an intrinsic or quantum size effect,^{1,11} but Mie theory still can be extended into this quasi-static regime. Eventually, when particle size becomes comparable to the third characteristic length- Fermi wavelength of an electron (i.e. de Broglie's wavelength of an electron at the Fermi energy, or ~0.5 nm for gold and silver),^{2,12,13} optical, electronic and chemical properties of metal clusters are dramatically different from the other two size regimes. In this smallest size regime, metal clusters become "molecular species",¹⁴⁻¹⁶ and discrete states with strong fluorescence can be observed.^{6,9,10,17-22} It is these molecule-like properties of such few atom metal clusters that is the primary topic of this thesis.

In this thesis, I attempted to to answer fundamental questions regarding these molecular clusters by creating a series of fluorescent gold and silver clusters and

investigating their photophysical properties at the bulk and the single molecule level. Providing the “missing link” between atomic and nanoparticle behavior in noble metals, these highly fluorescent noble metal nanoclusters smoothly link the optical and electronic structure transitions from atoms to nanoparticles with observable free electron behavior and also offer new opportunities for creating new biological labels, energy transfer pairs, and other light emitting sources in nanoscale electronics.

1.2 Free electron model

In 1900, Drude successfully applied the kinetic theory of gases to explain the electrical and thermal conduction of metals with three assumptions to account for electron densities and interactions of metals being much greater than those of classical gases.^{1,11} These assumptions are: (1) The interactions of a given electron with others and with ions are neglected between collisions. (2) Electron-electron scattering is neglected. (3) Electrons experience a collision probability per unit time of $1/\tau$, where τ is the interval between two adjacent collisions. In the Drude model, the valence electrons of metals were considered free electrons due to strong electron screening effects. These free electrons are delocalized in the bulk metals and do not belong to any specific metal atoms. As a result, free electrons move in the constant potential field provided by the positively charged cores. The total Hamiltonian of a metal can be written as the sum of “non-interacting” Hamiltonians of free electrons, which is also called the “one particle” approximation. Although the free electron model was originally proposed based on the kinetic theory of molecular gases, the

dramatic difference between these two systems is that the energy levels are not quantized in a molecular gas while they are quantized in metals due to the Pauli exclusion principle.^{11,23} As a result, the energy of an electron system is enormously larger than that of a molecular gas system.

Based on the one-particle approximation, the effective Hamiltonian for an electron can be considered as a free electron moving in a constant potential field.^{11,23} Consequently, a simple particle in a box model is used to describe the behaviors of the free electrons in metals. The energy levels of metals can be simply written as

$E = \frac{n^2 h^2}{2mL^2}$ based on the one particle in a box model, where n is the principle quantum number, E is the energy of a quantized level, L is the size of a metal, m is electron mass, h is Planck's constant. The boundary conditions for this box are the lengths of metals. However, since the metals have periodic crystal structures in the bulk states, boundary conditions in the bulk metals can be of any length as long as properties of metals are size-independent. Only on the nano scale, is the box size dependent on the particle size. This simple model sheds light on how the free electrons pile up in the metals. In a given metal, since each energy state could have different degeneracy, the number of the free electrons will be piled up at the rate of as many electrons per level as permitted by its degeneracy until all the electrons are exhausted.^{11,23} For example, while only 2 electrons are allowed in the lowest energy state, 6 electrons are allowed in the second lowest energy level because of degeneracy increasing. The topmost filled level corresponds to the highest electron

energy of a given metal, called the Fermi energy E_f , which is independent of the metal size. Quantized energy states and large Fermi energies are characteristic of an electron gas, thereby making them distinct from the more familiar molecular gas.

1.3 Metallic optical responses at different size scales

The optical response of free-electron metals in the bulk state is well described by Drude-Lorentz-Sommerfeld / free electron model.^{1,11} Based on this model, the macroscopic optical response of metals follows by summing the single electron response over the total number of the free electrons. Thus, according to this model, all the free electrons in a metal react in phase with the electrical field.^{1,11} In reality, due to the large electron density and delocalization, all the free electrons indeed coherently oscillate under a time dependent electrical field, which gives the well-known bulk plasmon absorption. The frequency of bulk plasmon can be written as^{1,11}

$$\omega_p = \left(\frac{4\pi n e^2}{\epsilon_0 m_e} \right)^{1/2} \quad [1]$$

where ϵ_0 is the dielectric constant of vacuum, m_e is the effective electron mass, and n is the electron density of the bulk metal. The dielectric “constant” of a metal is a function of the frequency of the external electrical field. Its real and imaginary parts, respectively, can be written as^{1,11}

$$\epsilon_R \approx 1 - \frac{\omega_p^2}{\omega^2} \quad [2]$$

$$\epsilon_i \approx 1 - \frac{\omega_p^2}{\omega^3} \Gamma \quad [3]$$

in which ω_p is the Drude plasma frequency and the relaxation time constant Γ ($\Gamma = 1/\tau$, τ is relaxation time) is related to the electron mean free path l by $\Gamma = v_f/l$, where v_f is the average speed of an electron at the Fermi energy. When ω is larger than ω_p , the metal becomes transparent and radiation can propagate without absorption.

When metal nanoparticle size is comparable to the light wavelength, plasmon absorption becomes size-dependent although the metallic dielectric functions remain nearly equal to those of the bulk. The free electrons in the large nanoparticles have different oscillation modes toward the time-dependent electrical field of the light. The optical response of the metal nanoparticles is the summation of all the different plasmon frequencies resulting from dipole and higher order oscillation modes,¹

$$\omega_1 = \left(\frac{\omega_p}{\sqrt{1 + \frac{L+1}{L} \epsilon_m}} \right) \quad [4]$$

in which ω_p is the volume plasmon frequency of a bulk metal. L is the oscillation mode, L is equal to one for dipole oscillation, and two for quadrupole oscillation. ϵ_m is the dielectric constant of an embedding material. When the diameters of metal nanoparticles are larger than their mean free paths, not only dipole oscillation but also the higher-order multipole oscillations are allowed. The plasmon positions of metal nanoparticles can be calculated with Mie theory. Assuming that ϵ_m is 1 in vacuum, for a spherical metal nanoparticle, its surface plasmon frequency is $\omega_p/\sqrt{3}$ because L is

equal to 1. Qualitatively, the larger the metal nanoparticle is, the lower its surface plasmon absorption frequency. Conduction electrons in a spherical nanoparticle act like an oscillator system, whereas in bulk metals they behave like a relaxator system to dissipate energy.¹ The displacement of negative charges due to an electric field gives rise to polarization charges at the nanoparticle surface and hence to a linear restoring force between electrons and positive charges.¹

When metal nanoparticle sizes become much smaller than the electron mean free path, a monotonic absorption transition with size is observed because absorption is mainly due to dipole oscillation mode while higher order oscillations contribute much less to the overall oscillation strength.²⁴ Both the absorption frequency and the absorption linewidth have simple size-dependences. For silver nanoparticles (with diameter 2 nm <D<10 nm) embedded in an argon matrix, absorption linewidths Γ and frequency $h\omega_s$ are quantitatively related to silver particle diameter D.²⁴ With decreasing silver particle size, the bandwidth increases and the plasmon position is blue shifted, as described by the empirical relations :

$$\Gamma / eV \approx 0.04 + \frac{0.59}{D / nm} \quad [5] \quad h\omega_s / eV = 3.21 + \frac{0.58}{D / nm} \quad [6]$$

1.4 Electronic structure of noble metals

Although optical responses of metals and metal nanoparticles are strongly size-dependent, metallic band structure is only weakly size-dependent. Bulk metals have continuous band structures and the conduction bands are occupied with free

electrons. Such band structure is also observed from metal nanoparticles larger than 2 nm, in which the density of states is large enough and energy level spacings between adjacent quantum states are much smaller than thermal energy.²⁴ Thus, these delocalized free electrons coherently oscillate and give the well-known surface plasmon absorption. Differences in size-dependent optical response mainly arise from the change in the number of free electrons.

When metal nanoparticle size approaches the Fermi wavelength, the continuous band structures of metals break up into discrete energy levels. In 1964, Kubo produced quantitative predications on the electronic structure of very small metal clusters based on the recognition that quasi-continuous electron energy states of bulk metals become discrete on the few-atom scale.²⁵ The energy level spacing between adjacent levels for an N-atom particle is on the order of E_f/N , where E_f is the Fermi energy of the bulk metal. The relative difference between the energy level spacing and thermal energy has become a criterion to distinguish metallic conduction from insulation.²⁶ If the energy level spacings are smaller than thermal energy, thermal energy can create mobile electron-hole pairs in the metals. As a result, current can flow through the metal.²⁶ However, if the energy level spacings are much larger than the available thermal energy, the free electrons in the metal clusters are confined to discrete energy levels. Thus, the metal clusters are often considered to be nonmetallic. Although Kubo et al. predicted some properties of metal cluster electronic structure; the quantitative correlation of electronic structures with the number of atoms in metal clusters was not discovered until 1984.²⁷

1.5 Optical response of alkali metal clusters and Jellium model

Knight and co-workers observed a periodic pattern of intense peaks in the mass spectra of alkali metal clusters Na_N , indicating that Na clusters with $N=2,8,18,20,40,58$ have greater stability than do others.²⁷ This magic pattern in stability can be rationalized with a simple quantum mechanical model called the jellium model, which originates from nuclear physics.^{24,27-29} Due to a strong electron screening effect, valence electrons of noble metal atoms are considered free electrons after neglecting electron-electron and electron-ion interactions. In this model, a metal cluster is modeled by uniform, positively charged spheres with electronic shells filled with free electrons. These free electrons are provided by the valence electrons of alkali atoms, and they delocalize and form spherical electron shells surrounding the positively charged core. Distinct from electronic structure of single atoms, cluster electron density is independent of the number of free electrons in the metal clusters. However, analogous to single atoms, free electrons in metal clusters are also delocalized for electronic shells surrounding the atoms and subject to the Pauli Exclusion Principle. The quantized shells can be described by a simple 3D harmonic oscillator.^{24,27-29} Due to the nature of the cluster spherical potential, the solutions of the Schrödinger equation are very similar to those of single atoms. Similarly, these free electrons form quantal shells surrounding the positively charged cores. Although jellium orbitals are labeled in the similar way as are with atomic orbitals, the principle quantum number n of Jellium orbitals is different to that n_{atom} of atomic orbitals and has such relation, $n = n_{\text{atom}} - l$, where l is the angular momentum quantum number.²⁴ In

addition, it should be noted that angular momentum is not restricted by the principal quantum number n . As a result, 1s, 1p, 1d, 2s, 1f, 2p, ... are observed in the electronic structure of alkali clusters because of potential surface differences between clusters and atoms. For example, an electron in hydrogen atom is in a $-r^{-1}$ potential, while an electron in a metal cluster is in the spherical harmonic oscillator r^2 potential. As a result, for a given shell n ,²⁴ the magic numbers for the r^{-1} potential are following the equation 7

$$N_0 = \frac{2}{3}n(n + \frac{1}{2})(n + 1) \quad [7]$$

and 4,10, 18..., corresponding to 1s, 2s, 2p, 3s, 3p, 3d.... electronic shells. while the magic numbers for the harmonic oscillator are following the equation 8 and are 2,8,18,20..., corresponding to 1s, 1p, 1d, 2s,.... electronic shells.:

$$N_0 = \frac{1}{3}(n + 1)(n + 2)(n + 3) \quad [8]$$

The harmonic energy level spacing ω_0 in a spherical harmonic oscillator potential is dependent on the Wigner-Seitz radius r_s and the number N of free electrons in the clusters as shown in equation 9²

$$\hbar\omega_0 = 3.61 \cdot \frac{\hbar^2}{2\mu r_s^2} (N)^{-\frac{1}{3}} \quad [9]$$

Fundamentally, the jellium model is the Drude free electron model and contains the same assumptions. The magic sizes observed in the alkali clusters are due to the complete filling of the different energy shells. For example, in Na₈ cluster, each Na atom donates one valence electron, and these free electrons are delocalized to form electronic shells surrounding the positively charged core composed of Na atoms. Eight free electrons completely fill the 1s and 1p energy states forming a complete valence shell, thereby making Na₈ very stable. The next stable size is Na₁₈, resulting from filled 1d energy state. Due to the similarity in electronic structure between metal clusters and single atoms, these metal clusters can also be called “multielectron” artificial atoms.^{24,27-29}

Since the number of the free electrons are piled up in the metal clusters with constant electron density, Fermi energies of “free electron” metals only depend on the electron density ρ_0 or the Wigner-Seitz radius (r_s) of the metals as shown in equation

10

$$E_f = \frac{p_f^2}{2\mu} = \frac{(3\pi^2\rho_0)^{2/3}}{2\mu} = \left(\frac{9\pi}{4}\right)^{2/3} \frac{\hbar^2}{2\mu r_s^2} \quad [10]$$

By combining equations 9 and 10, a very simple relation of frequency and Fermi energy can be derived (Equation 11).^{24,27-29}

$$\hbar\omega_0 \cong E_f (N)^{-1/3} = E_f r_s / R \quad [11]$$

This simple equation gives a quantitative explanation of how the electronic structures of alkali clusters changes with the number of free electrons. Energies of ground states as well as those of different excited states can be predicated with this equation.

Electronic shell structure was observed not only in the alkali metal clusters, but also in other metals. For example, Rademann and coworkers found that the ionization energies of Hg_n clusters increase with decreasing size, and roughly follow $1/R$ law.³⁰ The Knight group also discovered that the ionization potential of potassium clusters K_N ($N < 100$) has $1/R$ size-dependence.³¹ Skala et al. also observed this $1/R$ dependence in the binding energies of Li clusters.³² Many gas phase optical studies of alkali metal clusters have yielded the further important insights into alkali metal nanocluster structure. For example, Haberland et al. studied optical spectra for Na^+_n clusters with $3 \leq n \leq 64$ at 105 K. For small cluster size ($n=3-9$), single and well separated electronic transitions were clearly observed.³³ When the cluster size increases ($n=10-15$), the number of electronic transition lines increase and electronic transitions start to overlap. An additional and broad absorption started to show on the high energy side of the absorption spectra in the larger Na clusters.³³ This high energy absorption is the volume plasmon absorption of Na clusters rather than the often invoked interband transition (see below). This important set of studies clearly indicated strong size-dependent transitions from single electron resonance to collective plasmon oscillation in few atom Na clusters.

1.6 Optical response from noble metal clusters

1.6.1 Absorption and emission of silver clusters

The transition in optical absorption of the atomic to cluster to bulk silver was investigated by Kreibig in 1974.³⁴ Similar to alkali clusters, discrete electronic transitions instead of a collective plasmon were observed from these very small silver metal clusters at low temperature. In 1978, Ozin and Huber used cryophotoclustering technique to prepare a series of small silver clusters Ag_n (where $n < 6$) within Ar matrices at 20 K and attempted to bridge the molecular metal cluster-bulk metal microcrystalline interface by investigating the correlation of absorption with cluster size.⁵ Single silver atoms show strong optical absorption at 3.8 eV, and with increasing size, more discrete absorption bands between 3.1 and 4.1 eV were observed from few atom silver clusters at low temperature.⁵ When the silver cluster size, N , is larger than 40, these discrete absorption bands vanish and plasmon absorption becomes the dominant optical transition.³⁴ As a result, Ag_{40} is the lower limit for optical behavior corresponding to silver nanoparticles.³⁴ Later, with assistance of “soft landing” mass spectrometry, Harbich and coworkers were able to prepare size selected silver dimers and trimers in solid Kr matrices, and investigated their absorptions and fluorescence.^{22,35-37} A silver dimer gives rise to excitation bands centered at 271, 281, 390 and 407 nm and strong emissions at 288 and 479 nm. Ag_3 clearly shows absorptions at 331, 364, 402, 421, 458, and 514 nm and had discrete emissions at 374, 616 and 705 nm. Distinct from the plasmon of large silver nanoparticles, discrete electron transitions clearly indicates that these few atoms

exhibit molecular behaviors.^{22,35-37} Further studies on silver clusters showed that silver tetramer gave the emission at 458 nm³⁸, while Ag₈ gave emission at 394 nm as reported by Rabin et al.¹⁹ In 1998, Chen and coworkers used zeolites to prepare fluorescent silver clusters at room temperature.⁶ Complementary to the studies on isolated silver clusters, our group discovered that these same fluorescent silver clusters can be produced by photoreducing silver oxide films. The multicolored emission from silver clusters are easily observed at the single molecule level even under very weak mercury lamp excitation, thus offering a unique opportunity to apply these fluorescent silver clusters as biological labels or active materials in optoelectronics.^{7,39,40} Emission observed from these few atom silver clusters is due to discrete electronic transitions likely confined by cage effect. Solid Kr matrices,^{22,35-37} zeolites,⁶ or silver oxides^{7,39,40} increase cross section of irradiative decay and prevent dissociation of silver clusters, even though the excitation energies are comparable to the photodissociation energies of naked silver clusters. Atom and dimer loss are a general phenomenon for photodissociation of s-electron naked metal clusters.²⁸ For example, Ag₉⁺ under 308 nm irradiation fragments into equal proportions of Ag₇⁺ and Ag₈⁺.⁴² Hild and coworkers⁴³ found that after excitation by photons with energies 1.5~4 eV, silver clusters decay by emission of neutral atoms or dimers with lifetimes in the range 100 μs to 15 ms. Photodissociation energies are also size-dependent. For example, Kruckeberg and coworkers discovered that dissociation energies of Ag_N (N=2-25) are in the range of 1 to 3 eV, and are strongly influenced by the electronic close shell and odd-even effects.⁴⁴⁻⁴⁶ While either solid gas or inorganic matrices can

protect silver clusters from photodissociation, the large excited state charge separation is also a possible process in the photophysics of few atom silver clusters.

1.6.2 Absorption and emission of gold clusters

Marcus and Schwentner first observed that gold dimers yield 450, 545 and 580 nm emission in 1987.⁴⁷ Harbich et al. also used a similar method to prepare Au₂, and Au₃ embedded in argon matrices and studied their optical response at low temperature.^{21,35,48} Gold dimer shows absorptions at 209, 246, 305 and 357 nm and emissions at 285, 325, 742 and 757 nm. Absorptions centered at 231,258,285,302 457 and 511 nm and emission centered at 529, 579 and 809 nm were observed from Au₃. Collings et al also investigated the gas phase optical absorption spectra of gold clusters Au_N (N=7,9,11,13) using photodepletion spectroscopy.⁴⁹⁻⁵¹ Sharp lines between 1.9 and 5.6 eV in absorption bands were observed.⁴⁹⁻⁵¹ In addition, a pronounced odd-even alternation in the mass spectra of gold clusters indicated that Au cluster stability may follow a simple electron pairing scheme, which is in contrast to the jellium model.⁵⁰

Gold clusters are also highly stable at ambient conditions. Schmid and coworkers created Au₁₁ Au₁₃, Au₅₅ in solution phase with the assistance of organic ligands.⁵²⁻⁵⁷ Electronic transitions between 1.6 eV and 4.0 eV were observed from their absorptions. Au₅₅ is especially interesting because of its remarkable chemical stability. The extraordinary stability of Au₅₅ is due to its almost perfect close packing cuboctahedral structure.⁵² High stability of other gold clusters such as Au₁₃ and Au₁₄₇ are also because they have closed atomic shells. This “Chemical selection” in the

solution phase avoids having an arbitrary number of atoms in a particle, which is also a very important factor in determining the magic sizes of gold clusters under ambient conditions.^{52,58} The optical spectra of Au₅₅ appear to be rather structureless, neither showing a collective excitation resonance nor exhibiting distinct absorption bands known from few-atom clusters, possibly bridging transition from discrete energy levels to collective oscillations.^{52,56,57,59,60}

Fluorescence was also observed from Au clusters in the solution phase. In 1998, Wilcoxon et al observed blue emission at 440 nm from small gold nanoparticles (Diameter < 2.5 nm),⁶¹ however, due to the heterogeneity of the solution, the exact size of emissive species was not able to be identified. The Whetten and El-Sayed groups observed near IR emission from glutathione encapsulated Au₂₈ clusters in aqueous solution.⁹ Compared to well-studied alkali clusters,^{27,31} the size-dependent electronic structure of these noble metals remains poorly understood.

As discussed above, optical properties such as the plasmon absorption of noble metal nanoparticles can be well explained with the free electron model on different length scales. A fundamental question is whether this model which nicely explains the properties of large noble metal nanoparticles and small alkali clusters can be used in interpretation of optical properties of few atom noble metal clusters. Although the electronic structure of noble metal clusters remains unclear at ambient conditions, free electron behavior has recently been observed from gold nanowires at low temperature.⁶² Ho and coworkers recently studied the energy levels of few atom gold nanowires on a NiAl substrate at cryogenic temperatures with scanning tunneling

microscopy.⁶² Results indicated that the electronic properties such as conductance of one-dimension gold cluster chains were determined by the number of free electrons in the chains. Each gold atom in the chains only donate its 6s electron, and these valence electrons are delocalized in the whole chain because strong electron screening effect due to core electrons and d electrons. On the Fermi wavelength scale, 5d electrons of gold clusters are more tightly bound by the nucleus than are 6s electrons. As a result, there is also a large energy gap between the s band and the d band, and d electrons have little perturbation on the conduction band structure of few-atom gold clusters.⁶² Currently two possible mechanisms could be used to explain the observed emission from these small metal clusters. One is due to intraband (sp/conduction band) transition. The other is interband (d-sp) transition. In this thesis, fluorescence is utilized as a signature of electronic structure to explore the fundamental physics of these few -atom noble-metal clusters and their lowest lying electronic levels.

1.7 Antibunching of photon streams out of single quantum systems

When conduction electrons become sufficiently dense, noble metals behave as free electron gases which can collectively oscillate under time dependent electrical fields.^{1,2} Base on the one-particle approximation, a macroscopic response of metals is the sum of single electron responses over the total number of free electrons. When incident light passes through the bulk metal or metal nanoparticles, time-dependent electrical fields induce oscillation of free electrons in the metal, and scattered photons result from this oscillation. When metal nanoparticle size approaches the Fermi

wavelength of the electron, free electrons are confined in discrete energy levels. Because these energy level spacings are large relative to thermal energy, these metal nanoclusters should behave as single quantum systems, not the sum of many quantum systems. Because any individual quantum system can only emit one photon at a time, time correlation of photon pair arrival times or photon antibunching experiments can demonstrate quantum nature of the emitter. Only a single quantum system can provide a true nonclassical single-photon source with zero probability of two photons being simultaneously detected (i.e. “Antibunched” photons).

Photon antibunching in the fluorescence was first observed in dilute atomic beams at low temperature in 1977,⁶³ and later in single molecules in cryogenic molecular crystals. Michler et al and Santory et al demonstrated single photon devices using pulsed laser excitation of a single AlGaAs quantum dot.^{64,65} Single dye molecules embedded at low concentration within organic single-crystal platelets or covered by a polymer layer were also used as single photon sources at room temperature.⁶⁶⁻⁶⁸ However, for most organic dyes, photostability strongly limits their practical applications in quantum communications and quantum computing.

Currently, inorganic materials such as semiconductor quantum dots⁶⁹⁻⁷³ and color centers in diamond⁷⁴ are promising candidates for single photon sources because they are highly robust photoemission. Michler and coworkers performed the photon correlation measurements on single CdSe quantum dots at room temperature, which not only provided direct evidence that single quantum dots behave as solid-

state non classical light source but also prove that single quantum dots act like artificial atoms.^{64,65,75} Gruber et al. and Brouri et al. also studied the photon correlation of fluorescence of individual nitrogen-vacancy defect centers in diamond at room-temperature and found that these individual defects centers with the excited state lifetime around 11.5 ns behave as single quantum systems.⁷⁶ However, very long lifetimes of these quantum systems limit producing efficient photon antibunching characteristics. As a result, developing novel nanomaterials with strong photostability and short lifetimes can overcome current disadvantages in single photon source applications.

Photon correlation measurements are usually carried out by combining a Hanbury- Brown-Twiss photon-coincidence set up with a optical microscope.^{63-66,68-70,73,74,76-85} Such experiments measure a likelihood that second photon will be detected at time $t+\tau$, given an initial photon detection event at time t . Fluorescence from a single emitter is divided into two parts by a beam splitter, which is then detected by two single photon counting avalanche photodiodes (APDs). Each detector will generate a voltage pulse upon detection of a single photon. The pulses from the APDs are used to start and stop a time-to-amplitude converter, which translates the time delay between two photons into voltage differences. As a result, the number of photon pairs $n(\tau)$ with different interval time τ will be recorded. $n(\tau)$ is proportional to the normalized intensity correlation function $g^{(2)}(\tau)$

$$g^{(2)}(\tau) = \frac{\langle I(t)I(t+\tau) \rangle}{\langle I(t)^2 \rangle} \quad [12]$$

If $g^{(2)}(0)$ at zero delay is equal to 1, the photons are completely uncorrelated. If $g^{(2)}(0)$ is smaller than 1, this indicated that two photons are unlikely to appear simultaneously at the detectors with zero time delay. Intensity correlation of emitted light from a single two level quantum system should be exactly zero, indicating a strong quantum correlation between the photons.⁸⁴ Assuming that at $t=0$ one photon is detected, and the system can not emit a second photon until the system is re-excited into the excited state. As a result, $g^{(2)}(0) \approx 0$. if the detector time resolution is much faster than the excited state lifetime, the lifetime of the emitter can be determined under CW laser excitation based on the equation $g^{(2)}(\tau)=1-(1/N)e^{-\tau/t_d}$,⁶⁴ where t_d is decay time and N is the number of independent emitters under ideal background-free conditions. Photon antibunching $g^{(2)}(\tau) < 0.1$ is considered as the direct evidence that the source of the radiation field is a single emitter quantum system. However, because contrast quantum correlation is quickly lost due to the detector time resolution, background scattering, long fluorescence lifetime, and biexciton emission,⁶⁴ $g^{(2)}(\tau)$ s for most of known quantum systems such as single quantum dots,⁶⁴ color centers,⁷⁶ and dyes,⁷⁷ are nonzero. Thus for efficient and practical use of single quantum systems, thus it is very necessary to create new fluorophores with short lifetime, high photostability and strong emission.

1.8 Raman scattering and enhancement

When light interacts with molecules, the predominant mode of scattering is Rayleigh scattering due to elastic collisions between photons and molecules.^{86,87} The

intensity of Rayleigh scattering increases with the fourth power of the light frequency. Scattered photon can alternatively increase or decrease their energies due to inelastic scattering from the molecules. If frequencies of this Raman scattered light are lower than the incident frequency, “Stokes-shift” lines are observed, corresponding to the vibration energy shifts from the incident light frequency. Consequently, photons scattered to higher energy are called anti-Stokes lines.^{86,87} Like Rayleigh scattering, Raman scattering strongly depends upon the molecular polarizability. For polarizable molecules, the incident photon energy can excite vibrational modes of the molecules, yielding scattered photons that are modulated by the molecular vibrational transition energies.

1.8.1 Selection Rule of Raman Scattering

Since Raman scattering is dependent on the linear polarizability of a molecule, the transition moment integrals are of the form

$$\int \psi_v^i \alpha \psi_v^f d\tau \quad [13]$$

Where α represents the linear polarizability of the molecule, and within a Harmonic Oscillator picture, nonzero transition moments only occur when initial and final vibrational states must have the same symmetry, because the symmetry of the polarizability is the same as that of quadratic terms of the Cartesian coordinates. The intensity of Raman scattering is linearly dependent on the square of induced dipole moment P , which has a linear relationship with polarizability by $P = \alpha E$ where

E is a external electric field. If a vibration does not greatly change the polarizability under the electric field of the excitation light, the polarizability derivative will be near zero, and the intensity of the Raman lines is very weak. Generally, a highly polar bond such O-H has weak Raman scattering intensity, because the external electric field can not induce a large change in the dipole moment. Only when more nonpolar but electron rich bonds, such as aromatic groups, have larger induced dipole moment and stronger Raman scattering can be observed.

1.8.2 Enhanced Raman scattering^{86,87}

Since typical Raman scattering cross section is very small $\sim 10^{-30}$ cm²/molecule, high concentrations and high excitation intensity power laser are required to observe Raman scattering from materials. To overcome this intrinsic disadvantage of Raman scattering, different enhanced methods have been discovered and extensively investigated.

1.8.3 Resonance Raman Enhancement^{86,87}

If the laser wavelengths match the electronic transitions of the molecules, the Raman scattering cross sections can be increased by a factor of 10^2 - 10^4 . This effect is called Resonance Raman enhancement. Quantitatively, within the Born-Oppenheimer approximation, the resonance Raman cross section can be written as

$$\sigma_{i \rightarrow f} = 5.87 \times 10^{-19} M^4 E_s^3 E_L \left| \sum_v \frac{\langle f | v \rangle \langle v | i \rangle}{\epsilon_v - \epsilon_i + E_0 - E_L - i\Gamma} \right|^2 \quad [14]$$

in which E_S and E_L are scattered and incident photon energies, and ϵ_i and ϵ_v are energies of vibrational levels v, i of the excited and ground electronic states respectively. M is transition length. E_0 is the zero-zero energy separation between the lowest vibrational levels of the ground state and excited electronic states, Γ is the homogenous linewidth. $E_S, E_L, E_0, \epsilon_i, \epsilon_v$ and Γ are in cm^{-1} . M is in angstroms. σ is in $\text{\AA}^2/\text{molecule}$. Raman scattering has become a versatile spectroscopic technique for studying various systems, because only the vibrations of the absorbing species can be selectively enhanced.^{86,87}

1.8.4 Surface-Enhanced Raman Scattering.

Raman scattering also can be enhanced in the proximity of metallic surfaces. Early observation of surface enhanced Raman scattering was done by Fleischmann and co workers in 1973.^{88,89} Six orders of magnitude enhanced Raman signals were observed when pyridine molecules were adsorbed on silver electrodes with rough surfaces. Later, more detailed experiments were carried out to understand this surface enhancement effect. Enhancements as large as 10^9 were observed from molecules absorbed on 100-50 nm metal nanoparticles in the bulk solutions.^{86,87,90,91} This surface-enhanced Raman scattering is strongest on silver, but is observable on gold and copper as well. Surface-enhanced Raman scattering (SERS) generally are contributed from two mechanisms. The first one is due to the enhanced electromagnetic field produced by metal nanoparticles.⁹²⁻⁹⁶ When the wavelength of the incident light is close to the plasma wavelength of the metal nanoparticle, free

electrons in the conduction band of metal nanoparticles coherently oscillate, thus the local electric field is about 10^3 larger than the strength of incident electrical field, leading to overall 10^6 enhancement in Raman scattering cross sections of molecules adsorbed or in close proximity to the surface. During this surface plasmon excitation, vibrational modes normal to the surface are most strongly enhanced.

The second factor of enhancement mechanism is due to charge transfer between analyte molecule and metal surface.^{92,96-101} In 1980, McIntosh and coworkers found a pronounced optical absorption peak centered around 550 nm after dispersing silver in solid ethylene-Ar matrix at low temperature, but C_2H_4 itself has no internal electronic transitions in the visible range. In addition, only an ultraviolet absorption band instead of this charge transfer band in the visible range was observed from $Ag^+ - C_2H_4$ under the same conditions and the CT band is not observed from $Ag - C_2H_6$.¹⁰⁰ These observations suggested that this 550 nm absorption arises from charge transfer excitation of an electron from silver 5s to an unoccupied orbital of a C_2H_4 molecule. Strong Resonance Raman scattering of C-C stretching vibrational mode was observed after excitation of this charge transfer band and its intensity approximately given by $(h\omega_L - E_{CT})^2$, where ω_L is the frequency of incident light and E_{ct} is charge transfer energy. Since charge transfer happens only within a few Angstroms, this charge transfer mechanism is called short range enhancement mechanism. Fundamentally, this charge transfer mechanism is similar to Resonance Raman scattering enhancement as it creates new electronic levels close to the laser excitation frequency.

1.8.5 Single molecule Surface Enhanced Raman Scattering spectroscopy

Although surface enhanced Raman scattering can be well explained with electromagnetic field and charge transfer mechanisms in the majority of bulk studies, these two mechanisms seem insufficient to yield the extreme enhancements necessary to observe at the single molecular level. Kneipp and coworkers studied Raman scattering from a crystal violet molecule absorbed on 100 nm silver nanoparticles and directly observed single molecule Raman scattering cross section as large as 10^{-16} $\text{cm}^2/\text{molecule}$.¹⁰² Nie and Emory used cw 514 nm laser to excite single R6G molecules on silver nanoparticles and also observed enormous SERS enhancement with the same cross section as Kneipp et al. reported.¹⁰³ Both studies show the Raman scattering intensity fluctuates with time. In addition, a surprising discovery in Nie's studies is that not all the silver nanoparticles can give such large enhancement effect although they are in the same size. These magic SERS active silver nanoparticles are called "hot" nanoparticles.¹⁰³ By exploiting the properties of SERS and resonance effects, these incredible enhancements were attributed to rare surface interactions present on a very small subset of "hot" nanoparticles on the surface, or "hot spots". To generate such hot spots, a common method is introducing NaCl into silver nanoparticle solution,^{102,103} however, detailed information about these hot spots is still missing.

Compared to the overall 10^9 enhancement in Raman scattering observed from bulk studies, 10^{14} to 10^{15} enhancement observed at the single molecular level indicated that there are still unknown effects in the enhancement studies. Brus et al.

carried out detailed studies on these hot nanoparticles, and found that the giant enhancement 10^{12} may arise from the junction between two nanoparticles by combining other size characterization methods.¹⁰⁴ However, this pure physical model can not explain the quenching effect observed by Nie group.^{103,105} Thiolsulfate ions can completely destroy the SERS activity without physically changing junctions.^{103,105} These studies suggest that the chemical effect must be taken into consideration and charge transfer may also play a key role in the SERS enhancement at the single molecule level. Henglein and coworkers investigated the chemical reactivity of silver aggregates over a wide size range and found that small silver clusters have much higher chemical reactivity than the large nanoparticles.¹⁰⁶ As a result, charge/electron transfer between organic molecules and silver becomes more efficient in the small clusters than the large nanoparticles.

In addition to fluorescence and charge transfer as well as SERS enhancement, photoelectron emission process was also observed from silver nanoparticles and clusters.¹⁰⁶ Photoelectron emission from compact silver electrodes occurs with extremely small quantum yield (<0.0001), however, this yield greatly increases with decreasing size. Photoemission electron quantum yield of few-atom silver clusters can reach as high as 10%.¹⁰⁶ This dramatic change in the quantum yield is because the small clusters have lower density states in the conduction band, and photoinduced electron can more easily tunnel into the energy levels of scaffolds. Such photoinduced electron transfer might also contribute to chemical enhancement effect. While all these processes might involve in this unique large Raman enhancement, the detailed

enhancement mechanisms are still not fully understood and more work need to be done to clarify the role of small silver clusters in the SERS effect. In this thesis, Raman enhancement by fluorescent silver clusters will be investigated for better understanding and exploring the SERS effect.

1.9 References

1. Kreibig, U. & Vollmer, M. *Optical Properties of Metal Clusters* (Springer, 1995).
2. Haberland, H. *Clusters of Atoms and Molecules* (ed. Haberland, H.) (Springer-Verlag, 1994).
3. El-Sayed, M. A. Some interesting properties of metals confined in time and nanometer space of different shapes. *Accounts Chem. Res.* **34**, 257-264 (2001).
4. Whetten, R. L. et al. Crystal structures of molecular gold nanocrystal arrays. *Accounts Chem. Res.* **32**, 397-406 (1999).
5. Ozin, G. A. & Huber, H. Cryophotoclustering Techniques for synthesizing very small naked silver cluster Ag_n of known size (where n=2-5). The molecular metal cluster-bulk metal particle interface. *Inorg. Chem.* **17**, 155-163 (1978).
6. Chen, W. et al. Photostimulated luminescence of AgI clusters in zeolite-Y. *J. Appl. Phys.* **83**, 3811-3815 (1998).
7. Peyser, L. A., Vinson, A. E., Bartko, A. P. & Dickson, R. M. Photoactivated fluorescence from individual silver nanoclusters. *Science* **291**, 103-106 (2001).
8. Cleveland, C. L. et al. Structural evolution of smaller gold nanocrystals: The truncated decahedral motif. *Phys. Rev. Lett.* **79**, 1873-1876 (1997).
9. Link, S. et al. Visible to infrared luminescence from a 28-atom gold cluster. *J. Phys. Chem. B* **106**, 3410-3415 (2002).
10. Fedrigo, S., Harbich, W. & Buttet, J. Optical response of Ag₂, Ag₃, Au₂, and Au₃ in argon matrices. *J. Chem. Phys.* **99**, 5712-5717 (1993).
11. Ashcroft, N. W. & Mermin, N. D. *Solid State Physics* (HOLT, Rinehart and Winston, New York, 1976).
12. Kubo, R. *J. Phys. Soc. Jpn* **17**, 975 (1962).

13. Schaaff, T. G., Knight, G., Shafigullin, M. N., Borkman, R. F. & Whetten, R. L. Isolation and Selected Properties of a 10.4 kDa Gold:Glutathione Cluster Compound. *J. Phys. Chem. B* **102**, 10643-10646 (1998).
14. Wallace, W. T. & Whetten, R. L. Coadsorption of CO and O₂ on selected gold clusters: Evidence for efficient room-temperature CO₂ generation. *J. Am. Chem. Soc.* **124**, 7499-7505 (2002).
15. Campbell, C. T., Parker, S. C. & Starr, D. E. The effect of size-dependent nanoparticle energetics on catalyst sintering. *Science* **298**, 811-814 (2002).
16. Sanchez, A. et al. When gold is not noble: Nanoscale gold catalysts. *J. Phys. Chem. A* **103**, 9573-9578 (1999).
17. Peyser, L. A., Lee, T. H. & Dickson, R. M. Mechanism of Ag-n nanocluster photoproduction from silver oxide films. *J. Phys. Chem. B* **106**, 7725-7728 (2002).
18. Chen, W., Joly, A. G. & Roark, J. Photostimulated luminescence and dynamics of AgI and Ag nanoclusters in zeolites. *Phys. Rev. B* **65**, art. no.-245404 (2002).
19. Felix, C. et al. Ag-8 fluorescence in argon. *Phys. Rev. Lett.* **86**, 2992-2995 (2001).
20. Rabin, I. et al. Absorption and fluorescence spectra of Ar-matrix-isolated Ag-3 clusters. *Chem. Phys. Lett.* **320**, 59-64 (2000).
21. Harbich, W., Fedrigo, S., Buttet, J. & Lindsay, D. M. Optical Spectroscopy on Size Selected Gold Clusters Deposited in Rare-Gas Matrices. *Z. Phys. D-Atoms Mol. Clusters* **19**, 157-159 (1991).
22. Harbich, W. et al. Deposition of mass selected silver clusters in rare gas matrices. *J. Chem. Phys.* **93**, 8535-8543 (1990).
23. Altmann, S. L. *Band Theory of Metals* (Oxford, 1970).
24. Johnston, R. L. *Atomic and Molecular Clusters* (London and New York, 2002).

25. Kubo, R. Electronic Properties of Metallic Fine Particles .1. *J. Phys. Soc. Jpn.* **17**, 975-& (1962).
26. Wertheim, G. K., Diczko, S. B. & Buchanan, D. N. E. Noble-Metal and Transition-Metal Clusters - the D-Bands of Silver and Palladium. *Phys. Rev. B* **33**, 5384-5390 (1986).
27. Knight, W. D. et al. Electronic Shell Structure and Abundances of Sodium Clusters. *Phys. Rev. Lett.* **52**, 2141-2143 (1984).
28. Deheer, W. A. et al. Collective Dipole Oscillations in Small Sodium Clusters. *Phys. Rev. Lett.* **59**, 1805-1808 (1987).
29. Deheer, W. A. The Physics of Simple Metal-Clusters - Experimental Aspects and Simple-Models. *Reviews of Modern Physics* **65**, 611-676 (1993).
30. Uchtmann, H., Rademann, K. & Hensel, F. Metal-Nonmetal Transition and Homogeneous Nucleation of Mercury-Vapor. *Ann. Phys.* **48**, 207-214 (1991).
31. Knight, W. D., Clemenger, K., Deheer, W. A. & Saunders, W. A. Polarizability of Alkali Clusters. *Phys. Rev. B* **31**, 2539-2540 (1985).
32. Skala, L. Interpolation Formulas for Describing Size Dependence of Properties of Finite Systems and Their Use for Clusters and Biologically Important Molecules. *Theochem-Journal of Molecular Structure* **73**, 103-109 (1991).
33. Schmidt, M. & Haberland, H. Optical spectra and their moments for sodium clusters, Na-n(+), with $3 \leq n \leq 64$. *European Physical Journal D* **6**, 109-118 (1999).
34. Kreibig, U. Electronic Properties of Small Silver Particles - Optical-Constants and Their Temperature-Dependence. *Journal of Physics F-Metal Physics* **4**, 999-1014 (1974).
35. Fedrigo, S., Harbich, W. & Buttet, J. Optical-Response of Ag₂, Ag₃, Au₂, and Au₃ in Argon Matrices. *J. Chem. Phys.* **99**, 5712-5717 (1993).
36. Harbich, W., Fedrigo, S. & Buttet, J. The optical absorption spectra of small silver clusters (n = 5- 11) embedded in argon matrices. *Chem. Phys. Lett.* **195**, 613-617 (1992).

37. Harbich, W., Fedrigo, S. & Buttet, J. The Optical-Absorption Spectra of Small Silver Clusters (N=8- 39) Embedded in Rare-Gas Matrices. *Z. Phys. D-Atoms Mol. Clusters* **26**, 138-140 (1993).
38. Felix, C. et al. Fluorescence and excitation spectra of Ag-4 in an argon matrix. *Chem. Phys. Lett.* **313**, 105-109 (1999).
39. Lee, T.-H. & Dickson, R. M. Two-terminal single nanocluster quantum optoelectronic logic gates. *Proc. Natl. Acad. Sci. USA*, In Press (2003).
40. Lee, T. H. & Dickson, R. M. Single-molecule LEDs from nanoscale electroluminescent junctions. *J. Phys. Chem. B* **107**, 7387-7390 (2003).
41. Felix, C. et al. Ag8 fluorescence in Argon. *Phys. Rev. Lett.* **86**, 2992-2995 (2001).
42. Cameron, D., Haupt, S., Kaller, J. & Kappes, M. M. Laser Techniques for State-Selected and State-to-State Chemistry II. *SPIE Proceedings* **2124**, 418-425 (1994).
43. Hild, U. et al. Time-resolved photofragmentation of stored silver clusters Ag-n(+) (n=8-21). *Physical Review A* **57**, 2786-2793 (1998).
44. Kruckeberg, S. et al. The dissociation channels of silver clusters Ag-n(+), 3<=n<=20. *International Journal of Mass Spectrometry and Ion Processes* **155**, 141-148 (1996).
45. Kruckeberg, S. et al. Multiple-collision induced dissociation of trapped silver clusters Ag-n(+) (2 <= n <= 25). *J. Chem. Phys.* **110**, 7216-7227 (1999).
46. Schooss, D. et al. Photodissociation spectroscopy of Ag-4(+)(N-2)(m), m=0-4. *J. Chem. Phys.* **113**, 5361-5371 (2000).
47. Marcus, R. a. S. N. *Physics and chemistry of small clusters / edited by P. Jena, B.K. Rao, and S.N. Khanna.* (New York : Plenum Press, 1987).
48. Harbich, W., Fedrigo, S., Buttet, J. & Lindsay, D. M. Deposition of Mass Selected Gold Clusters in Solid Krypton. *J. Chem. Phys.* **96**, 8104-8108 (1992).

49. Collings, B. A., Athanassenas, K., Rayner, D. M. & Hackett, P. A. Optical Spectroscopy of Ag₇, Ag₉⁺, and Ag₉ - a Test of the Photodepletion Method. *Chem. Phys. Lett.* **227**, 490-495 (1994).
50. Collings, B. A., Athanassenas, K., Lacombe, D., Rayner, D. M. & Hackett, P. A. Optical-Absorption Spectra of Au-7, Au-9, Au-11 and Au-13 and Their Cations - Gold Clusters with 6, 7, 8, 9, 10, 11, 12, and 13 S-Electrons. *J. Chem. Phys.* **101**, 3506-3513 (1994).
51. Collings, B. A., Athanassenas, K., Rayner, D. M. & Hackett, P. A. Absorption-Spectra of Small Niobium and Gold Clusters Measured by Photodepletion of Their Rare-Gas Van-Der-Waals Complexes - Some Preliminary Experiments. *Z. Phys. D-Atoms Mol. Clusters* **26**, 36-40 (1993).
52. Boyen, H. G. et al. Oxidation-resistant gold-55 clusters. *Science* **297**, 1533-1536 (2002).
53. Kreibig, U., Fauth, K., Granqvist, C. G. & Schmid, G. 6s-Electrons in Stabilized Au₅₅-Clusters. *Zeitschrift Fur Physikalische Chemie Neue Folge* **169**, 11-28 (1990).
54. Feld, H., Leute, A., Rading, D., Benninghoven, A. & Schmid, G. Formation of Very Large Gold Superclusters (Clusters of Clusters) as Secondary Ions up to (Au₁₃)₅₅ by Secondary Ion Mass-Spectrometry. *J. Am. Chem. Soc.* **112**, 8166-8167 (1990).
55. Wallenberg, L. R., Bovin, J. O. & Schmid, G. On the Crystal-Structure of Small Gold Crystals and Large Gold Clusters. *Surf. Sci.* **156**, 256-264 (1985).
56. Schmid, G. et al. Naked Au-55 clusters: Dramatic effect of a thiol-terminated dendrimer. *Chem.-Eur. J.* **6**, 1693-1697 (2000).
57. Schmid, G. et al. Current and future applications of nanoclusters. *Chem. Soc. Rev.* **28**, 179-185 (1999).
58. Schmid, G. Large Clusters and Colloids - Metals in the Embryonic State. *Chem. Rev.* **92**, 1709-1727 (1992).
59. Liu, S. T., Maoz, R., Schmid, G. & Sagiv, J. Template guided self-assembly of Au₅(5) clusters on nanolithographically defined monolayer patterns. *Nano Lett.* **2**, 1055-1060 (2002).

60. Schmid, G. & Liu, Y. P. Quasi one-dimensional arrangements of Au-55(PPh₃)(12)Cl-6 clusters and their electrical properties at room temperature. *Nano Lett.* **1**, 405-407 (2001).
61. Wilcoxon, J. P., Martin, J. E., Parsapour, F., Wiedenman, B. & Kelley, D. F. Photoluminescence from nanosize gold clusters. *J. Chem. Phys.* **108**, 9137-9143 (1998).
62. Nilius, N., Ernst, N. & Freund, H. J. Photon emission from individual supported gold clusters: thin film versus bulk oxide. *Surf. Sci.* **478**, L327-L332 (2001).
63. Kimble, H. J., Dagenais, M. & Mandel, L. Photon antibunching in resonance fluorescence. *Phys. Rev. Lett.* **39**, 691 (1977).
64. Michler, P. et al. Quantum correlation among photons from a single quantum dot at room temperature. *Nature (London)* **406**, 968-970 (2000).
65. Michler, P. et al. Nonclassical radiation from a single quantum dot. *Physica Status Solidi B: Basic Research* **229**, 399-405 (2002).
66. Lukishova, S. G., Schmid, A. W., McNamara, A. J., Boyd, R. W. & Stroud, C. R., Jr. Room temperature single-photon source: Single-dye molecule fluorescence in liquid crystal host. *IEEE Journal of Selected Topics in Quantum Electronics* **9**, 1512-1518 (2003).
67. Lyublinskaya, I. E. & Vyas, R. Single-atom fluorescence with nonclassical light. *Physical Review A: Atomic, Molecular, and Optical Physics* **48**, 3966-79 (1993).
68. Treussart, F., Clouqueur, A., Grossman, C. & Roch, J.-F. Photon antibunching in the fluorescence of a single dye molecule embedded in a thin polymer film. *Optics Letters* **26**, 1504 (2001).
69. Lounis, B., Bechtel, H. A., Gerion, D., Alivisatos, P. & Moerner, W. E. Photon antibunching in single CdSe/ZnS quantum dot fluorescence. *Chem. Phys. Lett.* **329**, 399-404 (2000).
70. Mirin, R. P. Photon antibunching at high temperature from a single InGaAs/GaAs quantum dot. *Appl. Phys. Lett.* **84**, 1260-1262 (2004).

71. Zwiller, V., Aichele, T., Seifert, W., Persson, J. & Benson, O. Generating visible single photons on demand with single InP quantum dots. *Appl. Phys. Lett.* **82**, 1509-1511 (2003).
72. Zwiller, V. et al. Single quantum dots emit single photons at a time: Antibunching experiments. *Appl. Phys. Lett.* **78**, 2476-2478 (2001).
73. Becher, C. et al. Nonclassical radiation from a single self-assembled InAs quantum dot. *Physical Review B: Condensed Matter and Materials Physics* **63**, 121312/1-121312/4 (2001).
74. Kurtsiefer, C., Mayer, S., Zarda, P. & Weinfurter, H. Stable solid-state source of single photons. *Phys. Rev. Lett.* **85**, 290-293 (2000).
75. Michler, P. et al. A quantum dot single-photon turnstile device. *Science (Washington, D. C.)* **290**, 2282-2284 (2000).
76. Brouri, R., Beveratos, A., Poizat, J.-P. & Grangier, P. Photon antibunching in the fluorescence of individual color centers in diamond. *Optics Letters* **25**, 1294-1296 (2000).
77. Basche, T., Moerner, W. E., Orrit, M. & Talon, H. Photon antibunching in the fluorescence of a single dye molecule trapped in a solid. *Phys. Rev. Lett.* **69**, 1516-19 (1992).
78. Beveratos, A., Brouri, R., Gacoin, T., Poizat, J. P. & Grangier, P. Nonclassical radiation from diamond nanocrystals. *Physical Review A: Atomic, Molecular, and Optical Physics* **64**, 061802/1-061802/4 (2001).
79. Carmichael, H. J. Photon antibunching and squeezing for a single atom in a resonant cavity. *Phys. Rev. Lett.* **55**, 2790-3 (1985).
80. Hubner Christian, G. et al. Photon antibunching and collective effects in the fluorescence of single bichromophoric molecules. *Phys. Rev. Lett.* **91**, 093903, (2003)
81. Kumar, P. et al. Photon antibunching from oriented semiconducting polymer nanostructures. *J. Am. Chem. Soc.* **126**, 3376-3377 (2004).
82. Kumar, P. et al. Photon antibunching from oriented semiconducting polymer nanostructures. *J. Am. Chem. Soc.* **126**, 3376-3377 (2004).

83. Lounis, B. Single nanoobjects as triggered single photons sources. *Single Molecules* **2**, 289-290 (2001).
84. Paul, H. Photon antibunching. *Reviews of Modern Physics* **54**, 1061-1102 (1982).
85. Schubert, M., Siemers, I., Blatt, R., Neuhauser, W. & Toschek, P. E. Photon antibunching and non-Poissonian fluorescence of a single three-level ion. *Phys. Rev. Lett.* **68**, 3016-19 (1992).
86. Chang, R. K. & Furtak, T. E. (eds.) *Surface-Enhanced Raman Scattering* (Plenum Press, New York, 1981).
87. Champion, A. & Kambhampati, P. Surface-enhanced Raman scattering. *Chem. Soc. Rev.* **27**, 241-250 (1998).
88. Fleischmann, M., Hendra, P. J. & McQuillan, A. J. Raman spectra of pyridine at a silver electrode. *Chem. Phys. Lett.* **26**, 163-166 (1974).
89. Fleischmann, M., Hendra, P. J. & McQuillan, A. J. Raman spectra from electrode surfaces. *Journal of the Chemical Society, Chemical Communications*, 80-81 (1973).
90. Creighton, J. A. in *Surface-enhanced Raman scattering* (eds. Chang, R. K. & Furtak, T. E.) 243-273 (Plenum Press, New York, 1982).
91. Creighton, J. A., Blatchford, C. G. & Albrecht, M. G. Plasma resonance enhancement of Raman scattering by pyridine adsorbed on silver or gold sol particles of size comparable to the excitation wavelength. 790-798 (1978).
92. Moskovits, M. Surface-enhanced Raman spectroscopy. *Reviews of Modern Physics* **57**, 783-824 (1985).
93. Metiu, H. & Das, P. The electromagnetic theory of surface enhanced raman scattering. *Ann. Rev. Phys. Chem* **35**, 507-535 (1984).
94. Hildebrandt, P. & Stockburger, M. Surface enhanced Raman Spectroscopy of Rhodamine 6G adsorbed on colloidal silver. *J. Phys. Chem.* **88**, 5935-5944 (1984).

95. Haynes, C. L. & Van Duyne, R. P. Plasmon-sampled surface-enhanced Raman excitation spectroscopy. *J. Phys. Chem. B* **107**, 7426-7433 (2003).
96. Ferraro, J. R. *Introductory Raman Spectroscopy* (Academic Press, Boston, 1994).
97. Garrell, R. L. & Pemberton, J. E. (eds.) *Fundamentals and Applications of Surface Raman Spectroscopy* (VCH Publishers, Deerfield Beach, FL, 1994).
98. Osawa, M., Matsuda, K., Yoshii, K. & Uchida, I. Charge transfer resonance Raman process in surface-enhanced Raman scattering from p-aminothiophenol adsorbed on silver. *J. Phys. Chem.* **98**, 12702 (1994).
99. Otto, A. in *Light Scattering in Solids IV* (eds. Cardona, M. & Gundtherodt, G.) 289-418 (Springer-Verlag, Berlin, 1984).
100. Otto, A., Mrozek, I., Grabhorn, H. & Akemann, W. Surface -enhanced Raman scattering. *J. Phys. Condens. Mater.* **4**, 1143-1212 (1992).
101. Persson, B. N. J. On the theory of surface enhanced Raman scattering. *Chem. Phys. Lett.* **82**, 561-565 (1981).
102. Kneipp, K. et al. Single molecule detection using surface-enhanced Raman scattering (SERS). *Phys. Rev. Lett.* **78**, 1667-1670 (1997).
103. Nie, S. M. & Zare, R. N. Optical detection of single molecules. *Annu. Rev. Biophys. Biomolec. Struct.* **26**, 567-596 (1997).
104. Jiang, J., Bosnick, K. A., Maillard, M. & Brus, L. E. Single molecule raman spectroscopy at the junctions of large Ag nanocrystals. *J. Phys. Chem. B* **107**, 9964-9972 (2003).
105. Nie, S. M. & Emory, S. R. Probing single molecules and single nanoparticles by surface-enhanced Raman scattering. *Science* **275**, 1102-1106 (1997).
106. Henglein, A., Mulvaney, P. & Linnert, T. Chemistry of Agn Aggregates in Aqueous-Solution - Nonmetallic Oligomeric Clusters and Metallic Particles. *Faraday Discuss.*, 31-44 (1991).

CHAPTER 2

Experimental section

2.1 Overall Experimental Strategy

The ultimate goal of my research has been the creation of novel fluorescent metal nanoclusters and understanding their size-dependent emission. Wet chemistry was used to prepare these metal clusters. General synthetic procedures and experimental methods used throughout this thesis are presented in this chapter. Experimental procedures specific to the work are more fully described in the relative chapters.

2.2 Synthesis

2.2.1 Fluorescent gold clusters

I. Octadecanethiol encapsulated fluorescent gold clusters. $\text{HAuCl}_4 \cdot 5\text{H}_2\text{O}$ (0.5 μmol) (Aldrich) and octadecanethiol (0.25 μmol) (Aldrich) were co-dissolved in 2mL chloroform (90%) and ethanol (10%) solution. The solution was subsequently reduced with equivalent NaBH_4 aqueous solution. After being stirred for two days, the solutions produce strong blue emission with a maximum emission wavelength at 455 nm. The emission colors of the solutions were observed from blue to the IR region by changing the gold to octadecanethiol molar ratio from 0.5 to 8. Separation of different emissive species is being carried on. Although octadecanethiol can

stabilize the gold clusters very well, its hydrophobicity precludes the use of electrospray mass spectroscopy from determining cluster size. In addition, the molecular weight of a single gold cluster is not only dependent on the number of gold atoms in the cluster, but also on the number of octadecanethiol molecules surrounding the cluster. This causes inherent difficulty in cluster size assignment through correlation of fluorescence intensity with mass spectral abundance.

II. Dendrimer encapsulated fluorescent gold clusters. Widely used to prepare larger metallic and semiconductor nanoparticles,¹⁻⁴ second and fourth generation OH-terminated poly (amidoamine) PAMAM (G2-OH and G4-OH, respectively, Aldrich) were utilized to stabilize and solubilize gold nanoclusters in both aqueous and methanol solutions. By dissolving 0.5 μmol G4-OH or G2-OH and 1.5 μmol $\text{HAuCl}_4 \cdot 5\text{H}_2\text{O}$ (Aldrich) into 2 mL of deionized water (18 M Ω), gold ions were sequestered into dendrimers and then reduced by slowly adding an equivalent of NaBH_4 (0.005 M) into the solution within 30 min. Reduced gold atoms aggregate within the dendrimers to form small nanodots (dendrimer-encapsulated nanoclusters) and large nanoparticles. The solution was stirred for two days until reaction and aggregation processes were completed. Solutions were subsequently purified through centrifugation (16,000 g, Eppendorf) to remove the large gold nanoparticles.³ A clear Au clusters solution was obtained after 1 hr centrifugation.

Simple adjustment of Au to PAMAM molar ratios with subsequently reduction enables facile tuning of nanocluster excitation and fluorescence. By adjusting the molar ratio between gold ions and dendrimer, spectrally pure UV-

emitting gold clusters were created in 0.5 μmol G2-OH and 0.5 μmol HAuCl_4 in 2 mL distilled water. Green-emitting gold clusters were synthesized with 0.5 μmol G2-OH and 3 μmol HAuCl_4 in 2 mL distilled water. Red and IR emitting gold clusters were preferentially synthesized with 6.0 μmol and 7.5 μmol HAuCl_4 , respectively, co-dissolved into 2 mL with 0.5 μmol G4-OH or G4-NH₂. All nanoclusters can be created with AuBr_3 as well. Created through this general procedure, and differently sized fluorescent gold nanoclusters exhibit discrete excitation and emission spectra from the ultraviolet to the near infrared.

2.2.2 Large luminescent gold nanoparticles

Glutathione, a three amino acid peptide, was used as a scaffold to synthesize water-soluble and biocompatible large luminescent gold nanoparticles. 5 μmol glutathione (Aldrich) and 2.5 μmol HAuCl_4 (Aldrich) respectively were dissolved into 1 mL distilled water (18 M Ω), and then the solutions were mixed together. The bright yellow luminescence was observed after the solution was stirred for 3 days under room-light irradiation. Pale yellowish products were then centrifuged out of the solution. To purify this product, the precipitates were washed repeatedly with water at least three times to ensure removal of all other reactants such as HAuCl_4 and glutathione. The products were then redissolved in water and precipitated out of the solution through centrifugation again to ensure only large molecular weight products in the precipitates. This step was repeated at least three times to make sure that there are no small molecular weight gold clusters in the products. The product shows strong bright yellow luminescence. Amazingly, the luminescence color can be tuned to red

by simply adjusting the initial mole ratio between glutathione and HAuCl_4 to 1 : 2 with the same gold and glutathione concentration as described above. Red emitting species were also purified with the same procedure. If mole ratio between gold and glutathione is $\sim 1:1$, orange color emission was observed. After similar purification method, the orange solutions can be further purified with poly(acryl amide) gel electrophoresis method. Yellow emitting species usually run more slowly than red emitting species toward the positive electrode in an electrical field, which should arise from a combination of size and charge differences.

2.2.3 Fluorescent silver nanoclusters

The synthetic procedure employed to prepare dendrimer encapsulated fluorescent silver clusters was quite similar to that used to prepare encapsulated gold nanoclusters. PAMAM G4-OH dendrimers were utilized to concentrate, stabilize, and solubilize Ag nanoclusters in both aerated and deaerated aqueous solutions. By dissolving $0.5 \mu\text{mol}$ G4-OH and $1.5 \mu\text{mol}$ AgNO_3 into 1 mL distilled water ($18 \text{ M}\Omega$) and adjusting to neutrality with $160 \mu\text{mol}$ acetic acid, silver ions readily interact with the dendrimer. Because of our desire to create dendrimer-encapsulated nanoclusters (“nanodots”) not large nanoparticles, no reducing agents were added to our reactions. The fluorescence of these solutions was probed by placing a $10\text{-}\mu\text{l}$ drop of the solution on a clean coverslip in ambient air, nitrogen, and/or evacuated (10^{-5} torr) environments and irradiated with blue light (450-480 nm) from a bandpass-filtered mercury lamp through a standard epifluorescence microscope. Fluorescent silver clusters were formed in the solution during the photoactivation. Results were

unaffected by degree of oxygenation. In addition, since short amine-rich peptides (peptide sequence: Ala-His-His-Ala-His-His-Ala-Ala-Asp⁵) are known to strongly interact with metal ions, peptide encapsulated fluorescent silver clusters were also prepared with the same procedure. As a control experiment, pure silver nitrate solution was also photoactivated with the same procedure, however, no any emission was observed.

2.2.4 Nonfluorescent silver nanoparticles

To compare differences between fluorescent silver clusters and nonfluorescent large silver nanoparticles, dendrimer encapsulated large silver nanoparticles were also prepared.⁴ G4-OH (1 μmol) and silver nitrate (20 μmol) were dissolved in 10 mL organic free, deionized water. The pH was adjusted to 5.0 with dilute nitric acid. The resulting solution was stirred for 15 min, followed by the slow addition of up to 100 μmol sodium borohydride dissolved in 2 mL deionized water. Reduction of G4-OH/Ag⁺ at pH 5 with 1.25 equivalents of borohydride resulted in the formation of a clear, yellow-brown solution of G4-OH/Ag(0) nanoparticles. Silver nanoparticles with size ranging from 2 nm to 100 nm were observed.

2.3 Electrospray ionization mass spectrometry

Since the majority of metal nanoclusters studied in this thesis are too small to be observed with electron microscopy, we mainly employed mass, absorption and fluorescence spectrometry to characterize the nanoclusters properties. Metal cluster sizes were determined based on their molecular masses. Mass spectrometers can be divided into three fundamental parts, namely the ionization source, the analyzer and

the detector. Electrospray ionization (ESI) is the most gentle ionization method and was employed to analyze the high molecular weight metal nanoclusters. ESI is well-suited to the analysis of polar molecules ranging from 100 Da to more than 1,000,000 Da in molecular mass within 0.01% error. A Quattro LC ESI mass spectrometer (Micromass, Georgia Tech Mass spec facilities) was used to measure the cluster masses from aqueous solutions. A general procedure for characterizing metal cluster mass is as follow: a very small amount (10 μL) of the aqueous cluster solution is diiluted into 200 μL of DI water and then the solution was mixed with 0.2 μL formic acid for better ionization. A small volume (5 μL) of the sample is then pumped through a narrow, stainless steel capillary at a flow rate of 5 $\mu\text{L}/\text{min}$. A 3.5 kV voltage is applied to the tip of the capillary, which is inserted within the ionization source of the mass spectrometer. The charged droplets diminish in size by solvent evaporation, assisted by a warm flow of nitrogen. Eventually, the charged sample ions pass through a small aperture in a sampling cone into the mass analyzer of the mass spectrometer. For dendrimer encapsulated silver or gold clusters, the corn voltage is around 10V. In ESI, samples with molecular weights up to ca. 1200 Da give rise to singly charged ions such as protonated molecular ion of the formula $(\text{M}+\text{H})^+$ in positive ionization mode. However, some samples such as glutathione encapsulated gold nanoparticles were also studied in negative ionization mode. The samples with molecular weights greater than 1200 Da give rise to multiply charged ions such as $(\text{M}+\text{nH})^{n+}$ in positive ionization mode and $(\text{M}-\text{nH})^{n-}$ in negative ionization mode. Software (MassLynx 3.4) then converts the multiply charged ion data into a spectrum

corresponding to the true molecular weight. Since the molecular mass of dendrimer polyamidoamine PAMAM G2OH is 3271 (Figure 2.3.1), all the mass spectra obtained have been deconvoluted into the one-charge state spectrum. ESI mass spectra data is highly reproducible under identical conditions. As a control experiment, pure G2OH mass intensity observed from mass spectra was found to linearly depend on the dendrimer concentration in the solutions (Figure 2.3.2). However, only very messy mass spectra were obtained from dendrimer G4-OH solution

2.4 Transmission electron spectroscopy⁶

A modern TEM basically consists of an electron illumination system, a specimen stage, an electro-magnetic objective lens system, a data recording system and a chemical analysis system. The samples were prepared on Formvar/Carbon coated Copper or Nickel grid (200 Mesh) (Ted Pella, INC). A drop of a sample solution was placed and dried on a copper grid. Attempts to observe small dendrimer or octadecanethiol encapsulated silver/gold nanoclusters were made, but no particles were observed under TEM. In this thesis, only large glutathione encapsulated luminescent gold nanoparticles (~ 2nm) were characterized using a Hitachi HF-2000 TEM at 200 kV in detail. Lattice images of luminescent gold nanoparticles were obtained using a HR TEM JEOL 4000EX operated at 400KV.

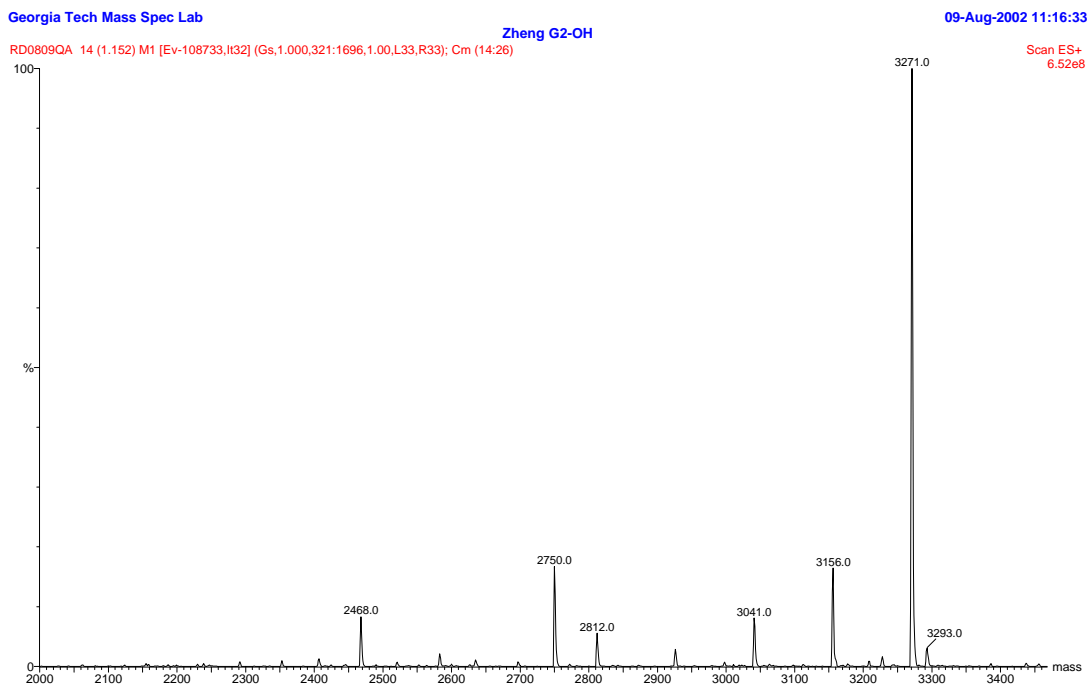


Figure 2-3-1. ESI mass spectrum of dendrimer PAMAM G2-OH. A small amount ($5\ \mu\text{L}$) of dendrimer G2OH aqueous solution ($1.5\ \text{mM}$) is pumped through a narrow, stainless steel capillary at a flow rate of $5\ \mu\text{L}/\text{min}$. A $3.5\ \text{kV}$ voltage is applied to the tip of the capillary and the cone voltage is around 10V . The molecular weight of Dendrimer PAMAM G2-OH is 3271 , which is consistent with the experimental result.

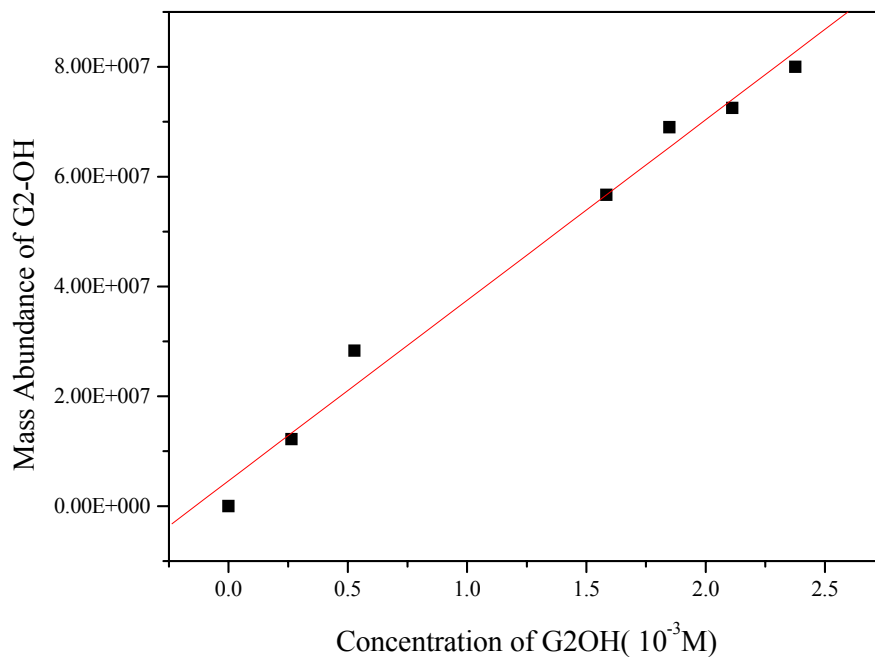


Figure 2-3-2. Correlation of G2-OH mass abundance with its concentration in aqueous solutions. The detailed procedure for the mass abundance measurement with ESI mass spectrometer has been described in Figure 2-3-1. The linear correlation indicates mass abundance of dendrimer G2-OH is proportional to its concentration in the solution under the same experimental conditions.

2.5 Photon correlation spectroscopy

Photon correlation spectroscopy (PCS) called dynamic light scattering or quasi-elastic light scattering spectroscopy can provide accurate hydrodynamic radii of the particles by analyzing intensity fluctuations of light scattered from the particles due to their Brownian motion in solutions. One advantage of PCS over other size characterization methods such as TEM and SEM is this technique can study particle in solution. Consequently, in combination with TEM results, more complete information on the particle sizes can be provided. In this thesis, hydrodynamic radii of some large luminescent gold nanoparticles were measured with photon correlation spectroscopy (Protein Solution Inc.). A small amount (~0.5 mL) of a luminescent gold nanoparticle solution was placed into a three-window cell and illuminated with a near IR laser diode. The scattering angle was fixed at 90 degree. The intensity of scattering light from the particles was recorded, and an average hydrodynamic radii of the different luminescent particles in aqueous solution is readily obtained with this technique.

2.6 X-ray photoelectron spectroscopy⁷

Photoelectron spectroscopy utilizes photo-ionization and energy-dispersive analysis of the emitted photoelectrons to study the composition and electronic state of the surface region of a sample. As for metal nanoparticles, X-ray photoelectron spectroscopy is also an excellent technique to investigate the overall charge states of nanoparticles. Atoms in a higher positive oxidation state exhibit a higher binding energy due to the extra columbic interactions between the photo-emitted electron and

the ion core. This ability to discriminate different oxidation states and chemical environments is one of the major strengths of XPS. Since the number of the free electrons in the metal nanoparticles is strongly dependent on the charge states of its constituent metal atoms, XPS technique was employed to measure the binding energies of core electrons and interpreted as being indicative of the overall charge states of gold atoms in these luminescent glutathione encapsulated gold nanoparticles. In this thesis, the average oxidation states of gold atoms in luminescent gold nanoparticle powders on Si wafers were measured using a PHI 1600/3057 X-ray Photoelectron Spectrometer (XPS) with a standard aluminum x-ray source. Au $4f_{7/2}$ and $4f_{5/2}$ binding energies in the luminescent gold nanoparticles and nonluminescent gold nanoparticles were investigated.

2.7 Fluorescence Lifetime measurement

Fluorescence lifetimes of luminescent metal nanomaterials in bulk were studied with a Timemaster Fluorescence lifetime spectrometer (Photon Technologies International), coupled to a TCSPC-1000 time correlated single photon counting electronics. TiO_2 aqueous suspensions were used as light scattering source to obtain instrument response IRF. Effective excitation wavelengths are in the range from 300 nm to 680 nm. Fluorescence lifetimes ranging from ns to μs of fluorescent gold clusters and luminescent gold nanoparticles were accurately measured at room temperatures.

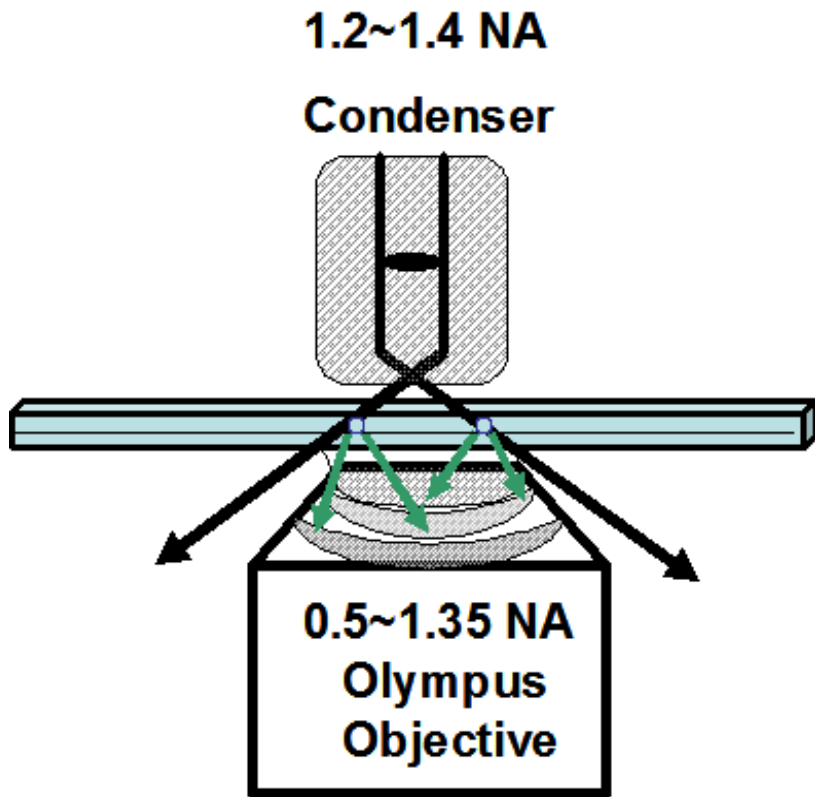


Figure 2-8-1. Schematic of the dark field setup on an inverted microscope. The particles on the interface of two coverslips are illuminated with high-angle annular illumination light, which is created by placing the opaque stop inside the condenser. Scattered light builds up the particle images on a dark background.

2.8 Dark Field microscope

Dark field light microscopy is also a very powerful technique to image nanoparticles with high contrast. Typically a drop of a nanoparticle solution was placed on a coverslip, and then was covered by the second coverslip, forming a sandwich structure. (Figure 2.8.1). The sample was then illuminated with a hollow cone of white light coming out from a high-numerical aperture condenser (1.4-1.2NA Olympus) with an opaque stop in the center of the light path. The high angle light was then focused at the plane of the sample. Imaging is performed with lower NA than used for illumination such that only light scattered by nanoparticles is observed. The scattered light from individual nanoparticles is then collected by the objective lens (0.5~1.35 NA 100× Olympus objective with an iris). The image was built up by those rays scattered by the sample and appears as bright spots against a dark background. In this thesis, we used darkfield microscope to image the nonluminescent silver and luminescent gold nanoparticles. Metal nanoparticle with sizes larger than 1.8 nm can be readily observed with dark field microscopy.

2.9 Total Internal Reflection Fluorescence Microscope

Total internal reflection (TIR) is the phenomenon that all light is reflected off the boundary above a critical angle (Figure 2.9.1). TIR only takes place when the light propagates from higher refractive index (n_1) to lower refractive index (n_2) and the incidence angle must be greater than the critical angle. Given by Snell's law, the

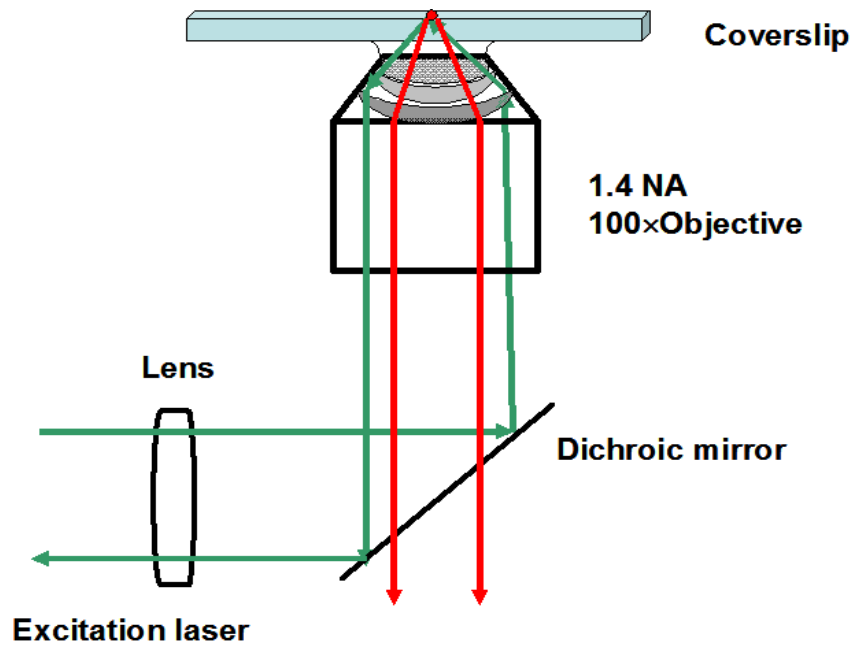


Figure 2-9-1. Total internal reflection geometry through a microscope objective. The excitation laser is brought into the microscope through its side port and illuminates the sample at a high incident angle. Only a range of 100-200 nm above the coverslip can be illuminated due to the penetration of the evanescent wave.

critical angle is equal to $\text{Sin}^{-1}(n_2/n_1)$. Although all the incident light is reflected from the interface once the angle of incidence is greater than the critical angle, an evanescent wave still can penetrate about 100-200 nm into the lower refractive index medium. The total internal reflection microscope takes advantage of the evanescent wave to specifically illuminate only a range of 100-200 nm above the substrate, and fluorophores beyond this range can not be excited. As a result, this technique becomes a powerful tool to study single molecule emission with high signal to noise ratio. Single molecule behaviors such as blinking, photoactivation, emission patterns of fluorescent silver and gold clusters were observed and characterized in a wide field imaging configuration.

2.10 Single molecule excitation spectroscopy

Single molecule excitation spectroscopy is also a powerful technique to investigate optical transitions of fluorescent metal clusters. Single molecule excitation spectra of silver clusters were collected with a Zeiss Axiovert 200 microscope in an epi-fluorescent geometry. The setup is shown in Figure 2.10.1. A compact Ar lamp (Photon Technologies International) coupled to a monochromator (DeltaRam V) was used as an excitation light source. Silver clusters were excited at different excitation frequencies and emission was collected using a highly sensitive CCD camera (Coolsnap, HQ). The excitation spectra were obtained after correlating excitation frequency with emission intensity. To collect the excitation spectra of silver clusters, a shortpass excitation filter (SP525nm) was placed in the excitation path and a long pass emission filter (LP 530 nm) was placed in the emission path. Both single

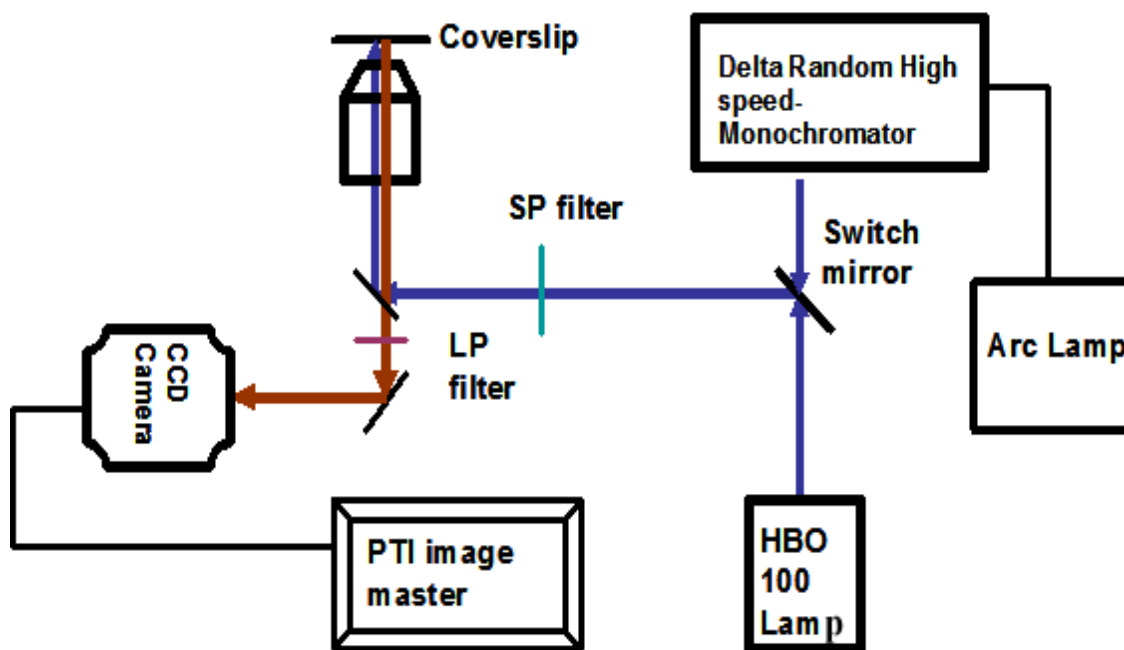


Figure 2-10-1. Schematic of the setup for measuring single molecule excitation spectra of fluorescent silver clusters. Excitation spectra of silver clusters were collected with a Zeiss Axiovert 200 microscope in epi-fluorescent geometry. Emission intensities of silver clusters at different excitation frequencies were collected with a CCD camera and then converted into the excitation spectra with PTI image master software.

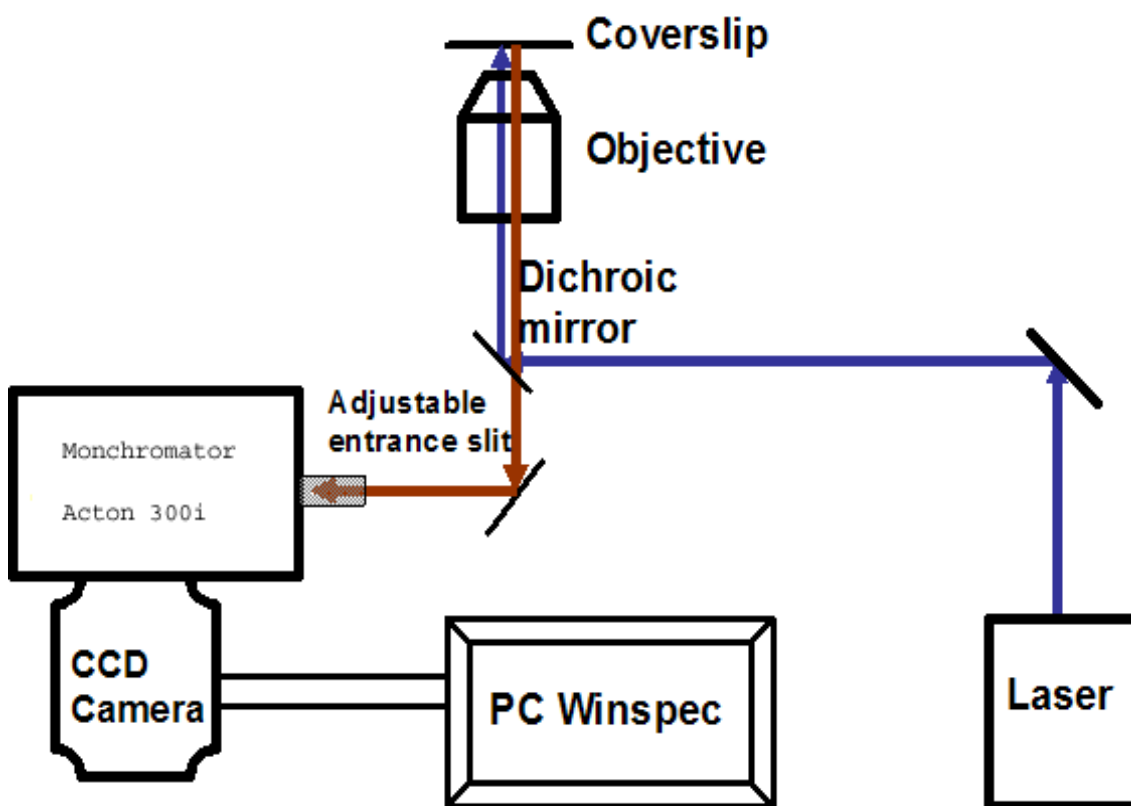


Figure 2-11-1. Schematic of the setup for measuring single molecule fluorescence /Raman spectra of the silver clusters. Emission spectra of silver clusters were collected with an Olympus IX 70 inverted microscope in an epi-fluorescent geometry.

molecule and bulk excitation spectra of fluorescent silver clusters on the coverslip surfaces were obtained with this technique.

2.11 Single molecule fluorescence/Raman spectroscopy

Single molecule fluorescence/Raman spectra were collected with an Olympus IX-70 inverted microscope, which is coupled to an Acton Spectra-Pro 300i imaging monochromator equipped with a Roper Scientific TE-cooled spectroscopy CCD camera. (Figure 2.11.1) The CCD camera was used to collect either the zeroth order light simply reflected from a mirror or the light dispersed with a grating. Generally, fluorescence spectra were collected with 150l/mm grating and Raman spectra were collected with a 600l/mm grating. The resolution increases with the number of lines on a grating. Generally, a CW Ar-Ion laser (458, 477, 488, 514 nm) or pulsed Ti:Sapphire (720-900 nm, 200fs, 82 MHz) laser is directed into the microscope through the back port and reflected to the substrate by a dichroic mirror. The laser beam was tightly focused on the samples by a 1.4NA 100x objective. Images and emission spectra of fluorescent silver clusters at the single molecule level were obtained with this technique.

2.12 Single molecule photon antibunching⁸

To demonstrate the non-classical properties of the fluorescence from single metal clusters, the second order intensity correlation function $g^{(2)}(\tau)$ was measured with two APDs behind a beam splitter. Similar to lifetime measurement, the setup is shown in Figure 2.12.1. Emission from a single molecule is split into two beams by 50/50 beam splitter, and each is directed onto an APD, which generates TTL pulse for

the SYNC and CFD channels of a PC based integrated time-to amplitude-converter (TAC) and a pulse-height analysis systems. (Time-Harp 100, Picoquant GmbH). By using a delay module (Ortec 425A), proper zero delay between Start and Stop detection events is achieved within the observation window. Depending on the lifetimes of the single molecules, both CW and pulsed lasers can be used as excitation light sources. Lifetime information can be achieved from CW excitation as long as lifetimes of single molecules are longer than the APD time resolution. We used CW He-Ne laser as the excitation light source to achieve antibunching from single gold clusters. Since silver clusters have ultrafast lifetime, pulsed laser excitation must be used.

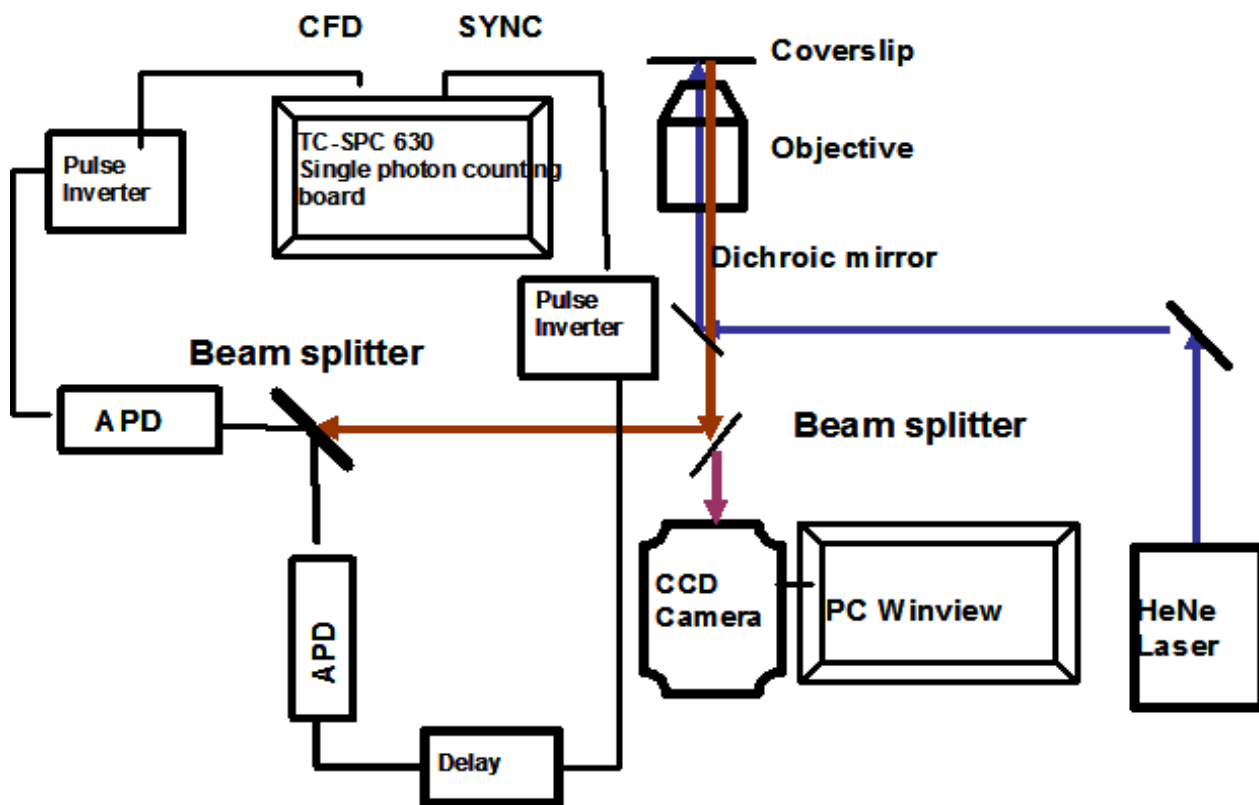


Figure 2-12-1. Hanbury-Brown and Twiss experimental setup for antibunching of gold clusters (Au₂₃) fluorescence. Gold cluster is excited with HeNe (632.8 nm) laser at room temperature.

2.13 References

1. Sooklal, K., Hanus, L. H., Ploehn, H. J. & Murphy, C. J. A blue-emitting CdS/dendrimer nanocomposite. *Adv. Mater.* **10**, 1083-+ (1998).
2. Balogh, L. & Tomalia, D. A. Poly(amidoamine) dendrimer-templated nanocomposites. 1. Synthesis of zerovalent copper nanoclusters. *J. Am. Chem. Soc.* **120**, 7355-7356 (1998).
3. Crooks, R. M., Zhao, M. Q., Sun, L., Chechik, V. & Yeung, L. K. Dendrimer-encapsulated metal nanoparticles: Synthesis, characterization, and applications to catalysis. *Accounts Chem. Res.* **34**, 181-190 (2001).
4. Zheng, J., Stevenson, M. S., Hikida, R. S. & Van Patten, P. G. Influence of pH on dendrimer-protected nanoparticles. *J. Phys. Chem. B* **106**, 1252-1255 (2002).
5. Slocik, J. M., Moore, J. T. & Wright, D. W. Monoclonal antibody recognition of histidine-rich peptide encapsulated nanoclusters. *Nanolett* **2**, 169-173 (2002).
6. Z.L. Wang, Z. C. K. *Functional and smart materials : structural evolution and structure analysis* (Plenum Press, New York, 1998).
7. Nefedov, V. I. V. I. *X-ray photoelectron spectroscopy of solid surfaces (VSP, Utrecht, Netherlands, 1988).*
8. Lee, T. H. Silver nanocluster single molecule optoelectronics and its applicatons. Thesis (2004).

CHAPTER 3

Highly Fluorescent, Water-Soluble, Size-Tunable Gold Nanoclusters

3.1 Introduction

Gold exhibits a particularly wide range of material behavior along the atom to bulk transition.¹⁻¹¹ Optical and electronic properties of gold are not only strongly size-dependent, but also dramatically change on different characteristic length scales.¹² Small gold clusters of sizes comparable to the Fermi wavelength play a unique role in the studies of material property transitions from atoms over nanoparticles to the bulk and have been attracting intensive interest for many decades.^{4-6,11,13-17} Such gold nanoclusters, composed of only several tens of atoms, exhibit molecule-like transitions as the density of states is insufficient to merge the valence and conduction bands.^{5,7-9} Analogous to the alkali metals, the high electron density, strong electron-electron coupling and efficient screening^{18,19} should make the electronic structure of gold clusters change dramatically with size and geometry, but, the influence of the d-electrons is thought to significantly complicate the free electron behavior.^{12,20}

Optical spectroscopy is a powerful technique to investigate the electronic structures of small metal clusters. Gold exhibits size-tunable plasmon absorption

widths by confining conduction electrons in both ground and excited states to dimensions smaller than the electron mean free path (~50 nm).¹⁹ Further confinement of the free electrons, however, reaches the Fermi wavelength of an electron (~0.5 nm) which should result in discrete, quantized electronic transitions.²⁰ While such sub-nm nanoclusters are too small to have the continuous density of states necessary to support a “plasmon” characteristic of larger free electron metal nanoparticles,^{12,21} the jellium model predicts that nanoparticle plasmon widths and nanocluster transition energies of true free electron metals should both scale with inverse cluster radius.²² As gas phase photodissociation experiments are unable to probe the lowest energy transitions,¹² the size-dependent behavior of gold metal and the development of the plasmon remain poorly understood.^{4,8,12,18,23,24}

Limited by broad size distributions and low concentrations of synthetically produced small clusters, direct optical absorption measurements of small gold clusters are more difficult than those on their larger nanoparticle counterparts. As early as the 1980s, fluorescence instead of plasmon scattering was also observed from few-atom gold dimer with emissions at 450, 545 and 580 nm.²⁵ Subsequently, Harbich et al. employed a “soft landing” technique to prepare Au dimer in Kr and Ar matrices at low temperature and observed emissions at 285, 325, 742 and 757 nm.^{26,27} Similarly prepared Au₃ in solid Ar matrices produced 529, 579 and 809 nm emission.^{26,27} Although the optical transitions of gold clusters varied from report to report, these works demonstrated that fluorescence can be used to characterize their size-dependent electronic transitions.

Observation of small gold cluster fluorescence at low temperature encouraged many authors to synthesize gold clusters in ambient solution. In 1998, Wilcoxon et al. observed blue emission at 440 nm from gold nanoparticles smaller than 5 nm (diameter) and also found the fluorescence intensity increased 4 fold with decreasing size to 2.5nm.¹¹ The emission was attributed to the radiative recombination of sp band and d band electrons and holes in based on the assumption that these luminescent gold “nanoparticles” have the same electronic structure as the bulk gold metal. However, this assumption is under debate because these luminescent gold “nanoparticles” have no plasmon while bulk gold metal does. Consequently, there must be dramatic differences in electronic structure between bulk gold metal and these luminescent gold “nanoparticles”. Although the exact size of the emissive species was not able to be identified due to heterogeneity of the solution, no plasmon observed from these emissive species suggests that emission might originate from even smaller gold clusters than the authors expected.

In 2000, Whetten and coworkers synthesized dodecanethiol encapsulated 1.1 and 1.7 nm gold clusters, of about 38 and 145 atoms, respectively, which produced emission in the range from 1.15 eV to 0.75 eV under the excitation of 1064 nm Nd:YLF laser.²⁸ The fluorescence quantum yield of 1.7 nm gold clusters was about $(4.4 \pm 1.5) \times 10^{-5}$. Emission was attributed to sp to sp-like (intraband) transitions²⁸ instead of sp to d (interband) transitions suggested by Wilcoxon et al.,¹¹ because the onset for such interband transitions in bulk gold occurring at ~1.7 eV is much larger than the observed emission energies.¹³ These authors also suggested that jellium

electronic shell model could be used to explain this intraband transition, but the exact mechanism for the emission was unclear.²⁸

In 2001, Whetten and El-Sayed observed near-IR emissions at 1.55 and 1.15 eV from aqueous glutathione encapsulated Au₂₈ cluster solutions at room temperature.⁴ The fluorescence quantum yield of Au₂₈ clusters increased to $(3.5 \pm 1.0) \times 10^{-3}$. However, the photoluminescence mechanism seems even more complicated than expected. Both ns and μ s lifetime components were observed from these emissions. Two possible models were proposed to explain the emission from Au₂₈ clusters. The first model is the solid-state model.⁴ The high energy emission at 1.55 eV is attributed to radiative interband recombination between the sp and d-bands while the low energy emission at 1.15 eV is assigned to radiative intraband transitions within the sp-band across the HOMO-LUMO gap. In this case, low energy intraband recombination still involved a prior nonradiative recombination of the hole in the d-band created after excitation with an (unexcited) electron in the sp-band,⁴ which is different from the mechanism proposed by Whetten et al in their early work for 1.1 and 1.7 nm gold clusters.²⁸ The second model is called the molecular model. Both 1.55 and 1.15 eV emissions are due to the intraband transitions. The high energy emission at 1.55 eV is attributed to radiative recombination of the ground state (S₀) and the higher excited state (S₁) in the sp band of Au₂₈ clusters, while the low energy emission at 1.15 eV is due to radiative relaxation of the ground state and the lowest excited triplet state in the sp band. Although both mechanisms could partially explain

the observations from the small gold clusters, further studies are required to completely understand this amazing size-dependent emission.

Since optical and electronic properties of metal clusters are determined by their electronic structure, it is very important to understand how the electronic structure changes with size in this smallest size regime. Ho and coworkers recently studied the energy levels of few atom gold nanowires on a NiAl substrate at cryogenic temperatures with scanning tunneling microscopy.²⁹ Results indicated that the electronic properties such as conductance of one-dimensional gold cluster chains were determined by the number of free electrons in the chains. Each gold atom in a chain only donate its lone 6s electron, and these valence electrons are delocalized in the whole chain because of a strong electron screening effect due to core electrons and d electrons. On the Fermi wavelength scale, 5d electrons of gold clusters are more tightly bound by the nucleus than 6s electrons are.¹⁹ As a result, there is also a large energy gap between the s band and d bands, consequently, conductance of few-atom gold clusters is solely determined by the conduction band structure built up by 6s valence electrons.²⁹

To investigate the origin of emission from small gold clusters, fluorescence can be utilized as a signature to explore the evolution of gold cluster electronic structure with size. In addition, although the Au₂₈ nanoclusters with million-fold enhanced fluorescence quantum yields ϕ_F , relative to that of bulk gold films have been created,³⁰ the 10^{-3} to 10^{-4} quantum yields and often polydisperse nanoparticle size distributions have precluded them from being good fluorophores.^{4,10} Thus, the

creation of new types of fluorescent gold clusters with high quantum yields and tunable emission will not only shed light on the fundamental question of how the electronic structures of gold clusters change with size, but also offers the opportunity to develop a new generation of small and biocompatible fluorophores as biological labels or as optoelectronic emitters.

Here, we report the creation of quantum-confined, water-soluble, high quantum yield Au nanodots with discrete absorption and fluorescence that is size-tunable from the UV to the near IR. The discrete absorptions and emissions scale with the number of atoms, N , as $N^{-1/3}$, precisely as predicted by the spherical jellium model, but in contrast to the $N^{-2/3}$ scaling for semiconductor quantum dots that do not exhibit the free electron shell filling degeneracies characteristic of metals.¹⁹ These two cases correspond to multi- and single electron artificial atoms, respectively. Bridging the gap between discrete gas phase absorptions of analogous alkali metal nanoclusters and the characteristic plasmon absorptions of large noble metal nanoparticles in solution, these few-atom water-soluble Au species offer the “missing link” between atomic and nanoparticle optical properties with clear protoplasmonic fluorescence arising from intraband transitions of the nanocluster free electrons.

3.2 Results and Discussion

3.2.1 Excitation and emission spectra of fluorescent gold clusters

Currently both water-soluble and organic-solvent soluble gold nanoclusters have been successfully prepared within dendrimer and alkyl thiol scaffolds

respectively. The detailed synthesis procedures have been described in Chapter 2. Figure 3.2.1 shows a fluorescence image and discrete excitation and emission spectra of different dendrimer encapsulated gold clusters in aqueous solutions. By adjusting the molar ratio between gold ions from 1:1 to 1 : 15, both excitation and emission energies can be easily tuned from UV to near IR emission. Analogous to producing large nanoparticles within PAMAM hosts,³¹ both the relative Au:PAMAM concentration and the dendrimer generation enable optimization of the desired nanocluster emission color in solution. Interestingly, the PAMAM scaffold stabilizes different nanocluster sizes and yields orders of magnitude higher fluorescence quantum yields than does glutathione.⁴ This great improvement in quantum yield might arise from better protection by 3-D branched structure of the dendrimers and also the chemically softer amines of the dendrimers.

Although there are no chromophores in dendrimer PAMAM-OH, blue emission at 450 nm recently has also been observed from these OH-terminated PAMAM dendrimers after oxidation of the OH groups.³² The similarity in the emission energy to that of Au₈ recently initiated some debates in whether the blue emission we observed from dendrimer encapsulated Au₈clusters is caused by the dendrimers oxidation. To address this controversy, we also synthesized octadecanethiol encapsulated fluorescent gold clusters with a similar preparation procedure (see Chapter 2). No emission was observed from pure octadecanethiol or the oxidized or reduced octadecanethiol. After slowly reducing the octadecanethiol/Au complex in chloroform/ethanol solution with NaBH₄, strong blue

emission at 455 nm was observed from octadecanethiol encapsulated gold clusters (shown in Figure 3.2.2). In addition, similar to the observations from dendrimer encapsulated gold clusters, the emission from octadecanethiol encapsulated gold clusters can also be tuned from blue to near IR region by simply adjusting the ratio between the thiol molecules and gold ions. (Figure 3.2.2). In addition, these octadecanethiol encapsulated gold clusters also have ns lifetime. Detailed spectroscopic studies of these thiol encapsulated gold clusters are being carried on by other group members. Combination of all these observations from different scaffold-encapsulated gold clusters provides strong evidence that small gold clusters are responsible for the observed emission. Although octadecanethiol can stabilize the gold clusters very well, its hydrophobicity precludes cluster size determination with electrospray mass spectrometry. In addition, the molecular weight of a single gold cluster is not only dependent on the number of gold atoms of a cluster, but also the number of octadecanethiol molecules surrounding the cluster, which also causes inherent difficulties in cluster size assignment. All aqueous and organic solvent nanoclusters solutions are very stable, lasting for months either in solution or as dried powders. Solutions from re-dissolved Au-nanoclusters powders have identical properties to those initially created.

3.2.2 Size determination of fluorescent gold clusters

The well-defined dendrimer structure enables analysis of encapsulated nanocluster sizes with electrospray ionization (ESI) mass spectrometry. As shown in

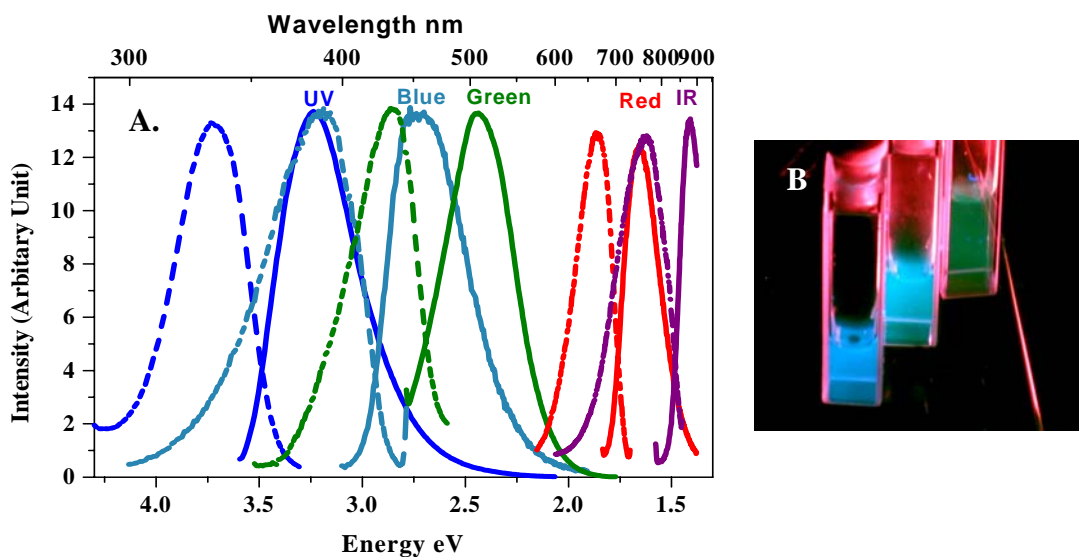


Figure 3-2-1. (A). Excitation (dashed) and emission (solid) spectra of different gold nanoclusters. Emission from the longest wavelength sample was limited by the detector response. Excitation and emission maxima shift to longer wavelength with increasing initial Au concentrations, suggesting that increasing nanocluster size leads to lower energy emission. (B) Emission from the three shortest wavelength emitting gold nanocluster solutions (from left to right) under long-wavelength UV lamp irradiation (366nm). The leftmost solution appears slightly bluer, but similar in color to Au₈ (center) [11] due to the color sensitivity of the human eye. Green emission appears weaker due to inefficient excitation at 366 nm.

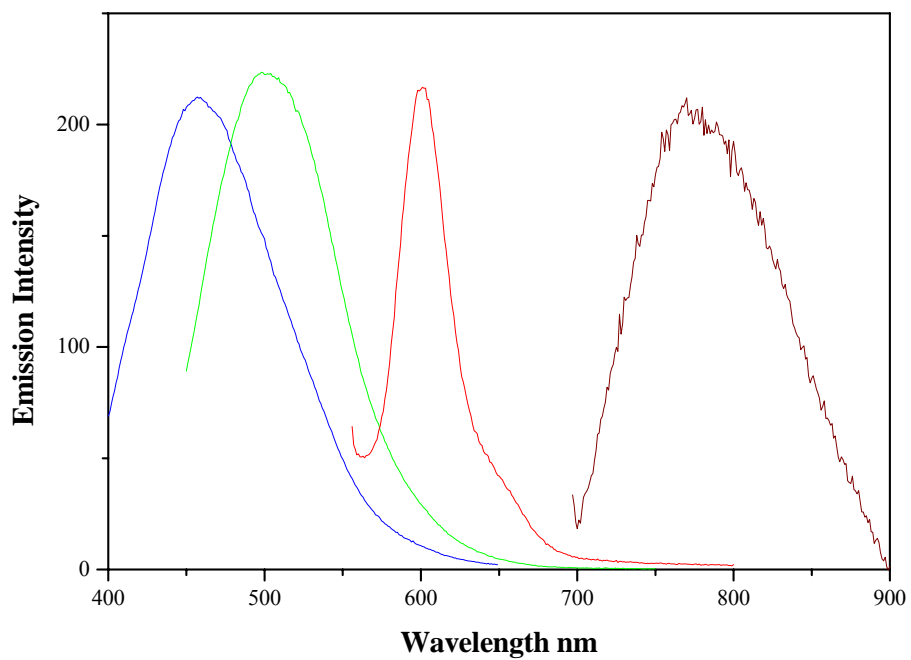


Figure 3.2.2 Emission spectra of octadecanethiol encapsulated gold nanoclusters in chloroform. Blue emitting gold clusters with maximum excitation at 365 nm. Green emitting gold clusters with maximum excitation at 430 nm. Red emitting gold clusters with maximum excitation at 586 nm. IR emitting gold clusters with maximum excitation at 650 nm.

Figure 3.2.3A, Au₈ is the dominant Au-containing species in the blue emitting solutions and its abundance linearly correlates with fluorescence intensity. In accord with stable nanoclusters having 8 valence electrons (one from each Au atom),³³ this dominant nanocluster is confirmed to be in the overall neutral oxidation state as even 100-fold excess of highly reducing BH₄⁻ does not alter the nanodot fluorescence. Confirmed through expected shifts relative to the dendrimer parent peak upon dissolution in D₂O instead of H₂O, five molecules of water were also found to be associated with the hydrophilic PAMAM dendrimer-Au complex. While five waters appears to be the favored number, smaller peaks corresponding to Au₈ with other numbers of water molecules ranging from one to six were also observed in the mass spectra of other similarly prepared samples. The peaks containing Au₈ were only observed in the fluorescent Au nanocluster solutions and fluorescence intensities of differently prepared solutions are directly proportional to relative abundances of the Au₈ nanocluster peaks alone. Additionally, Au nanocluster preparations using both HAuCl₄ and AuBr₃ yield indistinguishable fluorescent solutions with identical mass spectra. This indicates that the highly efficient blue emission results from Au₈ nanodots. In the mass spectroscopic studies of other different-color fluorescent gold nanocluster solutions, many peaks appear in the mass spectra from a combination of fragmentation and non-fluorescent products (Figure 3.2.3B). Consequently, to determine each fluorescent nanocluster size, each fluorescent solution was assayed through correlation of electrospray mass spectrometry abundances and fluorescence intensity

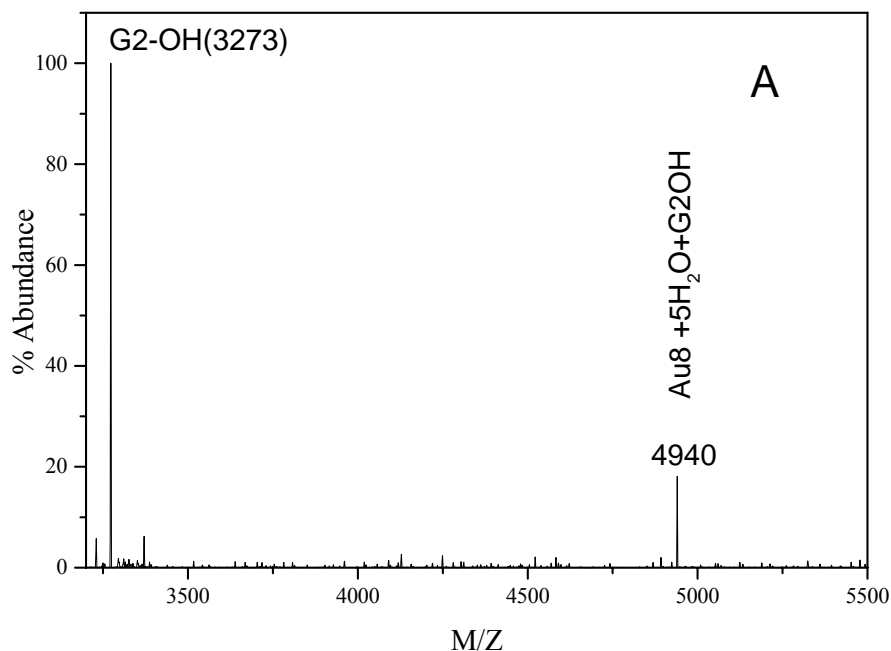


Figure 3-2-3. Fluorescent nanocluster size determinations. (A) ESI mass spectrum of G2-OH PAMAM encapsulated blue emitting (455-nm) gold nanodots. (Theoretical m/z of dendrimer G2-OH (3272) encapsulated Au_8 and $5H_2O$ is 4939) (B) A typical mass spectrum of a sample containing different fluorescent gold clusters. (C) In addition to separately identified Au_8 , nanocluster sizes (emission maxima) were determined to be Au_5 (385 nm), Au_{13} (510 nm), Au_{23} (760 nm), and Au_{31} (866 nm) through linear correlation of mass abundance and fluorescence intensity at each emission maximum. The mass abundances of all gold nanocluster solutions were measured by electrospray ionization (ESI) mass spectrometry with identical ionization conditions. The reproducible and gentle ionization procedure yielded only one mass species linear in emission intensity for each emission maximum. This one to one correspondence between mass abundance and fluorescence enabled unambiguous assignments of fluorescent gold nanocluster sizes.

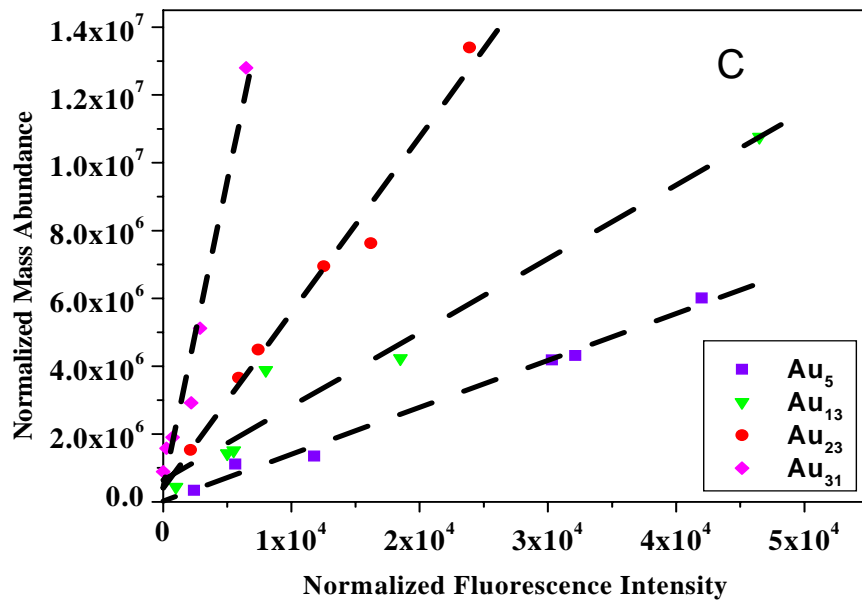
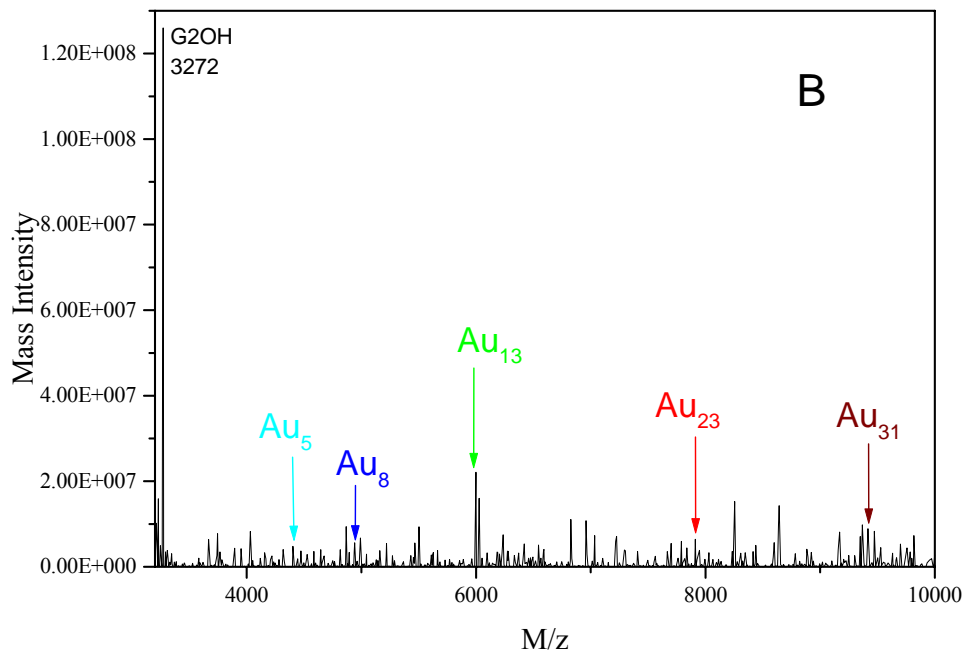


Figure 3-2-2 cont.

at each wavelength. In each case, there was a one-to-one correspondence between only one specific peak in the mass spectrum and a specific fluorescent transition. In other words, only one mass peak exhibited a linear correlation with each fluorescence peak, thereby enabling direct determination of each fluorescent nanocluster size (Figure 3.2.3C). This enables direct assignment of the UV (Au_5), green (Au_{13}), red (Au_{23}), and near IR (Au_{31}) emitting species each encapsulated within the PAMAM scaffold (“Au nanodots”). Final Au nanodot fluorescence is very stable in NaCl solution, but can be quenched with addition of Na_2S to result in the appearance of the 520nm plasmon absorption and black gold aggregates characteristic of larger Au nanoparticles.³⁴

3.2.3 Correlation of gold cluster size and its emission

The dependence of emission energy on the number of atoms, N , in each gold nanocluster (Figure 3.2.4) is quantitatively fit for the smallest nanoclusters with no adjustable parameters by the simple scaling relation of $E_{\text{Fermi}}/N^{1/3}$, in which E_{Fermi} is the Fermi energy of bulk gold.^{20,35,36} For a spherical cluster, the radius, R , is equal to $r_s \cdot N$, in which r_s is the Wigner-Seitz radius and N is the number of atoms per cluster. Identical to that for gas phase alkali metal nanocluster electronic absorption,^{21,37} the transition energy scaling with inverse cluster radius indicates that electronic structure is solely determined by the Au nanocluster free electron density and nanocluster size. This spherical jellium model has not only explained the magic sizes observed from alkali metal clusters in the gas phase, but also rationalized the gas phase plasmon absorption spectra of alkali metals. Knight and coworkers observed strong collective

electronic excitations from very small Na₆ clusters.³⁸ Haberland and coworkers also observed a strong linear decrease of the plasmon frequency as a function of R^{-1} , where R is the cluster radius.²¹ All of these results suggest that the free-electron shell-filling model corresponds exactly to the spherical jellium approximation – the simplest model for explaining delocalized, free conduction electron behavior relative to the atomic cluster core, and an excellent basic model explaining plasmon absorption in large nanoparticles.^{20,35,36}

Observation of this simple energy scaling $E_{\text{Fermi}}/N^{1/3}$ from fluorescent gold clusters offers clear and direct experimental evidence of the discrete nature of the excited state in noble metal clusters, which has long been a mystery in this field. Two different energy scaling laws for such small clusters have been proposed. Baltes and Hilf suggested the energy level spacing might be $(6/5)E_{\text{Fermi}}/N^{2/3}$ by considering the small clusters as cubic potential boxes. Kubo³⁹ produced E_f/N predictions of the electronic structure of small metal clusters based on the recognition that quasi-continuous electron energy states of bulk metals become discrete on the few-atom scale. Although both of the predications suggest the discrete energies of the metal clusters, the jellium $E_{\text{Fermi}}/N^{1/3}$ energy scaling law accurately describes the size-dependent electronic structure and relative electronic transitions of the small clusters. These quantum-confined protoplasmonic transitions of the free conduction electrons suggest nearly spherical electronic nanocluster structures with electrons bound by an approximately harmonic potential in three dimensions. While a harmonic potential would give a R^{-2} electronic transition energy dependence, as it is discussed in the

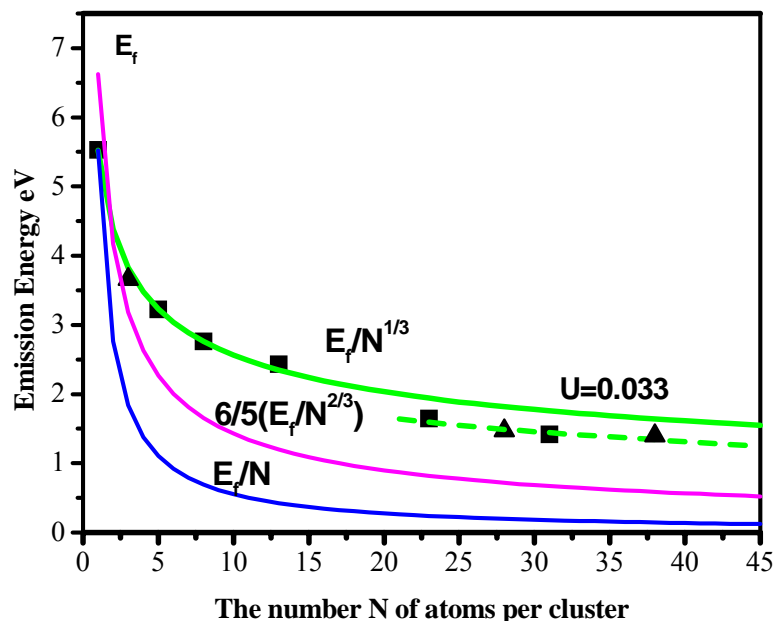


Figure 3-2-4A. Correlation of the number of atoms, N , per cluster with emission energy. Emission energy decreases with increasing number of atoms. The correlation of emission energy with N is quantitatively fit with $E_{\text{fermi}}/N^{1/3}$, as predicted by the jellium model.^{12,19} When N is equal to 1, the energy of valence electron is equal to Fermi energy because the valence electron is at the HOMO level. Emission energies of Au₂₃ and Au₃₁ exhibit slight deviations from the $E_{\text{fermi}}/N^{1/3}$ scaling. Consistent with the narrow excitation and emission spectra, the potential confining the free electrons flattens slightly for Au₂₃ and Au₃₁, with an anharmonicity of $U=0.033$. The experimental values for the emission energies of Au₃,⁴⁰ Au₂₈⁴ and Au₃₈⁴¹ are 3.66, 1.55 and 1.44 eV respectively (represented by \blacktriangle in the figure), which are all consistent with the observed scaling relations. Kubo model E_f/N and Cubic potential box model $(6/5 E_f / N^{2/3})$ proposed by Baltes and Hilf are also shown in the figure. Obviously these models can not accurately fit the emission energy scalings of the gold clusters. The Kubo model only works for gold nanowires because R is proportional to N for linear few-atom gold chains.

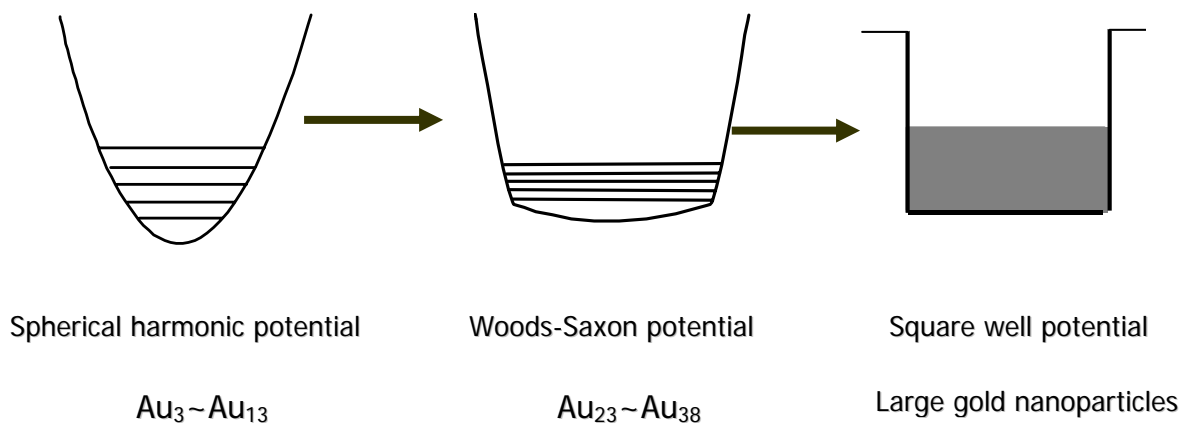


Figure 3-2-4 B Schematic of size-dependent surface potentials of gold clusters on the different size scales. For the smallest gold clusters (Au_3 to Au_{13}), cluster emission energies can be well fit with the energy scaling law $E_{fermi}/N^{1/3}$, where N is the number of atoms in each cluster, indicating that electronic structure transition of these small gold clusters are well-described by a spherical harmonic oscillator potential. With increasing size, a small anharmonic distortion term is required due to the deformation of potential well and this spherical potential surface gradually distorts into a Woods-Saxon potential surface,³⁵ and eventually becomes a cubic box potential characteristic of electrons in large metal nanoparticles.¹² These small gold clusters not only smoothly link the optical transitions from the single atom to large gold nanoparticles with observable free electron behavior but also demonstrate a smooth transition in potential confining the free electrons from that of a spherical harmonic oscillator to a cubic potential surface.

introduction chapter that the degeneracy in filling the delocalized nanocluster energy level shells (1s, 1p, 1d, 2s, 1f, 2p, ...) and the size-independent electron density for the given material yield an effective R^{-1} dependence on cluster size,^{19,20} further demonstrating the metallic origin of these Au nanocluster fluorescent transitions. Alkane thiol encapsulated Au₃ clusters recently reported by Scherer's group⁴⁰ demonstrate UV emission at 3.66eV, which is only a 4% deviation from the calculated energy for Au₃ (3.81 eV) based on this model. This suggests that emission of small gold trimer also results from the oscillation of free electrons in a spherical electronic nanocluster structure bound by an approximately harmonic potential in three dimensions.

Consideration of the effective single particle potential as a three-dimensional harmonic oscillator turns out to be very good approximation for small metal clusters (i.e. $N < 20$). However, for larger clusters, Clemenger found that a small anharmonic distortion term is required due to the deformation of the potential well.³⁵ As a result, the effective single particle Hamiltonian for electrons with mass m is

$$H = -\frac{P^2}{2m} + \frac{m\omega_0^2 q^2}{2} - U\hbar\omega_0[l^2 - n(n+3)/6] \quad [15]$$

, in which P and q are single electron momentum and coordinate operators. l is the angular momentum and n is the shell number. U is the distortion parameter. The third,

anharmonic term takes care of the shape change of the potential surface. An energy eigenvalue is³⁵

$$E_n = h\omega_0 \left\{ \left[\left(n + \frac{3}{2} \right) - U \left(l^2 - n(n+3) / 6 \right) \right] \right\} \quad [16]$$

, in which $h\omega_0$ is equal to $E_f/N^{1/3}$. Energy level spacing for large metal clusters should be³⁵

$$\Delta E_{\text{emission}} = \frac{E_f}{N^{1/3}} \left[1 - U \left(l_e^2 - l_g^2 - \frac{n+2}{3} \right) \right] \quad [17]$$

in which l_e and l_g are the angular momentum of the excited and ground state respectively. Indeed, the distortion of surface potential well is observed from the larger fluorescence gold clusters (N=23 and 31). Electron screening increases and the potential bounding each electron flattens, thereby slightly increasing the anharmonicity. Figure 3-2-4B shows that the potential confining free electrons in larger gold clusters Au₂₃ and Au₃₁ flattens only slightly, indicated by an anharmonicity distortion parameter^{20,35} of U~0.033 based on equation 17. Even the HOMO-LUMO gaps from gas phase Au₂₀⁶ and water soluble Au₁₁⁴² and Au₂₈⁴ lie close to the same curves and are consistent with our results (Figure 3-2-4A). More recently, Au₃₈ reported by Murray's group gives IR emission with maximum energy at 1.41 eV,⁴¹ which is about a 3% deviation from our calculated value (1.48 eV), further suggesting the distortion parameter (U=0.033) remains constant even at particle sizes as large as 38 atoms. While only magic cluster sizes correspond to shell

closings,³⁵ the approximately spherical electronic structure indicated by the scaling with inverse cluster radius shows that these nanomaterials are “multi-electron artificial atoms”.^{19,43,44} This similarity results from the conduction electrons making intraband transitions between nanocluster electronic states of well-defined angular momentum, thereby leading to discrete excitation and emission spectra. The primary difference between these and true atoms is that the electron density does not change in the clusters, while it does as atomic number increases.^{19,20} Consequently, for atoms, electrons can be considered in a r^{-1} potential well due to Columbic interaction and the magic numbers N_0 for the r^{-1} potential are 4,10, 18..., corresponding to 1s, 2s, 2p, 3s, 3p, 3d.... electronic shells. However an electron in a metal cluster is in the spherical harmonic oscillator r^2 potential and the magic numbers N_0 for the r^2 potential are 2,8,18,20..., corresponding to 1s, 1p, 1d, 2s,.... electronic shells.²² In contrast to predictions of planarity for gas phase $Au_{N \leq 7}$ nanoclusters in gas phase (Energy level spacing should be equal to $E_f / (\sqrt{2r_s N})$),¹⁶ the PAMAM-encapsulated nanocluster geometries must be approximately spherical to yield the observed scaling.

3.2.4 Photophysical properties of fluorescent gold clusters

The detailed photophysical properties of different water-soluble gold nanoclusters (Table I) indicate that these Au nanodots behave as not only quantum-confined, but also molecular-like and size-tunable fluorophores. The high quantum yields are comparable to the best water-soluble emitters currently available, ranging from 70% for UV-emitting Au_5 to ~10% for Au_{31} in the near IR. In contrast to larger semiconductor nanocrystals, dendrimer encapsulated gold clusters have well-defined

excitation and emission spectra while requiring neither complicated high temperature syntheses with toxic precursors nor difficult overcoating with surface passivation and solubilization chemistry for applicability as biolabels. Since semiconductor nanocrystals have band structures, any energy above the nanocrystal band gap can excite the semiconductor nanocrystals, which leads to broad excitation spectra and limit their applications as energy transfer pairs. However, molecule-like gold clusters have discrete energy states and both their excitation and emission spectra are strongly influenced by their sizes, thereby offering new opportunities to apply them as energy transfer pairs in the biological labeling studies. Such well-defined, tunable discrete excitation and emission suggest that these nanomaterials may find utility as energy transfer pairs – a task that semiconductor quantum dots are ill-suited for because of their extremely broad excitation spectra and larger fluorophore size. Gold clusters also exhibit low toxicity, in contrast to II-VI or III-V semiconductors. Size-dependent emission of gold begins at several atoms and strongly depends on the number of atoms in the clusters. Emission can be tuned from the UV to the near IR by simply adjusting the number of atoms in the clusters, while remaining below 1 nm in diameter. Characteristic lengths of semiconductor range from 2-10 nm with surface passivation and solubilization chemistry for the increasing size up to ~20 nm. As gold nanoclusters are too small to have the continuous density of states and plasmon absorptions characteristic of larger nanoparticles (>2 nm),^{45,46} the transition energy instead of the plasmon absorption width should scale with inverse cluster radius. While there is great debate regarding size-induced metal to insulator

transitions and the nature/lack of plasmon absorption in few-atom metal nanoclusters,^{18-20,47} the size-dependent scaling of excitation and emission energies with $E_{\text{Fermi}}/N^{1/3}$ directly indicates that free electron behavior begins in Au_N as small as $N=3$. The relative difference between the energy level spacing and thermal energy has become a criterion to distinguish metallic conduction from insulation.⁴⁸ If the energy level spacings are smaller than the thermal energy, thermal energy can create mobile electron-hole pairs in the metals, as a result, current can flow through the metals.⁴⁸ However, if the energy level spacings are much larger than the available thermal energy, the free electrons in the metal clusters are confined to discrete energy levels. Thus, very small metal clusters are often considered to be nonmetallic. Free electron behavior can be clearly observed from metal nanoparticles and molecule-scale metal clusters.

Such free electron protoplasmonic intraband absorption and fluorescence give rise to discrete size-dependent Au transitions throughout the visible beginning at the few-atom size scale. As nanocluster size increases further, transition energies decrease with the increasing density of states, thereby forcing energy level spacings to eventually become comparable to available thermal energy. This relaxes the angular momentum selection rules as single electron states become less well defined in favor of the effectively continuous density of states characteristic of plasmon absorption within nanoparticles and bulk metals. As a result, the nanoparticle absorption is mainly due to collective oscillations of free electrons, and its plasmon

Table 3-1. Photophysical properties of PAMAM-encapsulated gold nanoclusters in water

Gold Cluster	Excitation (FWHM) eV	Emission (FWHM) eV	Quantum Yield %	Lifetime ns	Intrinsic decay rate($\times 10^9$ GHz)
Au ₅	3.76 (0.42)	3.22 (0.45)	70	3.5	0.2
Au ₈	3.22 (0.54)	2.72 (0.55)	42	7.5	0.056
Au ₁₃	2.86 (0.38)	2.43 (0.41)	25	5.2	0.048
Au ₂₃	1.85 (0.21)	1.65 (0.26)	15	3.6	0.042
Au ₃₁	1.62 (0.20)	1.41 (0.10)	10	-	-

absorption width is solely dependent on its relaxation constant that is proportional to $(1/R)$.¹² Absorption is governed by $k(N)$, the size-dependent imaginary part of the refractive index, $n'(N)=n(N)+ik(N)$, while plasmon width results from the imaginary portion of the dielectric constant, $\epsilon(N)=\epsilon_1(N)+i\epsilon_2(N)$. Because $\epsilon(N)=n'(N)^2$ for non-magnetic materials, $\epsilon(N)=[n(N)]^2 - [k(N)]^2 + 2i \cdot n(N) \cdot k(N)$ and the portion governing the plasmon width is simply $\epsilon_2(N) = 2 \cdot n(N) \cdot k(N)$, and is linearly dependent on $k(N)$. Therefore, any size dependence in absorption is directly related to the imaginary portion of the dielectric constant which governs plasmon width, thereby connecting the atomic and nanoparticle limits. Consequently, by directly probing the lowest energy absorptions and emissions, these studies connect nanocluster transition energies and both of which scale with inverse particle radius (R^{-1} or, equivalently, $N^{-1/3}$). With increasing size and decreasing transition energy, confinement switches from being relative to the Fermi wavelength (yielding discrete size-dependent optical transitions) to being relative to the electron mean free path (yielding plasmon widths that scale with the free electron DOS and the imaginary dielectric constant). Both regimes scale with inverse cluster radius as the delocalized free electron states giving rise to nanocluster fluorescence become sufficiently dense at larger sizes that they enable the Au nanoparticle plasmon absorptions and generate the characteristic $N^{-1/3}$ scaling of the plasmon width. Consequently, the size dependent transition frequencies of our water soluble Au nanoclusters are the small size limit of the plasmon absorption within bulk metals and provide a smooth connection between atomic and

metallic behavior with true protoplasmonic fluorescence that is well-described at all sizes by the spherical jellium model.³⁸

3.2.5 Photon antibunching experiments for single Au₂₃ clusters

Although a single metal atom is a well-defined quantum system, metal nanoparticles and bulk metals are not typically expected to behave as single quantum systems due to the characteristic collective oscillations of free electrons under optical excitation. When incident light passes through the bulk metal or metal nanoparticles, scattered photons resulting from this oscillation are uncorrelated, thereby preventing observation of non-classical photon correlations. Fortunately, since electronic structures of metals dramatically change at the electron Fermi wavelength, splitting of continuous band structures into discrete energy levels may provide a unique opportunity to observe the photon antibunching behavior from few atom metal clusters. On the electron Fermi wavelength scale, free electrons can be described as being confined in discrete energy levels of metal clusters. Because these energy level spacings are large relative to thermal energy, these metal nanoclusters should behave as single quantum systems, not the sum of many quantum systems. To prove the quantum nature of these fluorescent gold clusters, photon antibunching measurements were performed on these gold clusters.

Here, we demonstrate the observation of photon antibunching from fluorescent Au₂₃ clusters. Au₂₃ clusters were dispersed on a coverslip, which formed the bottom window of a microscope-mounted vacuum chamber ($<10^{-5}$ torr). Adjusting the concentration of Au₂₃ enables a single molecule to be excited with a

CW 633 nm HeNe laser. Although well-defined dipole emission patterns⁴⁹ and blinking dynamics are readily observed, only antibunching in the photon stream definitively proves single molecule behavior. Measurement of photon correlations on individual gold Au₂₃ nanoclusters was performed in a Hanbury Brown and Twiss configuration.⁵⁰ In such an arrangement, the probability of detecting two individual photons was measured as a function of arrival time difference. Since simultaneous two photon emission at low excitation intensity is forbidden for a single quantum system, the intensity autocorrelation function $g^{(2)}(\tau)$ ideally should be close to zero at zero delay. Strong antibunching was observed from photons emitted from a single Au₂₃ cluster. Minimum coincidence counts at zero delay and an exponential increase of $g^{(2)}(\tau)$ before and after zero delay are clear evidence for non-classical photon antibunching (shown in Figure 3.2.5). In contrast, the ensemble $g^{(2)}(\tau)$ yields no minimum at zero delay. Overall these observations suggest that electronic structure and optical transitions dramatically change at the few-atom scale and that the conduction electrons are in well-defined electronic states and give rise to this novel “Multielectron artificial atom” behavior in Au nanoclusters. To simulate this autocorrelation of photons, we used a simple two level model to fit $g^{(2)}(\tau) = 1 - (1/N)e^{-\tau/t_d}$,⁵¹ in which t_d is the decay time. The fit gives an estimate of $g^{(2)}(0) = 0.6$, which is a clear signature of non-classical photon antibunching from a single quantum system. Theoretically, intensity correlation $g^{(2)}(\tau)$ of emitted light from a single two level quantum system at zero delay should be exactly zero, however, the background observed in our experiments arise from impurity fluorescence under laser excitation.

A weak but broad emission at 680 nm was observed even without presence of Au₂₃ clusters. This background is responsible for at least 20% contrast decrease. A possible method to improve the contrast is using 720 nm long pass filter to cut off the background, and experiments are being carried out. Single molecule lifetime of individual gold clusters obtained from fitting results is 3.6 ns, identical to the bulk lifetime. Such single quantum system behavior has not been previously reported for metals at any size regime. This direct photon antibunching result provides the optical evidence for these “multielectron” artificial atoms behaving as single quantum systems. Although Au₂₃ is composed of a group of individual atoms, the free electron delocalized in the clusters and their behaviors are governed by angular momentum. Clearly acting as true multielectron artificial atoms, only emission arising from single electron decay instead of collective excitations is observed. These studies shed light on the electronic structure change from a many body quantum system to a single quantum system with size decreasing to the molecular metal scale corresponding to Fermi wavelength of an electron. Different to their counterpart large gold nanoparticles, single rather than collective electron transitions are observed in these small gold clusters. Large energy spacings and well-defined angular momentum states are responsible for this change at the nanocluster level. Observation of antibunching from gold clusters at room temperature also provides an opportunity to utilize these sub-nm gold clusters as new non classical light sources.

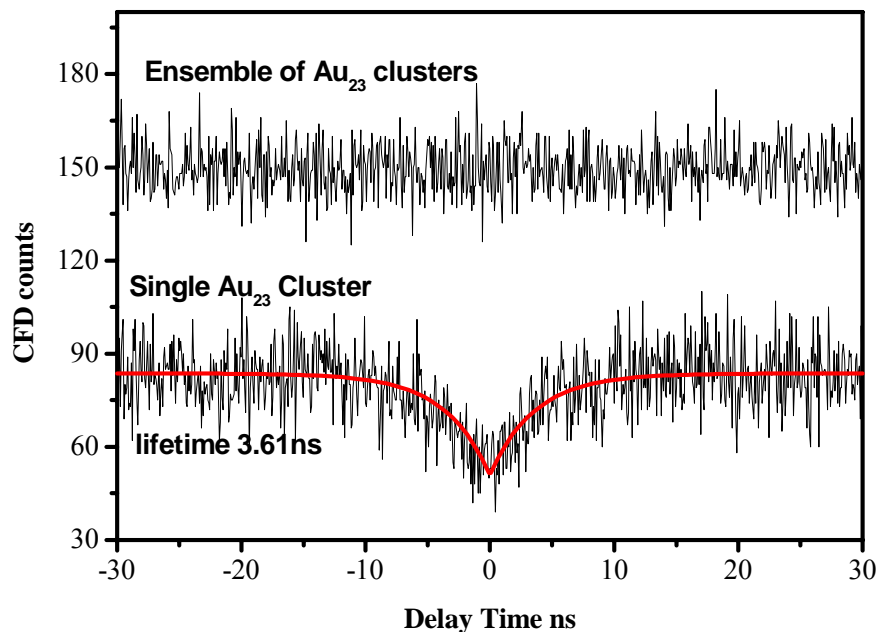


Figure 3-2-5 Measurement of photon correlations on individual gold Au_{23} nanoclusters (bottom) and the ensemble of gold clusters (top) performed in a Hanbury Brown and Twiss configuration. At zero delay, photons emitted by the ensemble of gold clusters are uncorrelated and $g^{(2)}(\tau)$ is equal to 1. However, for a single molecule, the probability of observing two photons at zero delay is the lowest and increases with delay time between photons. The red curve is a simulation based on the equation $g^{(2)}(\tau) = 1 - (1/N)e^{-\tau/t_d}$ with t_d as the decay time. Based on this equation, the $g^{(2)}(0)$ is 0.6 and lifetime of single Au_{23} is 3.6 ns, which is consistent with experimental results from bulk solution studies.

3.3 Conclusion

We have created novel, highly fluorescent gold quantum dots that behave as multi-electron artificial atoms with size-tunable, discrete electronic transitions between states of well-defined angular momenta. Correlation of Au nanocluster sizes with transition energies are well-fit with the simple relation, $E_{\text{fermi}}/N^{1/3}$, indicating protoplasmonic fluorescence corresponding to the jellium model because both fluorescence and plasmon scattering are due to free electron behavior but under different boundary conditions. Both plasmon width and cluster emission are proportional to $1/R$. Thus, the intraband transitions are the low number limit of the plasmon before the onset of collective dipole oscillations occurring when a continuous density of states is reached. Combination of this photon antibunching behavior at the single molecule level with their discrete size-dependent optical transitions demonstrate that these small gold clusters are true multielectron artificial atoms. Providing the “missing link” between atomic and nanoparticle behavior in noble metals, these highly fluorescent, water-soluble Au nanoclusters offer complementary transition energy size scalings at smaller dimensions than do semiconductor quantum dots. The unique discrete excitation and emission coupled with facile creation in aqueous solution open new opportunities for noble metal nanoclusters as biological labels, energy transfer pairs, and other light emitting sources in nanoscale electronics.

3.4 References

1. Empedocles, S. & Bawendi, M. Spectroscopy of single CdSe nanocrystallites. *Accounts Chem. Res.* **32**, 389-396 (1999).
2. El-Sayed, M. A. Some interesting properties of metals confined in time and nanometer space of different shapes. *Accounts Chem. Res.* **34**, 257-264 (2001).
3. Link, S. & El-Sayed, M. A. Shape and size dependence of radiative and non-radiative and photothermal properties of gold nanocrystals. *Int. Rev. Phys. Chem.* **19**, 409-453 (2000).
4. Link, S. et al. Visible to infrared luminescence from a 28-atom gold cluster. *J. Phys. Chem. B* **106**, 3410-3415 (2002).
5. Chen, S. W. et al. Gold nanoelectrodes of varied size: Transition to molecule-like charging. *Science* **280**, 2098-2101 (1998).
6. Li, J., Li, X., Zhai, H. J. & Wang, L. S. Au-20: A tetrahedral cluster. *Science* **299**, 864-867 (2003).
7. Felix, C. et al. Ag-8 fluorescence in argon. *Phys. Rev. Lett.* **86**, 2992-2995 (2001).
8. Peyser, L. A., Vinson, A. E., Bartko, A. P. & Dickson, R. M. Photoactivated fluorescence from individual silver nanoclusters. *Science* **291**, 103-106 (2001).
9. Zheng, J., Stevenson, M. S., Hikida, R. S. & Van Patten, P. G. Influence of pH on dendrimer-protected nanoparticles. *J. Phys. Chem. B* **106**, 1252-1255 (2002).

10. Huang, T. & Murray, R. W. Visible luminescence of water-soluble monolayer-protected gold clusters. *J. Phys. Chem. B* **105**, 12498-12502 (2001).
11. Wilcoxon, J. P., Martin, J. E., Parsapour, F., Wiedenman, B. & Kelley, D. F. Photoluminescence from nanosize gold clusters. *J. Chem. Phys.* **108**, 9137-9143 (1998).
12. Kreibig, U. & Vollmer, M. *Optical Properties of Metal Clusters* (Springer, 1995).
13. Alvarez, M. M. et al. Optical absorption spectra of nanocrystal gold molecules. *J. Phys. Chem. B* **101**, 3706-3712 (1997).
14. Barnett, R. N. et al. Structures and spectra of gold nanoclusters and quantum dot molecules. *European Physical Journal D* **9**, 95-104 (1999).
15. Cleveland, C. L., Landman, U., Shafigullin, M. N., Stephens, P. W. & Whetten, R. L. Structural evolution of larger gold clusters. *Z. Phys. D-Atoms Mol. Clusters* **40**, 503-508 (1997).
16. Hakkinen, H. & Landman, U. Gold clusters (Au-N, $2 \leq N \leq 10$) and their anions. *Phys. Rev. B* **62**, R2287-R2290 (2000).
17. Huang, T. & Murray, R. W. Visible luminescence of water-soluble monolayer protected gold clusters. *J. Phys. Chem. B* **105**, 12498-12502 (2001).
18. Nilius, N., Wallis, T. M. & Ho, W. Development of one-dimensional band structure in artificial gold chains. *Science* **297**, 1853-1856 (2002).
19. Haberland, H. *Clusters of Atoms and Molecules* (ed. Haberland, H.) (Springer-Verlag, 1994).

20. Deheer, W. A. The Physics of Simple Metal-Clusters - Experimental Aspects and Simple-Models. *Reviews of Modern Physics* **65**, 611-676 (1993).
21. Reiners, T., Ellert, C., Schmidt, M. & Haberland, H. Size Dependence of the Optical-Response of Spherical Sodium Clusters. *Phys. Rev. Lett.* **74**, 1558-1561 (1995).
22. Johnston, R. L. *Atomic and Molecular Clusters* (Taylor&Francis, London and New York, 2002).
23. Konig, L., Rabin, I., Schulze, W. & Ertl, G. Chemiluminescence in the agglomeration of metal clusters. *Science* **274**, 1353-1355 (1996).
24. Palpant, B. et al. Optical properties of gold clusters in the size range 2-4 nm. *Phys. Rev. B* **57**, 1963-1970 (1998).
25. Marcus, R. a. S. N. *Physics and chemistry of small clusters / edited by P. Jena, B.K. Rao, and S.N. Khanna.* (New York : Plenum Press, 1987).
26. Harbich, W., Fedrigo, S., Buttet, J. & Lindsay, D. M. Deposition of Mass Selected Gold Clusters in Solid Krypton. *J. Chem. Phys.* **96**, 8104-8108 (1992).
27. Fedrigo, S., Harbich, W. & Buttet, J. Optical-Response of Ag₂, Ag₃, Au₂, and Au₃ in Argon Matrices. *J. Chem. Phys.* **99**, 5712-5717 (1993).
28. Bigioni, T. P., Whetten, R. L. & Dag, O. Near-infrared luminescence from small gold nanocrystals. *J. Phys. Chem. B* **104**, 6983-6986 (2000).
29. Nilius, N., Ernst, N. & Freund, H. J. Photon emission from individual supported gold clusters: thin film versus bulk oxide. *Surf. Sci.* **478**, L327-L332 (2001).

30. Mooradian, A. Photoluminescence of metals. *Phys. Rev. Lett.* **22**, 185-187 (1969).
31. Balogh, L. & Tomalia, D. A. Poly(amidoamine) dendrimer-templated nanocomposites. 1. Synthesis of zerovalent copper nanoclusters. *J. Am. Chem. Soc.* **120**, 7355-7356 (1998).
32. Lee, W. I., Bae, Y. J. & Bard, A. J. Strong blue photoluminescence and ECL from OH-terminated PAMAM dendrimers in the absence of gold nanoparticles. *J. Am. Chem. Soc.* **126**, 8358-8359 (2004).
33. Lin, Z. Y., Kanters, R. P. F. & Mingos, D. M. P. Closed-Shell Electronic Requirements for Condensed Clusters of the Group-11 Elements. *Inorg. Chem.* **30**, 91-95 (1991).
34. Garcia-Martinez, J. C., Scott, R. W. J. & Crooks, R. M. Extraction of monodisperse palladium nanoparticles from dendrimer templates. *J. Am. Chem. Soc.* **125**, 11190-11191 (2003).
35. Clemenger, K. Ellipsoidal Shell Structure in Free-Electron Metal-Clusters. *Phys. Rev. B* **32**, 1359-1362 (1985).
36. Knight, W. D. et al. Electronic Shell Structure and Abundances of Sodium Clusters. *Phys. Rev. Lett.* **52**, 2141-2143 (1984).
37. Deheer, W. A. et al. Collective Dipole Oscillations in Small Sodium Clusters. *Phys. Rev. Lett.* **59**, 1805-1808 (1987).
38. Selby, K. et al. Photoabsorption Spectra of Sodium Clusters. *Phys. Rev. B* **43**, 4565-4572 (1991).
39. Kubo, R. Electronic Properties of Metallic Fine Particles .1. *J. Phys. Soc. Jpn.* **17**, 975-& (1962).

40. Jin, R. C., Egusa, S. & Scherer, N. F. Thermally-induced formation of atomic Au clusters and conversion into nanocubes. *J. Am. Chem. Soc.* **126**, 9900-9901 (2004).
41. Lee, D., Donkers, R. L., Wang, G. L., Harper, A. S. & Murray, R. W. Electrochemistry and optical absorbance and luminescence of molecule-like Au-38 nanoparticles. *J. Am. Chem. Soc.* **126**, 6193-6199 (2004).
42. Bartlett, P. A., Bauer, B. & Singer, S. J. Synthesis of Water-Soluble Undecagold Cluster Compounds of Potential Importance in Electron-Microscopic and Other Studies of Biological-Systems. *J. Am. Chem. Soc.* **100**, 5085-5089 (1978).
43. Brus, L. E. Electron Electron and Electron-Hole Interactions in Small Semiconductor Crystallites - the Size Dependence of the Lowest Excited Electronic State. *J. Chem. Phys.* **80**, 4403-4409 (1984).
44. Alivisatos, A. P. Semiconductor clusters, nanocrystals, and quantum dots. *Science* **271**, 933-937 (1996).
45. Kim, Y. G., Oh, S. K. & Crooks, R. M. Preparation and characterization of 1-2 nm dendrimer-encapsulated gold nanoparticles having very narrow size distributions. *Chem. Mat.* **16**, 167-172 (2004).
46. Zheng, J., Petty, J. T. & Dickson, R. M. High quantum yield blue emission from water-soluble Au-8 nanodots. *J. Am. Chem. Soc.* **125**, 7780-7781 (2003).
47. Thomas, O. C., Zheng, W. J., Xu, S. J. & Bowen, K. H. Onset of metallic behavior in magnesium clusters. *Phys. Rev. Lett.* **89**, art. no.-213403 (2002).
48. Wertheim, G. K., Diczko, S. B. & Buchanan, D. N. E. Noble-Metal and Transition-Metal Clusters - the D-Bands of Silver and Palladium. *Phys. Rev. B* **33**, 5384-5390 (1986).

49. Dickson, R. M., Norris, D. J. & Moerner, W. E. Simultaneous imaging of individual molecules aligned both parallel and perpendicular to the optic axis. *Phys. Rev. Lett.* **81**, 5322-5325 (1998).
50. Hanbury-Brown, R. H. & Twiss, R. Q. Correlation between photons in coherent light rays. *Nature* **178**, 1447-8 (1956).
51. Michler, P. et al. Quantum correlation among photons from a single quantum dot at room temperature. *Nature (London)* **406**, 968-970 (2000).

CHAPTER 4

Luminescent Gold Nanoparticles

4.1 Introduction

Electronic structures of metals are not only dependent on their sizes but also strongly correlated with the oxidation states of metal atoms. As a result, research into the chemistry and physics of small metal clusters has been driven by different objectives in the last decades.^{1,2} One objective is the understanding of size-dependent properties of metals along the atom to bulk transition by creating different size, fully reduced metal clusters and nanoparticles. The other is the understanding of interactions between metal ions and organic ligands by creating metal(I/II/III) complexes.

We and others have demonstrated that the optical and electronic properties of nanoscale gold clusters are determined by nanocluster size, with the scaffold providing a seemingly smaller perturbation.^{3,4} As a result, small gold clusters or nanoparticles can be roughly visualized as fragments of bulk gold with minor perturbation in electronic structures by organic matrices and the properties of metal clusters or nanoparticles are dominated by various size effects.²⁻⁴ In fluorescent gold nanoclusters, gold atoms are fully reduced and strong covalent bonds were observed

among these gold atoms. Emission is simply dependent on the number of free electrons in the clusters and can be well fit with the simple free electron, or jellium, model.⁴

In addition to these fluorescent and fully reduced gold clusters, small gold(I) complexes are also found to give bright luminescence.⁵⁻¹⁴ In these luminescent gold(I) clusters, gold ions provide available states and hybridize with organic ligands by forming charge transfer bands.⁵⁻¹⁴ Luminescence is roughly attributed to metal to metal electronic transitions, coupling with strong ligand to metal/metal-metal unit charge transfer transitions. Large Stokes-shifted luminescence with μs lifetimes are generally characteristics of these gold(I) complexes. Charge transfer between ligand and gold or gold-gold unit is responsible for the observed large Stokes shift and long-lifetime emission. The emission center is usually assigned to metal-metal electronic transitions and emission energy is inversely proportional to gold-gold distance at low temperature.^{14,15} In addition, lowering the temperature can result in the decrease of Au(I)-Au(I) bond length, corresponding to a blue shift of the emission energy.¹⁶

A general strategy for synthesizing luminescent small gold(I) clusters is using multidentate ligands¹⁷ with “soft” electron donor groups to coordinate with Au^{3+} ions. With assistance of closed-shell interactions among Au(I) ions ($5d^{10}$) and bridging structures of the ligand groups,⁹ small luminescent gold(I) clusters can be prepared. In these luminescent gold(I) clusters, closed-shell interactions drive aggregation of Au(I) atoms to form dimers and oligomers. The multidentate ligands are necessary to stabilize gold(I) complexes/clusters because bond energies of gold(I)-gold(I) ranging

from 20-50 kJ are much smaller than those of gold(0)-gold(0) in fully reduced gold nanoparticles or clusters.¹⁸ The average gold(I)-gold(I) distance (2.69-3.35 Å) in such gold(I) clusters is also shorter than the sum (3.7 Å) of the two van der Waals radii of gold(I) ions but is longer than Au(0)-Au(0) distance (2.2-2.5 Å).¹⁸

Studies on luminescent polynuclear gold(I) complexes/clusters suggest that if surface atoms in gold nanoparticles are in high oxidation states, they might exhibit luminescence by forming ligand-metal charge-transfer band and metal(I)-metal(I) interactions. In thesis, we found that luminescent gold nanoparticles can be created by using a very gentle photoreduction method. These nanoparticles might have applications as a new type of nanoscale emitters in biological labeling and optoelectronic devices.

4.2 Results and discussion

4.2.1 Synthesis

Glutathione¹⁹⁻²³, a three amino acid peptide, was used as an encapsulant to synthesize water-soluble and biocompatible luminescent gold nanoparticles. The detailed synthetic procedure has been described in Chapter 2. Distinct from synthesis of nonluminescent but plasmonic gold nanoparticles, no strong reducing reagents or strong photoirradiation was used in the synthesis of these luminescent gold nanoparticles. The glutathione/gold solution was stirred for 3 days at room temperature under room-light irradiation. This gentle reduction method may leave some Au atoms in higher oxidation states, giving a slight effective partial positive charge to all Au atoms in the nanoparticles. Both yellow and red emitting gold

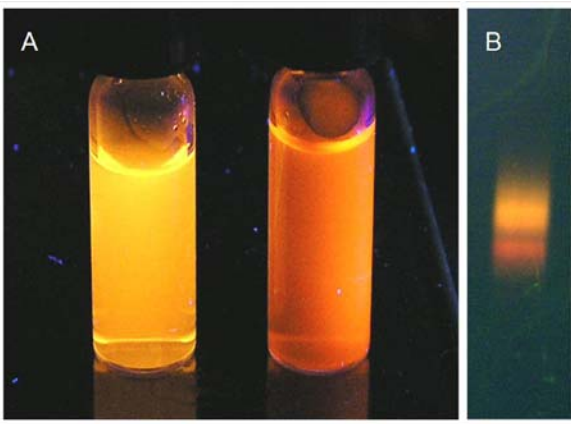


Figure 4-2-1 Luminescence images of glutathione encapsulated gold nanoparticles (a). Luminescence image of glutathione-encapsulated yellow and red emitting gold nanoparticles in aqueous solution under 366 nm excitation. (b) Luminescence image of yellow and red emitting gold nanoparticles in poly(acrylamide) gel after electrophoretic separation.

nanoparticles were readily created with the methods in Chap2.. Figure 4.2.1A shows yellow and red emitting gold nanoparticles have been prepared within glutathione scaffolds, and they strongly emit under irradiation at 360 nm. Figure 4.2.1B shows that red and yellow emitting species are separable with poly (acryl amide) gel electrophoresis. Yellow emitting species usually run more slowly than red emitting species toward the positive electrode in electrical field, indicating a combination of large size and/or less negative overall charge.

4.2.2 Size characterization with Transmission Electron Microscopy

Luminescent gold nanoparticle solutions were deposited on copper TEM grids. After solvent evaporation, the TEM grids with samples were characterized by field emission transmission electron microscopy (TEM) (Hitachi HF-2000 FEG at 200 kV) and high-resolution transmission electron microscope (HRTEM) (JEOL 4000EX at 400 kV). All TEM images were collected immediately without long irradiation by electron beams to ensure that observed particles are not due to the reduction by the electron beam. TEM images and size-distributions for the compounds are shown in Figure 4.2.2 respectively, indicating nanoparticle sizes around 2 nm. As a control experiment, “polymeric” Au(I)SR was also synthesized based on the Brust method²⁴ and investigated with TEM, however, no gold nanoparticles were observed under the same experimental conditions. Size distributions for yellow emitting gold nanoparticles and red emitting gold nanoparticles are 2.2 ± 0.3 and 1.9 ± 0.3 nm, respectively. HRTEM (high resolution TEM) measurements further indicated that these gold nanoparticles have well-defined crystal structures (Figure 4.2.3). Since no

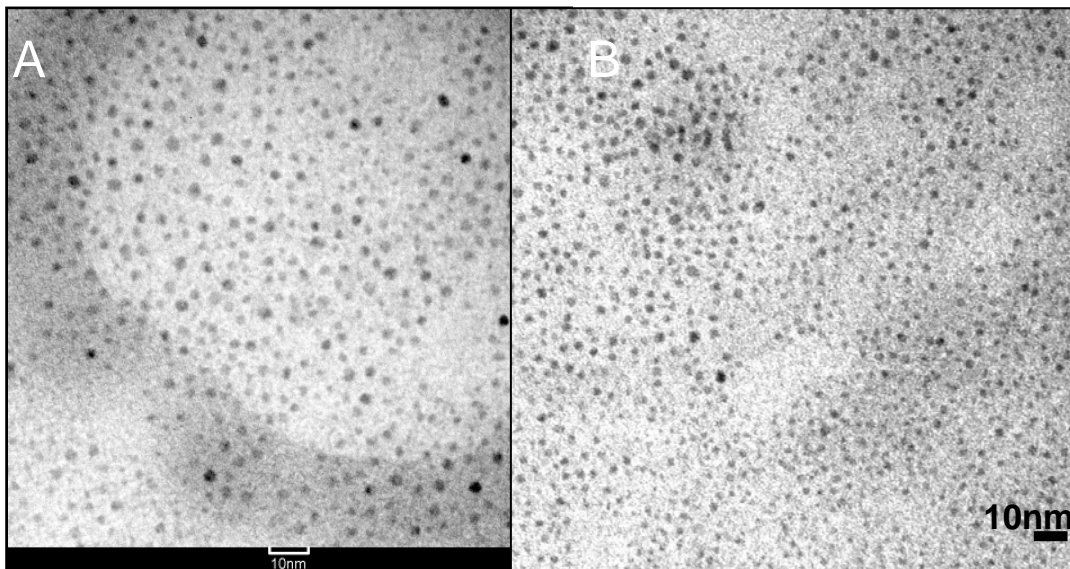


Figure 4-2-2 TEM measurements on the luminescent gold nanoparticles. TEM images of red (A) and yellow (B) emitting gold nanoparticles collected using field emission transmission electron microscope (TEM) (Hitachi HF-2000 FEG at 200 kV). Size distribution of glutathione encapsulated red emitting (C) and yellow emitting gold nanoparticles (D) are 1.9 ± 0.3 nm and 2.2 ± 0.3 , respectively (Total the number of gold nanoparticles counted is 100 for yellow and red emitting gold nanoparticles, respectively).

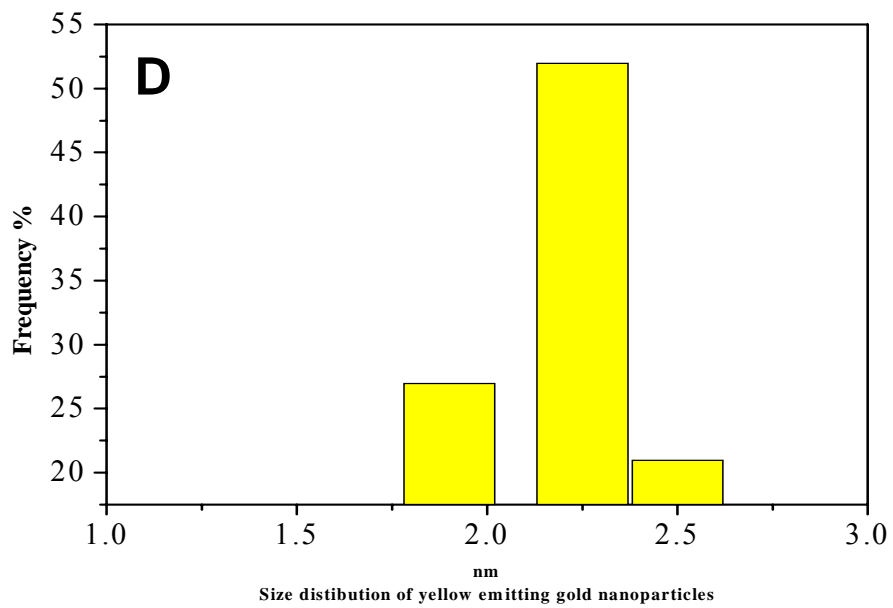
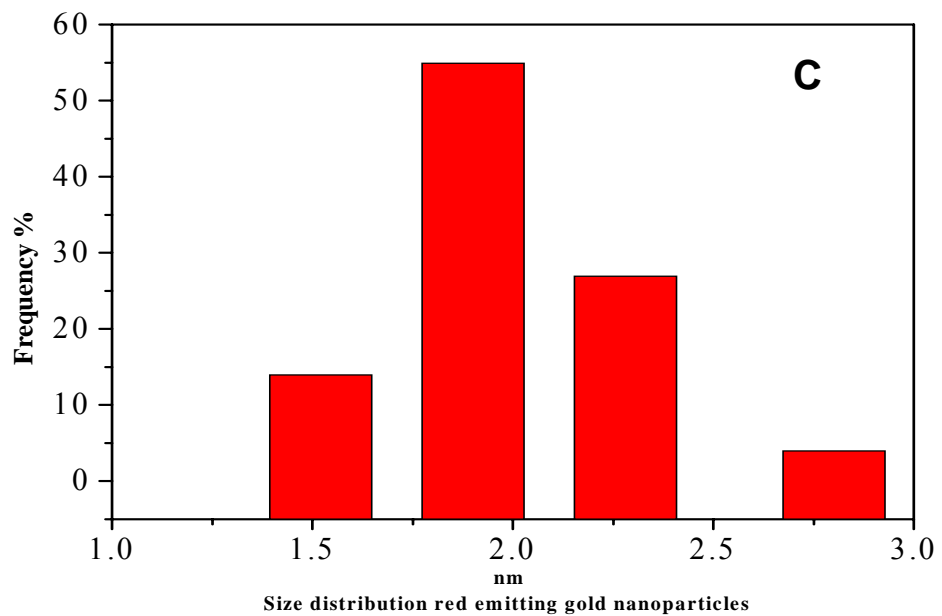


Figure 4-2-2 cont.

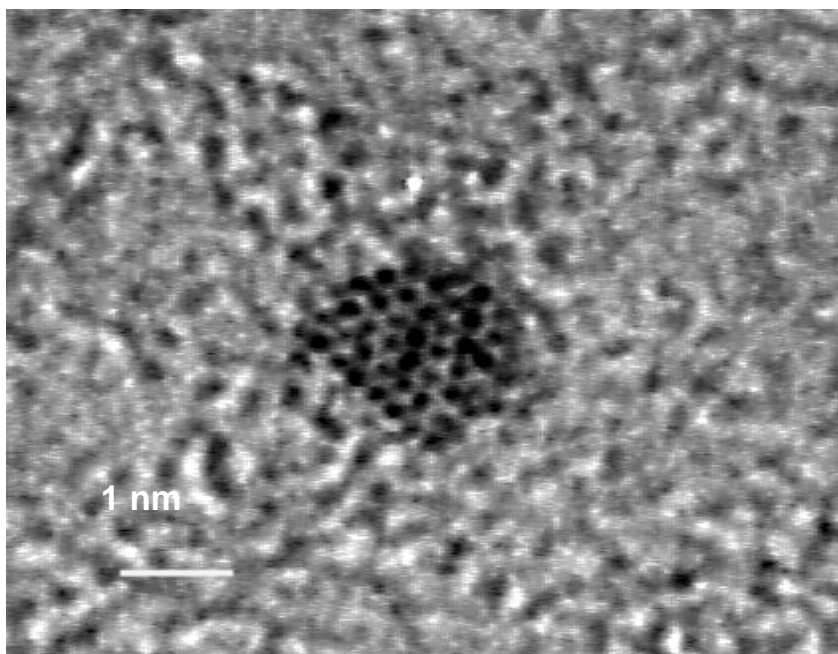


Figure 4-2-3 A lattice image of a single red emitting gold nanoparticle collected with high-resolution transmission electron microscopy (HRTEM) (JEOL 4000EX at 400 kV).

chemical reducing agents were used in the preparation of these luminescent gold nanoparticles, the driving force in the formation of these luminescent gold nanoparticles is probably attributed to photoreduction and disproportionation of some gold salts within glutathione scaffolds.²⁵ El-Sayed et al. recently reported that Au³⁺ was first reduced to Au(1+) and then Au(1+) was decomposed to Au(3+) and Au(0).²⁵ Au(0) atoms aggregated into the nanoparticles. In our case, since only room light was used as the photoreduction source, the Au nanoparticles might be in a slightly positive overall the high oxidation states, or the disproportionation mechanism of El-Sayed may yield true Au(0) nanoparticles.

4.2.3 Size characterization with photon correlation spectroscopy

To further determine the sizes of luminescent particles in the solutions, the hydrodynamic radii of glutathione encapsulated luminescent gold nanoparticles were also characterized via photon correlation spectroscopy (Protein solutions Inc.). A small volume (0.5) of luminescent gold nanoparticle solution was placed in a three-sided quartz cuvette for determination of the hydrodynamic radii of the particles. The average hydrodynamic radii of glutathione encapsulated gold nanoparticles were observed 1.18 nm and 1.33 nm for red emitting and yellow emitting gold nanoparticles, respectively. The hydrodynamic radii of these gold nanoparticles are larger than sizes measured with TEM due to water layers forming around these nanoparticles. Photon correlation spectroscopic results further indicate that gold nanoparticles observed in TEM studies are not due to reduction by the electron beam of TEM and the relative sizes are consistent with TEM results. Combination of TEM and PCS measurement

results indicates that these gold nanoparticles are responsible for the observed emission, and that the yellow emitting nanoparticles are slightly large in size.

4.2.4 Photophysical properties of luminescent gold nanoparticles

Absorption spectra of the luminescent gold nanoparticles are distinct from those of fully reduced $\sim 2\text{nm}$ Au(0) gold nanoparticles which have weak but distinguishable plasmon absorption around 520 nm.^{2,26} As shown in Figure 4.2.4, the luminescent gold nanoparticles have no plasmon absorption but strong and broad absorption in the UV range. The UV absorptions likely arise from strong sulfur-gold charge transfer transitions.¹⁸ In these luminescent gold nanoparticles, “soft” sulfur atoms can be considered weak reducing agents, and donate electrons to Au ions by forming S-Au(I) bonds.^{8,27} Since the same size fully reduced gold nanoparticles can give surface plasmon absorption, the absence of a plasmon absorption in these luminescent gold nanoparticles suggests that some gold atoms in the luminescent gold nanoparticles might not be fully reduced, as a result, the free electron density in the gold nanoparticles may not be high enough to give rise to plasmon absorption.

Excitation and emission spectra of luminescent gold nanoparticles are shown in Figure 4.2.5. Strong emission was observed around 568 nm and 600 nm with both excitation maxima around 398 nm and 265 nm were observed from glutathione-encapsulated luminescent gold nanoparticles, respectively. The strong UV excitation profiles and long lifetime ($\sim 5\ \mu\text{s}$) (Figure 4.2.6) are reminiscent of the photophysical properties of small luminescent gold(I) complexes/clusters at low temperature,^{14-16,27} suggesting that emission might result from the analogous electronic transitions such

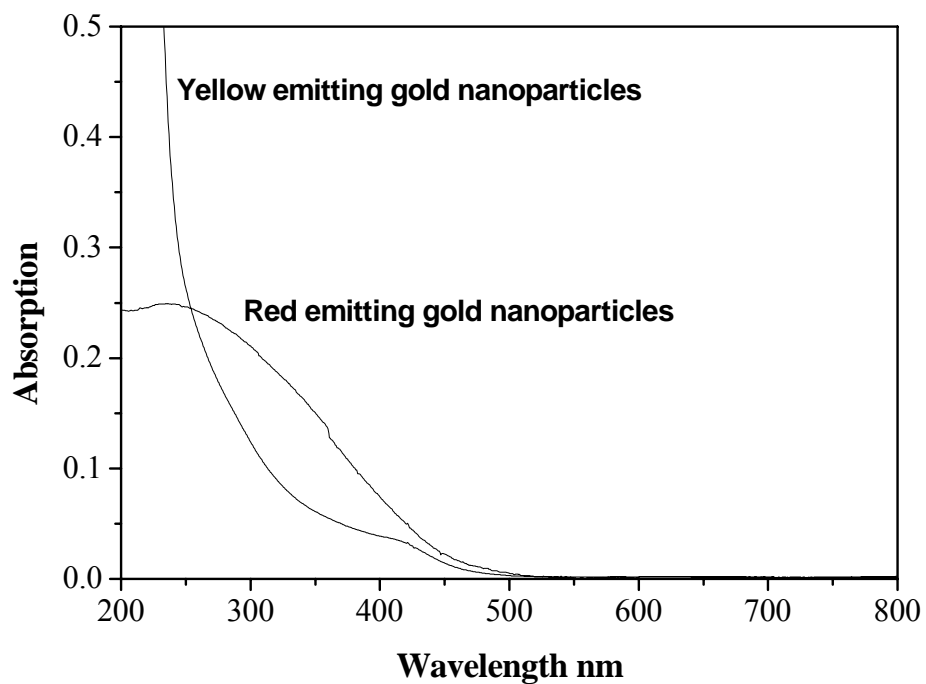


Figure 4-2-4 Absorption spectra of yellow and red emitting gold nanoparticles in aqueous solutions. Broad absorptions in the UV region may arise from ligand-metal charge transfer bands. No plasmon absorption are observed from these luminescent gold nanoparticles.

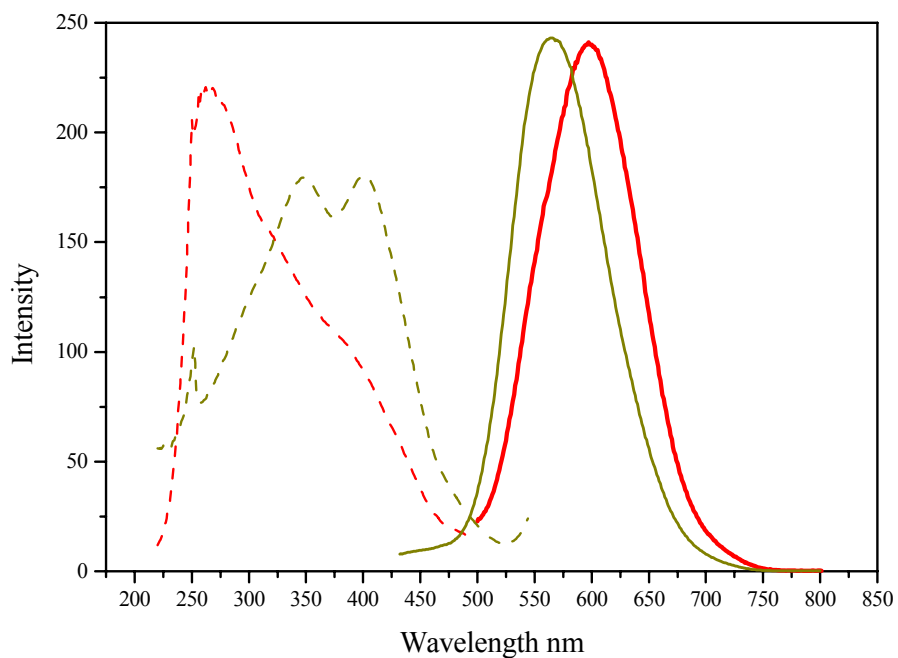


Figure 4-2-5 Excitation spectra (dash line) and emission spectra (solid line) of yellow (dark yellow color) and red (red color) luminescent gold nanoparticles. Strong emission was observed around 568 nm and 600 nm with both excitation maxima around 398 nm and 265 nm were observed from glutathione-encapsulated luminescent gold nanoparticles, respectively.

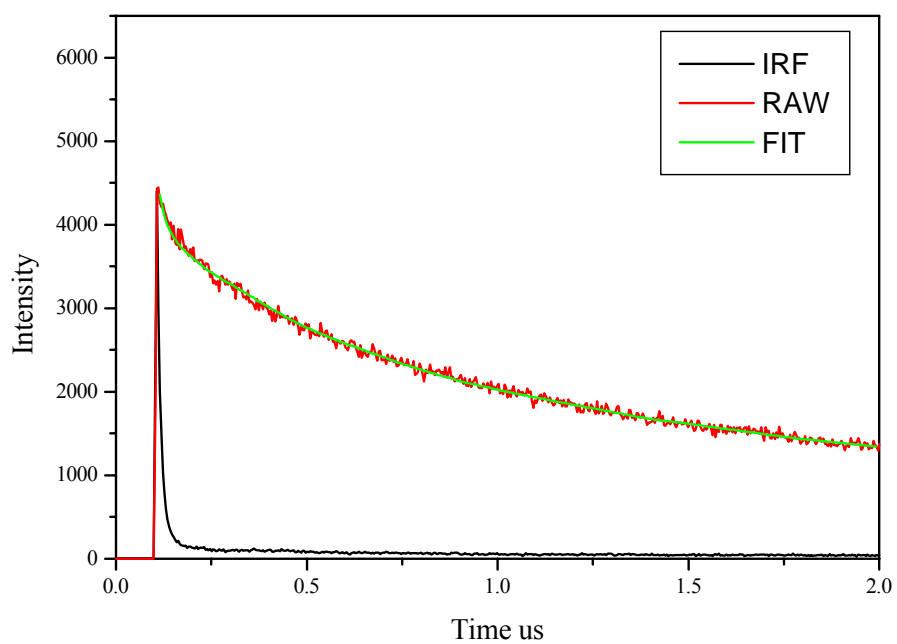


Figure 4-2-6. Lifetime measurement of red emitting gold nanoparticles. Lifetime of luminescent gold nanoparticles is around 5.04 μs .

as interband transitions (dp-sp) mixed with ligand to metal charge transfer.^{14,28-30} To investigate the overall oxidation states of gold in the luminescent gold nanoparticles, $4f_{7/2}$ and $4f_{5/2}$ binding energies of luminescent gold nanoparticles were investigated with XPS.

4.2.5 Average oxidation states of gold atoms in luminescent gold nanoparticles investigated by XPS studies

To further probe the detailed electronic structure of luminescent gold nanoparticles, oxidation states of the gold atoms in the particles were investigated using x-ray photoelectron spectroscopy (XPS). Luminescent films were prepared through drop casting the gold nanoparticle solutions on a silicon wafer. Binding energies (BE) of Au $4f_{7/2}$ electrons were used as a signature of Au oxidation states and were examined with alkyl chain C 1s BE (284.5 eV) as an internal reference. Figure 4.2.7 indicates that the gold Au $4f_{7/2}$ BE are 84.28 eV and 84.43 eV for yellow and red emitting gold nanoparticles respectively, which fall in the middle of Au(0) BE (84.0 eV) (~2 nm fully reduced Au(0) nanoparticles)^{26,31} and Au(1+) BE (84.9~85.3eV) (AuS complexes).^{32,33} These values suggest that both Au(1+) and Au(0) are constituents of the luminescent gold nanoparticles. Differences in the binding energies between yellow emitting and red emitting gold nanoparticles might arise from the size effect and also the relative ratio between Au(1+) and Au(0) in each luminescent nanoparticles. Ignoring any possible size effects and assuming a linear relation of binding energy with oxidation state, deconvolution of Au $4f_{7/2}$ binding energies indicates that 43% Au atoms in yellow emitting nanoparticles are Au(1+) while 52% Au(1+) in red emitting gold nanoparticles. Although XPS measurements

indeed suggests the existence of higher average oxidation state gold atoms in the luminescent nanoparticles, it is unclear whether emission energy is dependent on the abundance of Au(1+) in the nanoparticles.

4.2.6 Reducing luminescent gold nanoparticles

By slowly adding NaBH₄ into yellow/red luminescent solutions, absorption in the visible range slowly shows up and monotonically increases to higher energies and eventually weak but broad absorption around 520 nm was observed. (Figure 4.2.8). This broad visible absorption is the gold plasmon absorption and their sizes (Figure 4.2.9) and absorption are indistinguishable to the absorption spectra of fully reduced 2 nm gold nanoparticles reported by other groups.^{2,26} No luminescence was observed from these reduced glutathione encapsulated gold nanoparticles, suggesting that the Au(I) coordinated with ligands might be the emission centers for the observed luminescence. However, the detailed mechanism for the emission is still not clear, and specifically the particle size effecting the emission energy of the luminescent gold nanoparticles requires more study before giving any conclusive answers.

4.3 Conclusion

Luminescent gold nanoparticles encapsulated by glutathione molecules were synthesized and characterized with different techniques. Distinct from the similar size but nonluminescent gold nanoparticles, these 2 nm gold nanoparticles show bright and long lifetime emission but no plasmon. XPS measurements suggest the presence of higher average oxidation states gold atoms in the nanoparticles. The emission might arise from electronic transitions of gold(I) coupling to the ligand-metal charge

transfer transition. Although the detailed mechanism for emission has not been fully understood, these ~2 nm peptide encapsulated gold nanoparticles integrated with luminescence properties could be used as a new type of biological label with dual function for both optical and electron microscopy studies.

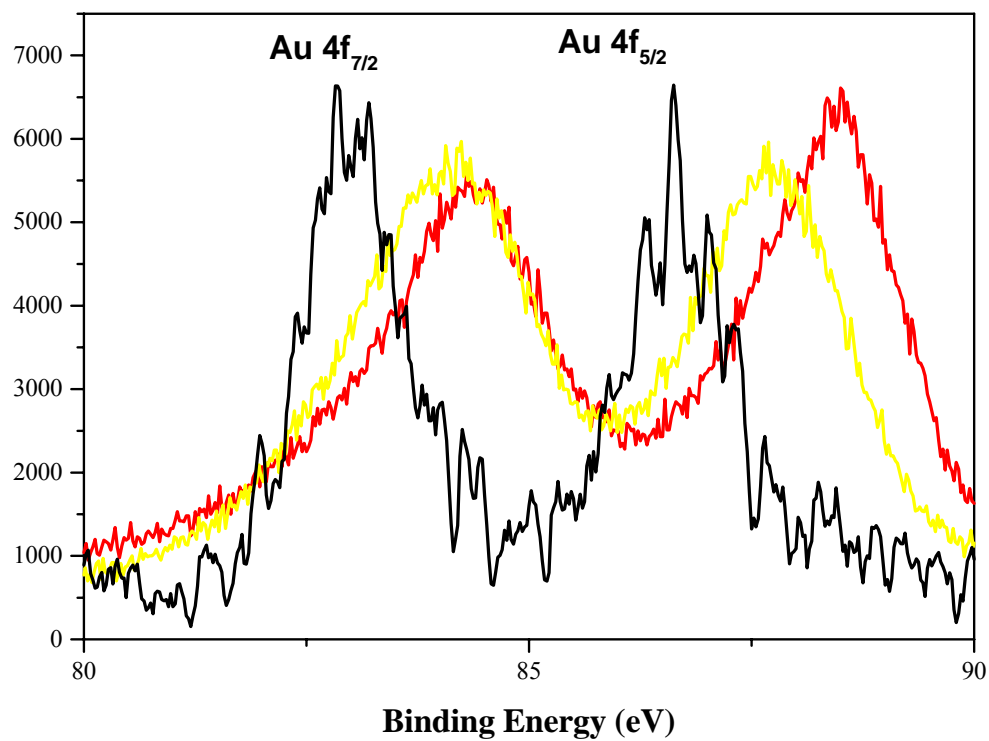


Figure 4-2-7. XPS spectra of Au 4f Binding energies of glutathione-encapsulated yellow (yellow curve) and red emitting (red curve) gold nanoparticles and that of fully reduced gold nanoparticles (black curve).

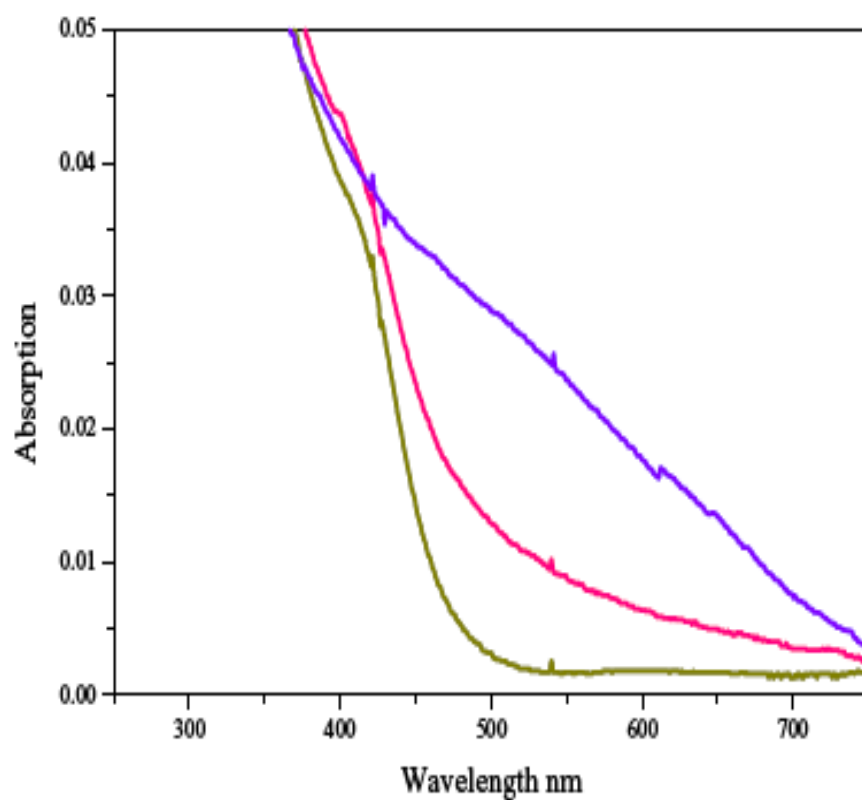


Figure 4-2-8 Absorption spectra of yellow emitting gold nanoparticles before and after adding NaBH_4 into the solution. Reducing yellow emitting gold nanoparticles leads to a weak and broad plasmon absorption at 520 nm.

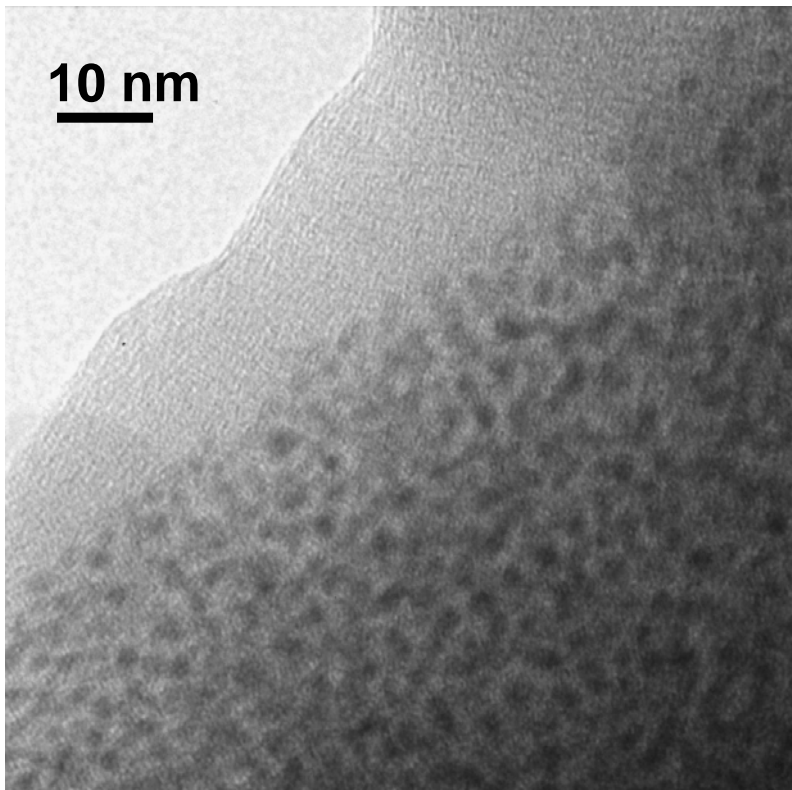


Figure 4-2-9 A TEM image of reduced yellow emitting gold nanoparticles, which shows the same size distribution of yellow emitting gold nanoparticles.

4.4 References

1. Elschenbroich, C. *Organometallics : a concise introduction* (New York, NY, USA : VCH,, 1992).
2. Kreibig, U. & Vollmer, M. *Optical Properties of Metal Clusters* (Springer, 1995).
3. Schaaff, T. G. *Preparation and characterization of thioaurite cluster compounds: Thesis* (School of Chemistry and Biochemistry, Georgia Institute of Technology,, 1999).
4. Zheng, J., Zhang, C. & Dickson, R. M. Highly Fluorescent, Water-Soluble, Size-Tunable Gold Quantum Dots. *Phys. Rev. Lett.* **93**, 077402 (2004).
5. Yam, V. W. W., Chan, C. L., Li, C. K. & Wong, K. M. C. Molecular design of luminescent dinuclear gold(I) thiolate complexes: from fundamentals to chemosensing. *Coord. Chem. Rev.* **216**, 173-194 (2001).
6. Fernandez, E. J., Laguna, A. & Lopez-de-Luzuriaga, J. M. Luminescence in gold-heterometal complexes. *Gold Bull.* **34**, 14-+ (2001).
7. Calhorda, M. J. et al. Synthesis, structure, luminescence, and theoretical studies of tetranuclear gold clusters with phosphinocarborane ligands. *Inorg. Chem.* **39**, 4280-4285 (2000).
8. Yam, V. W. W., Cheng, E. C. C. & Cheung, K. K. A novel high-nuclearity luminescent gold(I)-sulfide complex. *Angew. Chem.-Int. Edit.* **38**, 197-199 (1999).
9. Tzeng, B. C., Schier, A. & Schmidbaur, H. Crystal engineering of gold(I) thiolate based compounds via cooperative aurophilic and hydrogen-bonding interactions. *Inorg. Chem.* **38**, 3978-3984 (1999).

10. Yam, V. W. W., Cheng, E. C. C. & Zhou, Z. Y. A highly soluble luminescent decanuclear gold(I) complex with a propeller-shaped structure. *Angew. Chem.-Int. Edit.* **39**, 1683-+ (2000).
11. Hettiarachchi, S. R. et al. Spectroscopic studies of "exciplex tuning" for dicyanoaurate(I) ions doped in potassium chloride crystals. *J. Phys. Chem. B* **106**, 10058-10064 (2002).
12. Ford, P. C., Cariati, E. & Bourassa, J. Photoluminescence properties of multinuclear copper(I) compounds. *Chem. Rev.* **99**, 3625-3647 (1999).
13. Yam, V. W. W. & Lo, K. K. W. Luminescent tetranuclear copper(I) and silver(I) chalcogenides. *Comments Inorganic Chem.* **19**, 209-229 (1997).
14. White-Morris, R. L., Olmstead, M. M., Jiang, F. L., Tinti, D. S. & Balch, A. L. Remarkable variations in the luminescence of frozen solutions of $\text{Au}\{\text{C}(\text{NHMe})_2\}_2(\text{PF}_6) \cdot 0.5(\text{acetone})$. Structural and spectroscopic studies of the effects of anions and solvents on gold(I) carbene complexes. *J. Am. Chem. Soc.* **124**, 2327-2336 (2002).
15. Coker, N. L., Bauer, J. A. K. & Elder, R. C. Emission energy correlates with inverse of gold-gold distance for various $\text{Au}(\text{SCN})_2^-$ salts. *J. Am. Chem. Soc.* **126**, 12-13 (2004).
16. Assefa, Z. et al. Syntheses, Structures, and Spectroscopic Properties of Gold(I) Complexes of 1,3,5-Triaza-7-Phosphaadamantane (Tpa) - Correlation of the Supramolecular Au...Au Interaction and Photoluminescence for the Species $(\text{Tpa})\text{AuCl}$ and $(\text{Tpa-HCl})\text{AuCl}$. *Inorg. Chem.* **34**, 75-83 (1995).
17. Shan, H., Yang, Y., James, A. J. & Sharp, P. R. Dinitrogen bridged gold clusters. *Science* **275**, 1460-1462 (1997).
18. Pyykko, P. Strong closed-shell interactions in inorganic chemistry. *Chem. Rev.* **97**, 597-636 (1997).

19. Schaaff, T. G. et al. Isolation of smaller nanocrystal Au molecules: Robust quantum effects in optical spectra. *J. Phys. Chem. B* **101**, 7885-7891 (1997).
20. Schaaff, T. G., Knight, G., Shafiqullin, M. N., Borkman, R. F. & Whetten, R. L. Isolation and Selected Properties of a 10.4 kDa Gold:Glutathione Cluster Compound. *J. Phys. Chem. B* **102**, 10643-10646 (1998).
21. Schaaff, T. G. & Whetten, R. L. Controlled etching of Au : SR cluster compounds. *J. Phys. Chem. B* **103**, 9394-9396 (1999).
22. Schaaff, T. G. & Whetten, R. L. Giant gold-glutathione cluster compounds: Intense optical activity in metal-based transitions. *J. Phys. Chem. B* **104**, 2630-2641 (2000).
23. Schaaff, T. G., Shafiqullin, M. N., Khoury, J. T., Vezmar, I. & Whetten, R. L. Properties of a ubiquitous 29 kDa Au : SR cluster compound. *J. Phys. Chem. B* **105**, 8785-8796 (2001).
24. Brust, M., Walker, M., Bethell, D., Schiffrin, D. J. & Whyman, R. Synthesis of Thiol-Derivatized Gold Nanoparticles in a 2-Phase Liquid-Liquid System. *Journal of the Chemical Society-Chemical Communications*, 801-802 (1994).
25. Eustis S., H. H. Y., El-Sayed MA. Gold Nanoparticle Formation from Photochemical Reduction of Au³⁺ by Continuous Excitation in Colloidal Solutions. A Proposed Molecular Mechanism. *J. Phys. Chem. B* **109** (2005).
26. Hostetler, M. J. et al. Alkanethiolate gold cluster molecules with core diameters from 1.5 to 5.2 nm: Core and monolayer properties as a function of core size. *Langmuir* **14**, 17-30 (1998).
27. Lee, Y. A. & Eisenberg, R. Luminescence tribochromism and bright emission in gold(I) thiouracilate complexes. *J. Am. Chem. Soc.* **125**, 7778-7779 (2003).

28. Lee, Y. A., McGarrah, J. E., Lachicotte, R. J. & Eisenberg, R. Multiple emissions and brilliant white luminescence from gold(I) O,O'-di(alkyl)dithiophosphate dimers. *J. Am. Chem. Soc.* **124**, 10662-10663 (2002).
29. Yam, V. W. W. & Cheng, E. C. C. Molecular gold - Multinuclear gold(I) complexes. *Angew. Chem.-Int. Edit.* **39**, 4240-+ (2000).
30. Link, S. et al. Visible to infrared luminescence from a 28-atom gold cluster. *J. Phys. Chem. B* **106**, 3410-3415 (2002).
31. Bourg, M. C., Badia, A. & Lennox, R. B. Gold-sulfur bonding in 2D and 3D self-assembled monolayers: XPS characterization. *J. Phys. Chem. B* **104**, 6562-6567 (2000).
32. McNeillie, A., Brown, D. H., Smith, W. E., Gibson, M. & Watson, L. X-Ray Photoelectron-Spectra of Some Gold Compounds. *J. Chem. Soc.-Dalton Trans.*, 767-770 (1980).
33. Scaini, M. J., Bancroft, G. M. & Knipe, S. W. Reactions of aqueous Au¹⁺ sulfide species with pyrite as a function of pH and temperature. *American Mineralogist*, **88**, 316-322 (1998).

CHAPTER 5

Fluorescent silver clusters and their Raman enhancement

5.1 Introduction

Single molecule fluorescence microscopies^{1,2} are very powerful tools to unravel many mysteries underlying the heterogeneous dynamics characteristic of nanoscale materials and biosystems.^{3,4} Although many fluorophores can be utilized in single molecule microscopy, only semiconductor nanocrystals^{5,6} have sufficiently strong absorptions to be easily observed at the single molecule level with weak mercury lamp excitation. Such materials can potentially enable facile, inexpensive single molecule studies, but syntheses require toxic compounds and high temperature methods.

Similar to gold metal, silver metal also has very wide size-dependent optical properties and displays discrete electronic transitions on the few-atom size scale. In 1978, Ozin and Huber used cryophotoclustering techniques to prepare a series of small naked silver clusters Ag_n (where $n < 6$) at low temperature and attempted to bridge the molecular cluster-bulk microcrystalline metal interface by investigating the correlation of absorption with cluster size.⁷ A remarkable monomeric relationship between the lowest absorption energy and the number of atoms N of Ag_N (where N

<6) was discovered. Although this correlation was not fully understood at that time, it actually can be easily rationalized with the electronic shell/jellium model proposed by Knight et al in 1984.⁸ Since the small silver clusters Ag_N (where $2 \leq N \leq 5$) were predicted to have linear chain structure in the gas phase as calculated by Baetzold,⁹⁻¹² the energy level spacing could be linearly dependent on $1/R$ (where $R=r_s N$ for linear silver chain structures) based on the free electron gas model. As a result, similar to fluorescent gold clusters, small silver clusters could also be considered as free electron “artificial atoms”.

Not only discrete absorptions but also fluorescence was observed from small silver clusters. One of the early works performed by Harbich and coworkers was the observation of fluorescence from Ag_2 and Ag_3 at low temperature in rare gas matrices.^{13,14} Silver dimer in an Ar matrix not only showed discrete absorption transitions at 243, 262, 382, and 441 nm similar to those reported by Ozin et al.,⁷ but also gave emission at 288 and 479 nm. Silver trimer in an Ar matrix also had discrete emission at 374, 616 and 705 nm.^{13,14} In addition, silver tetramer gave emission at 458 nm,¹⁵ while Ag_8 gave emission at 394 nm reported by Rabin et al..¹⁶

In 1998, Chen et al found that zeolite-Y can encapsulate and stabilize fluorescent silver clusters in the condensed phase.^{17,18} Silver ions were first adsorbed into the small cavities of zeolites and then photoreduced with UV light to form silver clusters. Strong emission from 460-600 nm was observed. In 2001, a simpler method to generate fluorescent silver clusters at room temperature was discovered by our group.¹⁹ Small fluorescent silver nanoclusters (Ag_2 - Ag_8) are readily created by

photoreducing silver oxides films at room temperature. In addition, these silver clusters yield such strong multicolored fluorescence that the emission can be easily observed at the single molecule level even under the very weak mercury lamp excitation.^{19,20} While potentially useful as optical data storage elements, very little control could be effected over individual surface-bound clusters as continued irradiation of silver oxides further modifies nanocluster size and therefore emission color.¹⁹⁻²¹ Consequently, studying individual species proved very difficult. Additionally, the surface-bound nature of these highly fluorescent species precluded the applications as fluorescent labels or as volumetric optical data storage elements.²¹ Thus, synthesis of stable, water-soluble individual silver clusters will greatly facilitate the characterization and use of these photoactivated nanomaterials at the single molecule level.

Interaction of light with silver metal on the nanoscale is strongly size-dependent. Different from small fluorescent silver clusters, large 40-100 nm silver nanoparticles are nonfluorescent, but show strong surface plasmon scattering and surface enhanced Raman scattering (SERS).²²⁻²⁷ Although typical Raman scattering cross sections are very small ($\sim 10^{-30}$ cm²/molecule), Raman signal can be greatly enhanced by coupling with large metal nanoparticles. In 1974, Fleischmann and coworkers first observed six orders of magnitude enhanced Raman signals from pyridine adsorbed on a rough surface of a silver electrode.²⁸ Later, as large as 10^9 Raman enhancements were observed from molecules absorbed on 50-100 nm silver nanoparticles.²⁹⁻³² This large Raman enhancement is called surface-enhanced Raman

scattering (SERS), mainly arising from the strong surface plasmon enhancement effect and chemical effects.^{23,33-36} Coherent oscillation of free electrons in metal nanoparticles under light excitation can greatly increase the strength of local electrical field close to the particles, leading to $\sim 10^6$ fold enhancement in Raman scattering cross sections of molecules adsorbed or in close proximity to the surface. The chemical effect is mainly thought to arise from charge transfer between analytes and the metal surface, resulting in $\sim 10^3$ -fold enhancement in Raman scattering cross section^{33,36-41} Fundamentally, this charge transfer mechanism is similar to resonance Raman scattering enhancement as it is thought to create new electronic levels close to the laser excitation frequency, strongly coupling the molecular orbitals of analytes with the conduction bands of the nanoparticles.

Although considerable progress has been made in understanding the enhancement mechanisms, the SERS effect was found to be much more complicated at the single molecule level. To unravel the details in single molecule Raman enhancement, Kneipp et al. in 1997 used a cw 830 nm laser to excite a crystal violet molecule adsorbed on 100 nm silver nanoparticles and directly observed the single molecule crystal violet Raman spectra with extremely large cross sections ($10^{-16} \sim 10^{-15}$ cm²/molecule).⁴² In addition, Raman scattering intensity was also found to fluctuate with time.⁴² Nie and Emory⁴³ used cw 514 nm laser to excite single R6G molecules on silver nanoparticles and also observed enormous SERS enhancements on the order of $10^{14} \sim 10^{15}$, which is consistent with the enhancement factor reported by Kneipp et al.⁴² These studies reveal that the enhancement factor achieved from the single

molecule studies is much larger (10^6 –fold) than that obtained from the bulk studies. Through imaging, they also discovered that only a very small subset of silver nanoparticles can give such large enhancement even though all particles are of similar size. These magic SERS active silver nanoparticles are called “hot” nanoparticles.⁴³ By exploiting the plasmon-enhanced electromagnetic fields and resonance effects, these incredible enhancements were attributed to rare surface interactions present on the “hot” nanoparticles or “hot spots”. To increase hot spot concentrations, NaCl can be added into silver nanoparticle solution to induce aggregation,^{42,43} however, detailed information about these hot spots is still missing.

A mystery arising from single molecule SERS studies is the discrepancy in the enhancement factor between calculations and those obtained in the single molecule studies.⁴⁴ Based on these two classical enhancement mechanisms, the overall calculated SERS enhancement at the single molecule level should range from 10^9 to 10^{11} , which is about 10^4 to 10^6 fold smaller than the necessary to explain the experimental results obtained at the single molecule.⁴⁴ The great disparity between observed and calculated enhancements indicates that either the plasmon enhancement or the chemical effect is underestimated. Recently Brus et al. found that such large enhancements might arise from the greatly enhanced local electric fields in junctions between nanoparticle,⁴⁴ where the field strength is more than 10^3 larger than that in other locations due to the couplings of two plasmon enhanced electric fields. This large electric field may comprise the missing 10^6 enhancement in SM-SERS. However, since strong SERS signals were also observed from single large silver

nanoparticles without junctions,⁴³ detailed SERS mechanisms require more research. More interestingly, although all of these well-known SERS-active nanoparticles with sizes 40-100 nm are nonfluorescent, a strong broad emission background always comes along with SERS signals even from nonfluorescent organic scaffolds or analytes.⁴³ This emission potentially can be used as an alternative optical signature to shed light on the local electronic structures of “hot” spots. We and other groups have demonstrated that small few atom Ag nanoclusters are strongly fluorescent with large oscillator strengths.^{13,17,19,21} In this chapter, water-soluble fluorescent silver clusters were synthesized and their fluorescence, Stokes and antistokes Raman scattering were investigated at the single molecule level.

5.2 Results and Discussion

5.2.1 Growth of fluorescent silver clusters with photoactivation

Initially, no visible fluorescence is observed from dendrimer encapsulated silver ion solutions under blue light excitation, but, more and more multicolored emissive species were observed with increased photoactivation. Within ~6 s, the field of view is filled with individual blinking fluorescent species, with little subsequent photoactivation (Fig. 5.2.1A). These very bright, stable fluorescent features are all highly polarized and exhibit well-defined dipole emission patterns⁴⁵ (Fig. 5.2.1B). Since transition dipoles have different angles relative to the field of view, both out of plane (“donut” shape) and in plane (“butterfly” shape) emission dipoles are easily observed even with very weak mercury lamp excitation (30 W/cm²). Correlated with the absorption changes, fluorescence quickly grows in with increasing irradiation

time as silver ions are photoreduced inside the dendrimer host and blinking dynamics characteristic of individual emitters are observed. After completion of photoactivation, the fluorescent silver – dendrimer nanodots remain very stable both in average emission intensity and in spectral characteristics. The dendrimer thereby stabilizes the nanoclusters and enhances their optical properties relative to those on AgO films.^{19,20} Necessary because the binding energy of small Ag nanoclusters is less than the excitation energy, the cage effect of the dendrimer likely acts similarly to that of rare gas matrices⁴⁶ to stabilize and enhance the nanocluster fluorescence by preventing photodissociation. While water has been shown to quench Ag nanocluster fluorescence on AgO films,⁴⁷ silver nanoclusters encapsulated in dendrimers are highly fluorescent and quite stable in water solution. Thus, the photochemically produced Ag nanoclusters are also protected inside the dendrimer, thereby preventing interaction with quenchers in solution.

5.2.2 Comparison of fluorescent silver nanoclusters and nonfluorescent silver nanoparticles

Although difficult to measure the exact size of the fluorescent nanodots, similarly prepared solutions of larger silver nanoparticles (1.5-7 nm) utilizing NaBH₄ reduction⁴⁸⁻⁵¹ yield a characteristic, strong surface plasmon absorption at 398 nm, but with essentially no fluorescence (Fig. 5.2.2). The absorption spectrum of the nanoparticle solution is shown in Figure 5.2.2C (Curve 1). The position of the plasmon absorption peak around 400 nm suggests that the nanoparticles are

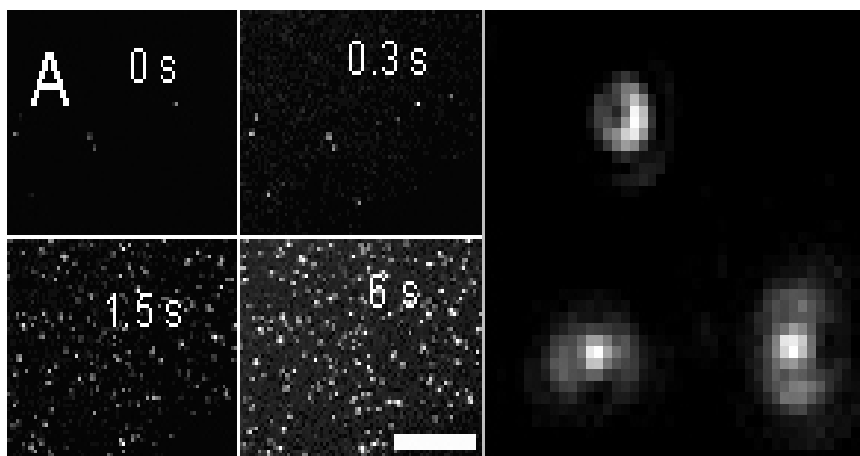


Figure 5-2-1 Time-dependent photoactivation of aqueous dendrimer-encapsulated silver nanoclusters and single silver nanocluster emission patterns on the surface. A Mercury lamp excited (450 to 480 nm, $30\text{W}/\text{cm}^2$, scale bar = $15\ \mu\text{m}$) epifluorescence microscopy images demonstrating time-dependent photoactivation of aqueous dendrimer-encapsulated silver nanodots. Each 300 ms CCD frame shows increasing fluorescence with illumination time. (B) Surface-bound silver nanodot emission patterns in aqueous solutions. Indicative of single molecules, the anisotropic emission patterns and fluorescence blinking are easily observable under weak Hg lamp excitation.

widely dispersed; TEM characterization of silver nanoparticles from the solution indicates that the particles are isolated and monodisperse with size around 2 to 6 nm. The mean particle radius was determined to be 3.6 nm. Since the radius of an individual G4 PAMAM dendrimer has been estimated on the basis of molecular modeling calculations to be approximately 2.3 nm and has been measured in methanol solution by small-angle X-ray scattering to be approximately 1.7-1.9 nm, these large nanoparticles actually were encapsulated by several dendrimer molecules.⁵⁰

A drop of the nanoparticle solution was also studied with optical microscopy under the same conditions as for small fluorescent silver clusters. No emission was observed from these large nanoparticles, indicating that the emissive silver clusters must be smaller than 2 nm. Additionally, photoactivation is clearly demonstrated by the solution absorption spectra (Figure 5.2.2C) before and after exposure to white light. Initially only the dendrimer contributes to the spectrum with a single absorption at 284 nm. After photoactivation, instead of a surface plasmon, the solution exhibits two new peaks (345 nm and 440 nm) due to the absorption of small, photoreduced silver nanodots.^{46,52} The size and geometry differences of the small silver nanodots simultaneously created during photoactivation yield multicolored fluorescence throughout the visible region (Fig. 5.2.2D).

5.2.3 Size characterization of fluorescent silver clusters with ESI Mass spectrometry

The well-defined dendrimer structure enables analysis of encapsulated silver nanocluster sizes with electrospray ionization (ESI) mass spectrometry. As shown in

Figure 5.2.3, silver dimer, trimer, and tetramer were all observed in the solution although the concentrations of these species were very low. Limited by the low concentration of fluorescent silver clusters, correlation of emission with size is still unsolved. Creating fluorescent silver clusters at high concentration is key to unraveling this correlation.

5.2.4 Fluorescence spectra of dendrimer encapsulated silver nanoclusters

While the bulk spectra of Ag_n of our aqueous nanodot solutions (Fig. 5.2.4A, top) are indistinguishable, five stable and easily distinguished fluorescence spectra are obtained from these highly dispersed dendrimer-encapsulated silver nanodots (Fig. 5.2.4A bottom), suggesting that the bulk spectrum is dominated by as few as five nanocluster sizes. Considerably narrower than those of bulk nanodot films or solutions, room temperature single nanodot fluorescence spectra exhibit no obvious spectral diffusion. Because no additional silver can be incorporated into the nanodot and the dendrimer stabilizes the nanodot fluorescence, single nanodot emission is quite stable and robust with maxima at 533 nm, 553nm, 589nm, 611nm and 648nm, although fluorescence intermittency is readily observed. Comparable to II-IV nanoparticles, these nanodots are very photostable with ~80% of individual features remaining fluorescent for >30 minutes of continuous 514.5-nm or 476 nm excitation at $300\text{W}/\text{cm}^2$ (Figure 5.2.4B). The nanodot photoactivation, blinking, dipole emission patterns, spectral stability, and fluorescence only at small size, further indicate that individual dendrimer-encapsulated Ag_n nanoclusters less than 8 atoms in

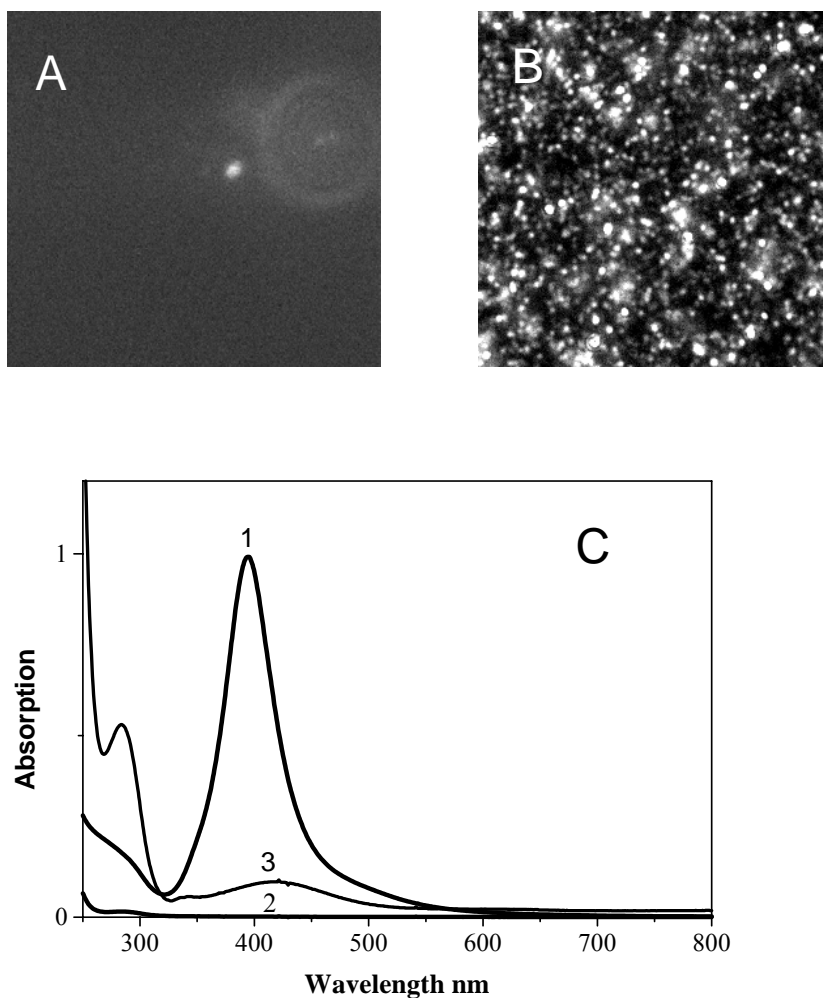


Figure 5-2-2 Comparison of fluorescence images and absorption spectra of dendrimer encapsulated fluorescent silver clusters and nonfluorescent silver nanoparticles. Emission images of silver nanoparticles (A) and silver clusters (B) under blue light (460~490 nm) excitation. (C) UV-Vis spectra of aqueous Ag/dendrimer solutions. (1) Strong plasmon absorption (398 nm) characteristic of large, nonfluorescent dendrimer-encapsulated silver nanoparticles prepared through NaBH_4 reduction of silver ions in the dendrimer host (1:12 dendrimer:Ag). (2) Absorption spectrum of nonfluorescent 1:3 (dendrimer:Ag) solution before photoactivation, and (3) the same solution after photoactivation to yield highly fluorescent silver nanodots.

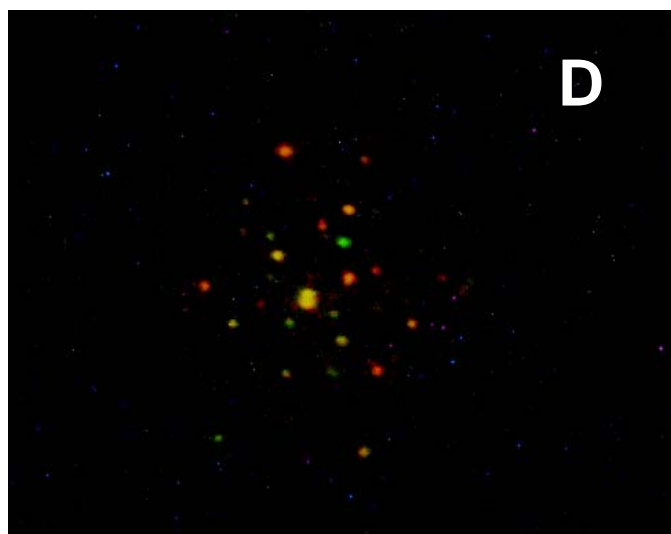


Figure 5-2-2 (D) A 476 nm laser excited epifluorescence microscope image demonstrates multicolor emission from dendrimer encapsulated silver clusters solution. (250X, 1-s exposure on Kodak DCS620X color digital camera, 476-nm excitation with 300 W/cm^2).

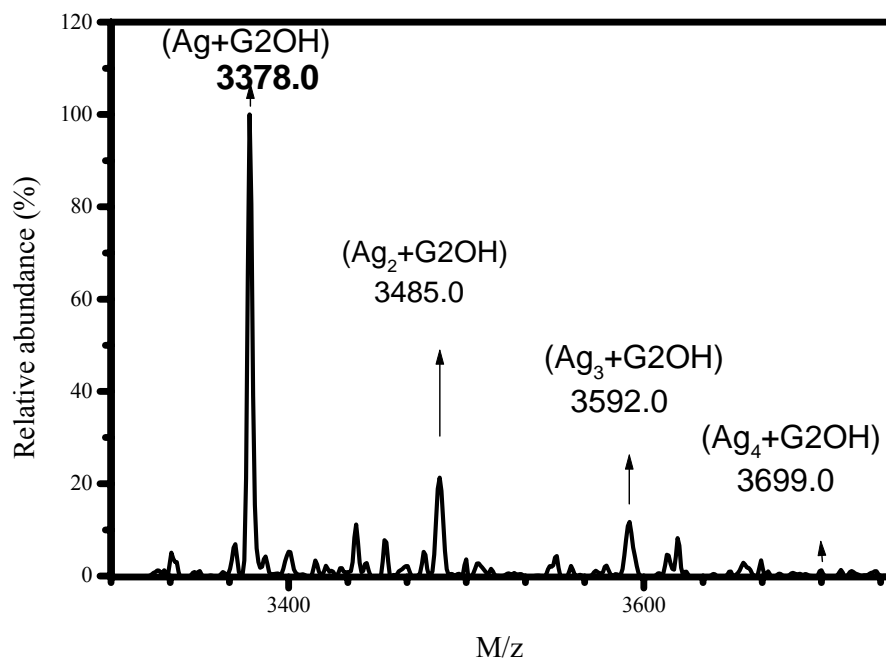


Figure 5-2-3 Electrospray ionization mass spectrum of photoactivated G2-OH PAMAM (MW: 3272 amu) – AgNO₃ solution. Ag_n nanodot peaks are spaced by the Ag atomic mass (107.8 amu) and only appear in the fluorescent, photoactivated nanodot solutions

size give rise to the observed emission. Crucial to solubility and stabilization, the dendrimer enhouses and protects the nanoclusters, yielding strong emission and providing a silver-limited environment that prevents further photoreduction/nanocluster growth, especially after the sample has dried.

5.2.5 Excitation spectra of fluorescent silver clusters

Since emission of silver clusters is very strong at the single molecule level even under very weak excitation, excitation spectra of dendrimer encapsulated fluorescent silver clusters can be easily collected. Detailed measurement procedures have been described in chapter 2. Excitation spectra of dendrimer/peptide encapsulated silver clusters are in the range from 400 nm to 520 nm with maximum emission when at 475 nm (shown in Figure 5.2.5A). Detailed studies indicate that the maximum excitation wavelength for green emitting (533 nm) silver clusters is around 444 nm (Figure 5.2.5B), which is suggestive of the excitation wavelength of silver dimer in the gas phase.¹³ This similarity may suggest that green emitting silver cluster may be silver dimer, but no conclusive assignments of silver cluster size can currently be made. Red emitting silver clusters show maximum excitation at 460 nm (Figure 5.2.5C). However, due to equipment limitation, it is difficult to accurately correlate the excitation spectra with the emission colors.

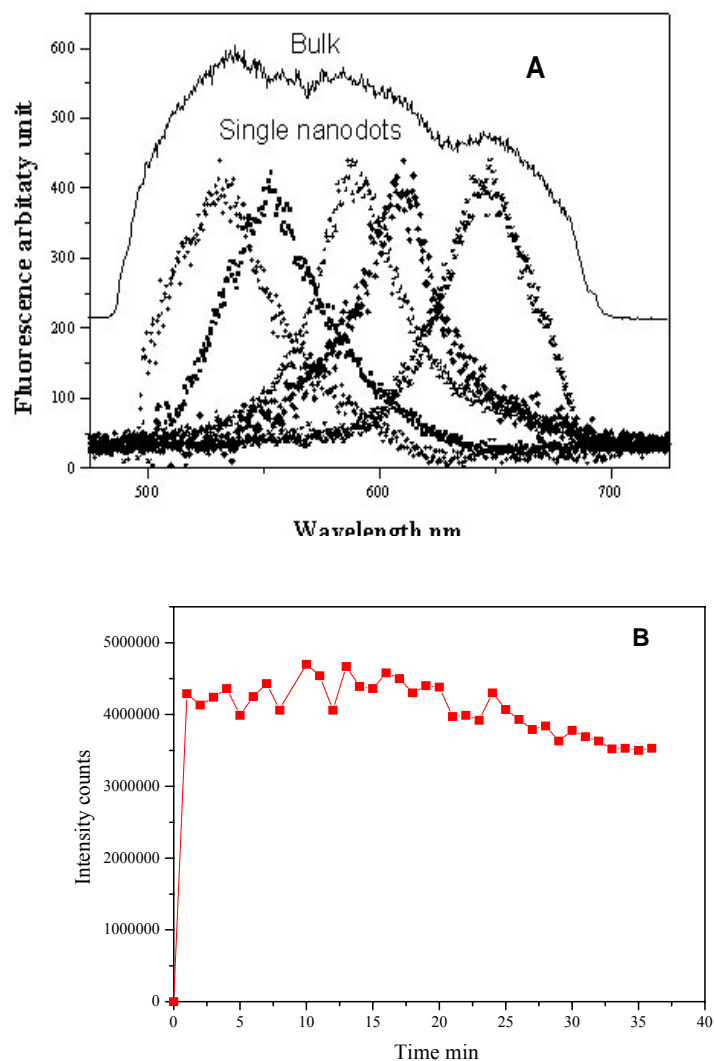


Figure 5-2-4 . Room temperature single cluster fluorescence spectra and their photostability. (A) Taken in a confocal geometry (476-nm Ar^+ laser excitation, 496-nm long-pass emission filter and dispersed by a 300-mm path length monochromator), emission maxima for the five typical nanodots shown are 533 nm, 553 nm, 589 nm, 611 nm, and 648 nm, and the ensemble fluorescence spectrum of bulk silver cluster solutions (top) is primarily composed of these five spectral types. (B) Photostability measurement of bulk dendrimer encapsulated fluorescent silver clusters on a coverslip under the excitation of 476 nm laser with a total internal reflection (TIR) geometry. Collection time for each point is 0.5 s.

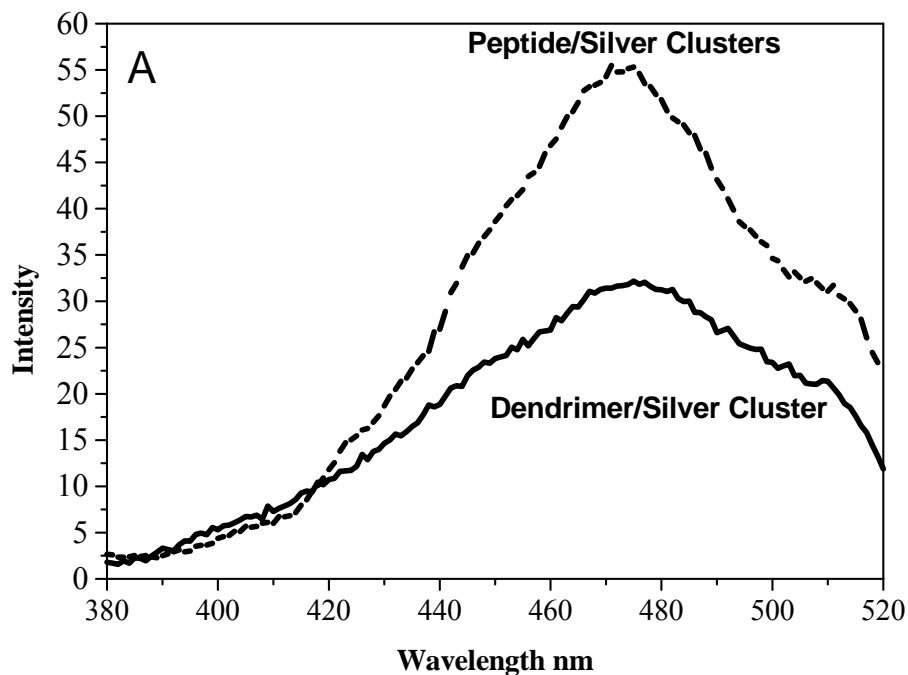


Figure 5-2-5. Excitation spectra of fluorescent silver clusters. (A) Room temperature bulk excitation spectra from different individual silver nanodots. Taken in a epifluorescence geometry (scanning excitation light from 360~520 nm, 520 nm short-pass excitation filter in the excitation path and 540 nm LP emission in the emission path) Integration time for each step is 1 s. Bulk excitation maxima for both dendrimer and peptide is around 475 nm. (B) Single molecule excitation spectrum for green emitting silver cluster with maximum at 440 nm. (C) Single molecule excitation spectrum for red emitting silver cluster with the excitation maximum at 460 nm.

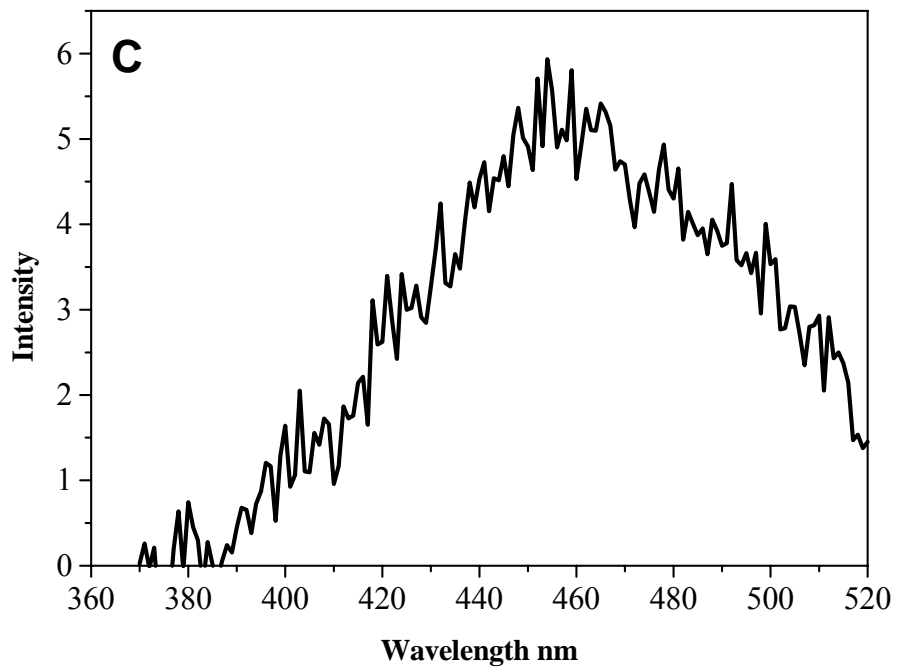
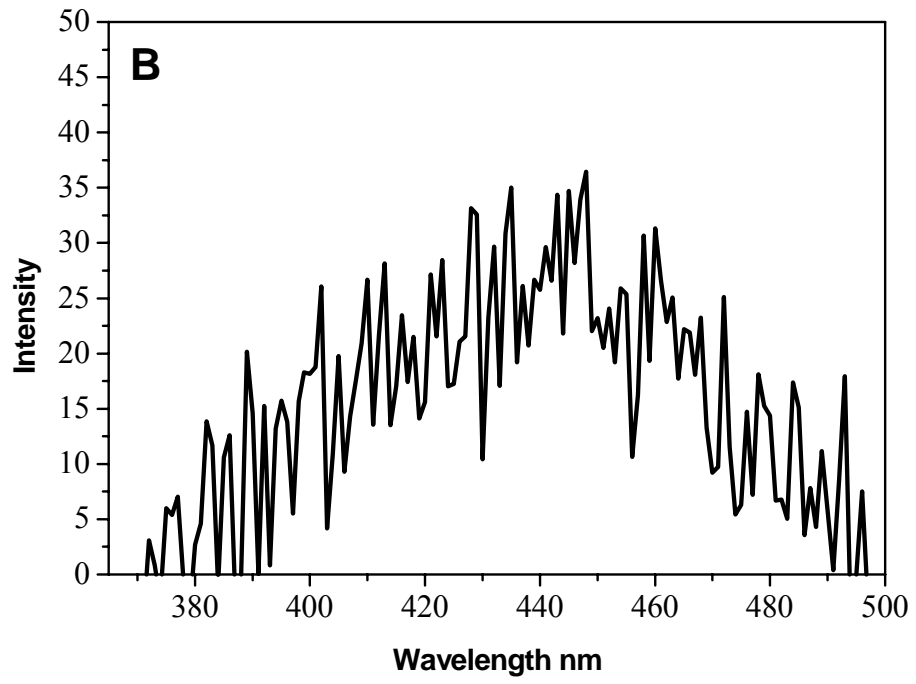


Figure 5-2-5 cont.

5.2.6 Creating red emitting silver clusters with HeNe laser photoactivation

Fluorescence spectra of silver clusters are strongly dependent on their size and geometry, as a result, silver clusters created through blue and green excitation of bulk solutions have very broad emission spectra. These broad bulk spectra, however, limit their practical applications as biological labels or as active media in optoelectronics. Toward accurately controlling the cluster size at the atomic level and its emission, we recently discovered a very simple method to generate greater spectrally pure red emitting silver clusters, which have much narrower bulk emission spectra than the clusters prepared through photoactivation with blue and green light. Instead of using blue or green photoactivation, we used the 633nm line of a HeNe laser with intensity around 500 W/cm^2 to photoactivate the solution containing dendrimer or peptide/silver ions, and within tens of seconds, red emitting silver clusters were formed in the solutions.(Figure 5.2.6A) These red emitting silver clusters have 50-60nm FWHM in the bulk state, which is much narrower than 150 nm FWHM of silver clusters obtained with green or blue light photoactivation. (Figure 5.2.6B) Although the mechanism for forming red emitting silver clusters is still not clear, a possible scheme might be similar to the one proposed by Ozin in his cryophotoclustering techniques.⁵³ Light can induce aggregation of excited silver atoms and different frequency light might induce or limit the different aggregation pathways.

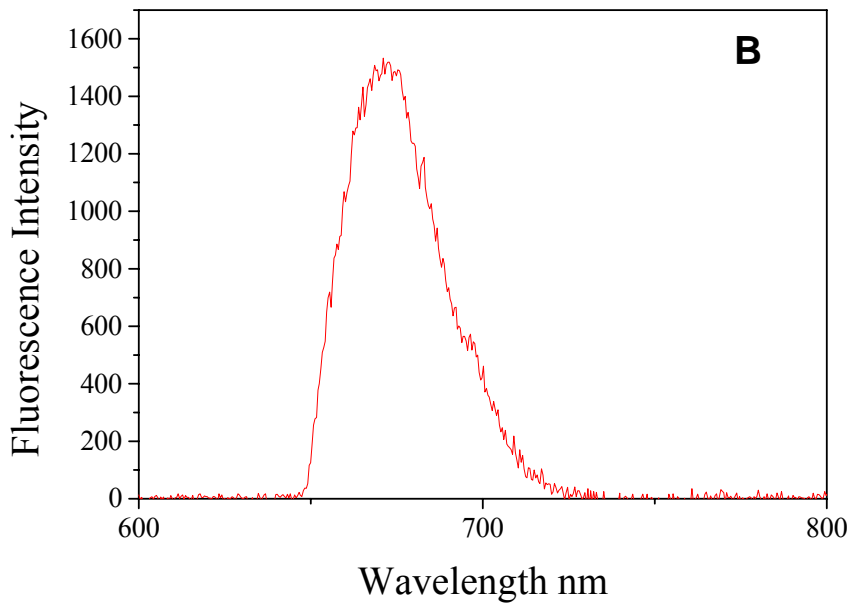


Figure 2-5-6 Fluorescence image (A) and a bulk fluorescence spectrum (B) of the peptide encapsulated red emitting silver nanoclusters. The image was collected with 250X, 1-s exposure on Kodak DCS620X color digital camera, under 633-nm excitation. The room temperature bulk fluorescence spectrum was taken in a confocal geometry (633-nm HeNe laser excitation, 633 NB laser excitation filter, 650-nm long-pass emission filter and dispersed by a 300-mm path length monochromator).

5.2.7 Raman enhancement by fluorescent silver clusters

Although these silver clusters are too small to have surface plasmon absorptions, strong Raman enhancement was discovered while studying emission spectra of dendrimer encapsulated fluorescent silver clusters. Surprisingly, in addition to fluorescence, Raman scattering was observed from both dendrimer and peptide encapsulated silver clusters under CW laser excitation at the single molecule level. Figure 5.2.7 shows Raman and fluorescence of three individual silver clusters obtained with 476 nm excitation. Often considered evidence of single molecule behavior, emission intermittency in both the fluorescence and Raman is readily observed.^{42,43} Although these clusters are encapsulated by the same dendrimer scaffolds, different emitting silver clusters enhanced the different vibrations of dendrimers. Adding these Raman spectra of individual silver clusters together are consistent with the bulk spectra, further indicating that fluorescent silver clusters are involved in such large Raman enhancements.⁵⁴ The Raman spectra are strongly dependent on scaffolds used to encapsulate these fluorescent silver clusters. Obvious differences in Raman spectra of dendrimer and peptides encapsulated silver clusters were observed after integrating more than one hundred of silver cluster enhanced Raman spectra.⁵⁴

5.2.8 Stokes Raman spectra of single dendrimer encapsulated fluorescent silver clusters

By controlling the concentration of fluorescent silver clusters in the field of the view, Raman scattering from both dendrimer and peptide encapsulated red

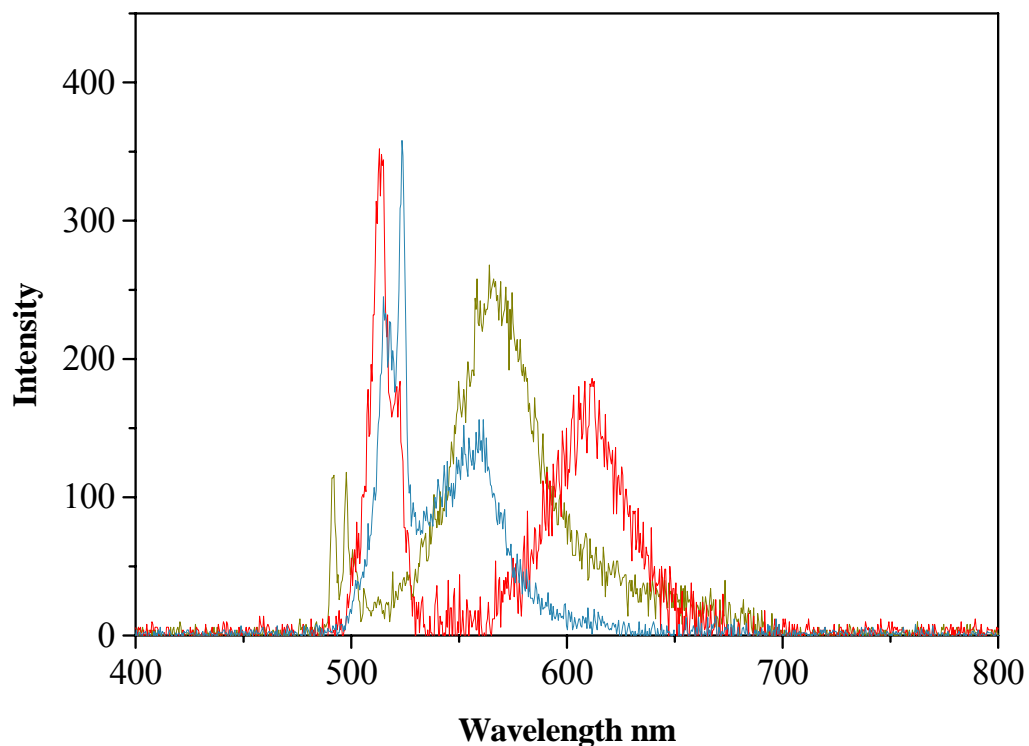


Figure 5-2-7. Room temperature fluorescence and Raman spectra from different individual dendrimer encapsulated fluorescent silver nanoclusters. Taken in a confocal geometry (476-nm Ar^+ laser excitation, 496-nm long-pass emission filter and dispersed by a 300-mm path length monochromator), Fluorescence maxima for the three typical nanodots shown are 553 nm, 570 nm, 611 nm. Raman peaks corresponding vibration energies are shifted by 642, 928, 1552 and 1888 cm^{-1} .

emitting silver clusters can be readily observed (Figure 5.2.8). Strong coupling with electronic absorption of silver clusters during laser excitation might lead to a type of resonance or pre-resonance enhancement.⁵⁴ However, the fundamental physics behind this unusually large enhancement is still not clear. Several possible processes might contribute to this large enhancement due to some unique interactions of silver clusters with light. The first plausible process is highly efficient charge/electron transfer between small silver clusters and organic scaffolds. Henglein and coworkers⁵⁵ investigated the chemical reactivity of silver aggregates over a wide size range and found that small silver clusters have much higher chemical reactivity than the large nanoparticles. As a result, charge/electron transfer becomes more efficient between organic molecules and small silver clusters than with their large nanoparticle counterparts.⁵⁵ The second process is photoemission electron⁵⁵. Photoelectron emission from compact silver electrodes occurs with extremely small quantum yield (<0.0001), however this yield greatly increases with decreasing size and the photoemitted electron quantum yield of few atom silver clusters is more than 10% .⁵⁵ This dramatic change in the quantum yield is because the small clusters have lower density of states in the conduction band, and photoejected electron can more easily tunnel to the acceptor levels of scaffolds. Such photoinduced electron transfer might also contribute to the Raman enhancement effect that we observed from these small fluorescent silver clusters. The third process is pre photodissociation of small silver clusters within organic scaffolds. Naked silver clusters are easily dissociated under

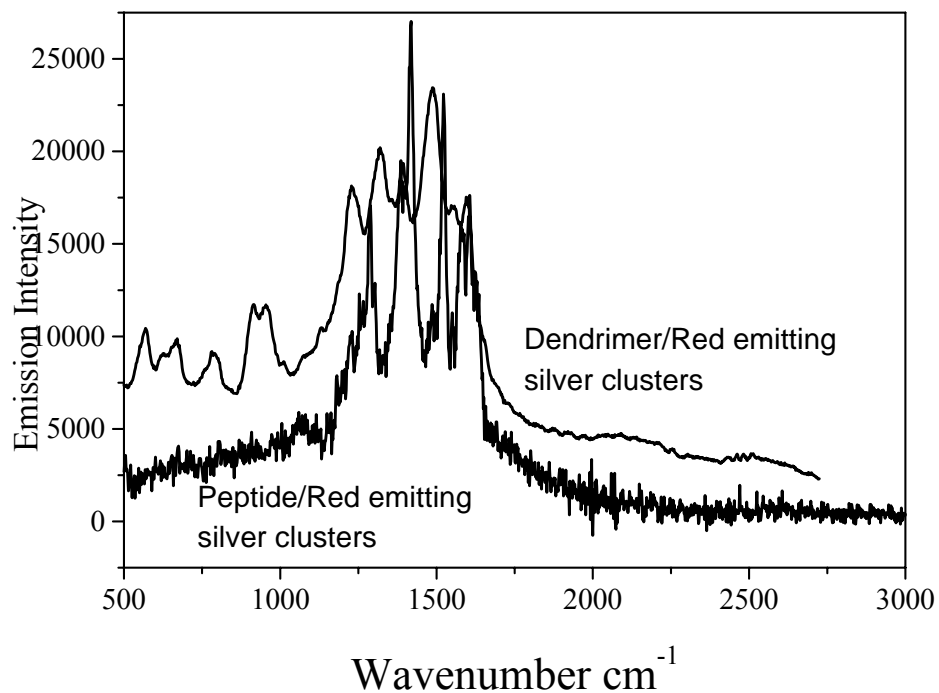


Figure 5-2-8 Room temperature bulk Raman spectra from dendrimer/peptide encapsulated red emitting silver clusters. Taken in a confocal geometry (633-nm HeNe laser excitation, a 633 NB laser excitation filter in the excitation path, a 650-nm long-pass emission filter in the emission path)

the light excitation, however the scaffold stabilizes the Ag clusters and prevents photodissociation characteristic of Ag_n observed in the gas phase.⁵⁶⁻⁵⁹ A large excited state charge separation most likely produces the large oscillator strength, fast radiative lifetime, and Raman-enhancing ability of these few-atom NC's. While all these processes might contribute to this unique large Raman enhancement, more work needs to be done to clarify the role of fluorescent silver clusters in the SERS effect.

5.2.9 Anti-Stokes Raman spectra of red emitting silver clusters

Not only Stokes Raman scattering but also strong anti-Stokes Raman scattering was observed in the presence of fluorescent silver clusters. Anti-Stokes spectra of dendrimer/peptide encapsulated red emitting silver nanoclusters were collected through a short pass dichroic mirror and emission filter (SP620 nm) under HeNe laser excitation with 20~500 W/cm². Strong single molecule anti-Stokes Raman emission spectra with intensity intermittency was clearly observed from both dendrimer and peptide encapsulated red emitting silver clusters (shown in Figure 5.2.9). The cross section of anti-Stokes Raman scattering is around 10⁻¹⁷ cm²/s based on the rough estimation of relative intensity ratio between fluorescence and anti-Stokes scattering from the same silver cluster. Such AS-Raman transitions exhibit intensities comparable to standard single molecule fluorescence from the best organic dyes.

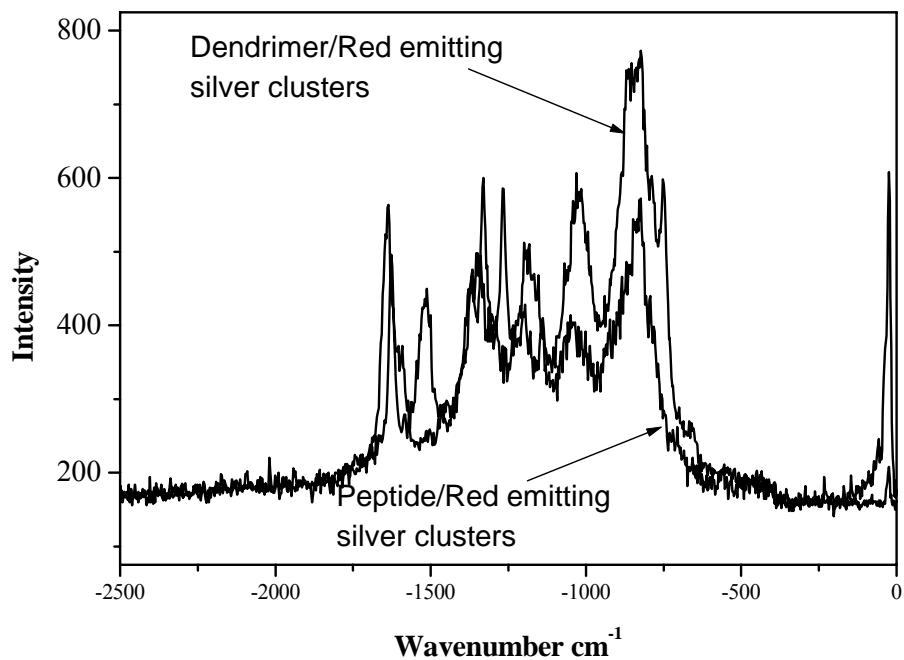


Figure 5-2-9 Room temperature bulk antistokes Raman spectra from dendrimer/peptide encapsulated red emitting silver clusters. Taken in a confocal geometry (633-nm HeNe laser excitation, 633 NB laser excitation filter and 545 LP filter on the excitation path. 620-nm short-pass emission filter on the emission path and dispersed by a 300-mm path length monochromator),

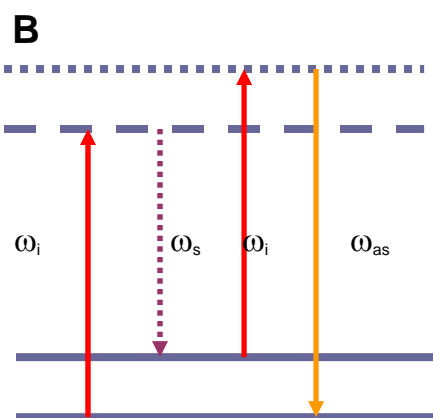
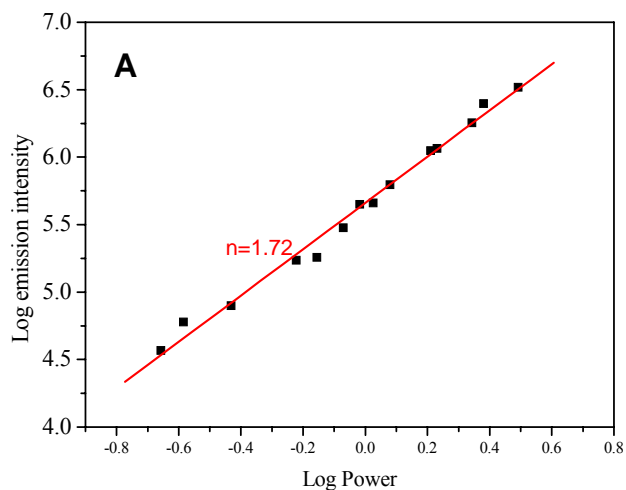


Figure 5-2-10 Power dependence and a possible mechanism of enhanced antistokes Raman scattering observed by red emitting silver clusters. (A) Correlation of the excitation power and antistokes Raman Scattering Intensity. Nearly quadratic power dependence suggests that a possible scheme (B) for the observed large antistokes Raman scattering cross section, may be the population pumping of excitation vibrational states by spontaneous Raman. The first excited state is first populated through the large Stokes Raman scattering process instead of direct thermal population and then excited to higher vibrational states of the excited electronic state, which then relaxes to the ground vibrational states through antistokes Raman scattering.

According to simple Raman theory, the relative intensity ratio between Stokes and antistokes scattering is governed by a Boltzmann distribution. However, the unusually large antistokes/stokes intensity ratio ($1/10\sim 30^{\text{th}}$) suggested the first excited vibration state is greatly populated beyond thermal population.⁶⁰ To understand this unusual large antistokes, the correlation of excitation power with intensity of antistokes Raman scattering was investigated. Strong quadratic power dependence was observed (Figure 5.2.10A). Such correlation was also observed early by Kneipp et al.⁶⁰ but with 100-fold higher excitation power. This large antistokes enhancement effect may be attributed to the population pumping of excitation vibrational states by spontaneous Raman (Figure 5.2.10B), however, the detailed mechanism involving the silver clusters is still not fully understood. Such surprisingly high antistokes Raman scattering cross section offers a unique opportunity to use these red emitting silver clusters in true background-free windows for biological imaging by measuring emission at higher energy than the excitation.

5.3 Conclusion

Incredibly photostable, water-soluble silver nanoclusters ($\text{Ag}_2\sim\text{Ag}_8$) have been successfully created in dendrimers or peptide through direct photoreduction in ambient conditions. Such silver nanodots are quite stable in both solution and films and are readily observed on the single molecule level with weak mercury lamp excitation. Strong coupling between the ground and excited state is responsible for their ultra brightness. Red emitting silver clusters can be selectively created by using HeNe laser photoactivation. Large Stokes and antistokes Raman scattering were also

observed from these few atom fluorescent silver clusters. With synthetic control of dendrimer and peptide attachment, such simple nanomaterials are likely to find applications as biological labels, thereby making single molecule studies much more widely accessible without expensive laser sources. Unique Raman scattering enhancement by fluorescent silver clusters offers new insights into the nature of SM-Stokes and antistokes Raman. The extremely high oscillator strength and the intense photoactivated emission of these sub-nm silver clusters present new possibilities for use as biological labels with various scaffolds giving single molecule sensitivity, possible correlated with true chemical information.

5.4 References

1. Lu, H. P., Xun, L. Y. & Xie, X. S. Single-molecule enzymatic dynamics. *Science* 282, 1877-1882 (1998).
2. Dickson, R. M., Cubitt, A. B., Tsien, R. Y. & Moerner, W. E. On/off blinking and switching behaviour of single molecules of green fluorescent protein. *Nature* 388, 355-358 (1997).
3. Hu, D. H., Yu, J. & Barbara, P. F. Single-molecule spectroscopy of the conjugated polymer MEH-PPV. *J. Am. Chem. Soc.* 121, 6936-6937 (1999).
4. Bartko, A. P. Deciphering spatially heterogeneous polymer dynamics using single molecule microscopy. *Thesis* (2002).
5. Murray, C. B., Norris, D. J. & Bawendi, M. G. Synthesis and Characterization of Nearly Monodisperse Cde (E = S, Se, Te) Semiconductor Nanocrystallites. *J. Am. Chem. Soc.* 115, 8706-8715 (1993).
6. Bruchez, M., Moronne, M., Gin, P., Weiss, S. & Alivisatos, A. P. Semiconductor nanocrystals as fluorescent biological labels. *Science* 281, 2013-2016 (1998).
7. Ozin, G. A. & Huber, H. Cryophotoclustering Techniques for synthesizing very small naked silver cluster Ag_n of known size(where n=2-5). The molecular metal cluster-bulk metal particle interface. *Inorg. Chem.* 17, 155-163 (1978).
8. Knight, W. D. et al. Electronic Shell Structure and Abundances of Sodium Clusters. *Phys. Rev. Lett.* 52, 2141-2143 (1984).
9. Baetzold, R. C. Study of Evaporated Metal Nuclei by Auger-Spectroscopy. *J. Appl. Phys.* 47, 3799-3803 (1976).

10. Baetzold, R. C. & Mack, R. E. Electronic Properties of Metal Clusters. *J. Chem. Phys.* 62, 1513-1520 (1975).
11. Baetzold, R. C. Molecular-Orbital Description of Catalysis by Metal Clusters. *Journal of Catalysis* 29, 129-137 (1973).
12. Baetzold, R. C. Calculated Properties of Metal Aggregates .2. Silver and Palladium. *J. Chem. Phys.* 55, 4363-& (1971).
13. Fedrigo, S., Harbich, W. & Buttet, J. Optical-Response of Ag₂, Ag₃, Au₂, and Au₃ in Argon Matrices. *J. Chem. Phys.* 99, 5712-5717 (1993).
14. Harbich, W., Fedrigo, S. & Buttet, J. The optical absorption spectra of small silver clusters (n = 5- 11) embedded in argon matrices. *Chem. Phys. Lett.* 195, 613-617 (1992).
15. Felix, C. et al. Fluorescence and excitation spectra of Ag-4 in an argon matrix. *Chem. Phys. Lett.* 313, 105-109 (1999).
16. Felix, C. et al. Ag-8 fluorescence in argon. *Phys. Rev. Lett.* 86, 2992-2995 (2001).
17. Chen, W. et al. Photostimulated luminescence of AgI clusters in zeolite-Y. *J. Appl. Phys.* 83, 3811-3815 (1998).
18. Chen, W., Joly, A. G. & Roark, J. Photostimulated luminescence and dynamics of AgI and Ag nanoclusters in zeolites. *Phys. Rev. B* 65, art. no.- 245404 (2002).
19. Peyser, L. A., Vinson, A. E., Bartko, A. P. & Dickson, R. M. Photoactivated fluorescence from individual silver nanoclusters. *Science* 291, 103-106 (2001).

20. Peyser, L. A., Lee, T. H. & Dickson, R. M. Mechanism of Ag-n nanocluster photoproduction from silver oxide films. *J. Phys. Chem. B* 106, 7725-7728 (2002).
21. Zheng, J. & Dickson, R. M. Individual water-soluble dendrimer-encapsulated silver nanodot fluorescence. *J. Am. Chem. Soc.* 124, 13982-13983 (2002).
22. Chen, M. C. et al. Effect of silver-nanoparticle aggregation on surface-enhanced Raman scattering from benzoic acid. *Phys. Rev. B* 51, 4507-4515 (1995).
23. Hildebrandt, P. & Stockburger, M. Surface enhanced Raman Spectroscopy of Rhodamine 6G adsorbed on colloidal silver. *J. Phys. Chem.* 88, 5935-5944 (1984).
24. Emory, S. R. & Nie, S. M. Near-field surface-enhanced Raman spectroscopy on single silver nanoparticles. *Anal. Chem.* 69, 2631-2635 (1997).
25. Lei, C. C. et al. Enhanced Raman scattering from crystal violet and benzoic acid molecules adsorbed on silver nanocrystals. *Mater. Sci. Eng. B* B32, 39-45 (1995).
26. Schneider, S., Grau, H., Halbig, P., Freunscht, P. & Nickel, U. Stabilization of silver colloids by various types of anions and their effect on the surface-enhanced Raman spectra of organic dyes. *J. Raman Spectrosc.* 27, 57-68 (1996).
27. Kneipp, K. et al. Single-molecule detection of a cyanine dye in silver colloidal solution using near-infrared surface-enhanced Raman scattering. *Appl. Spectrosc.* 52, 175-178 (1998).
28. Fleischmann, M., Hendra, P. J. & McQuilan, A. J. Raman spectra of pyridine at a silver electrode. *Chem. Phys. Lett.* 26, 163-166 (1974).

29. Creighton, J. A. *Surface-enhanced Raman scattering* (eds. Chang, R. K. & Furtak, T. E.) 243-273 (Plenum Press, New York, 1982).
30. Seki, H. *Surface enhanced Raman scattering of pyridine on different silver surfaces* *J. Chem. Phys.* 76, 4412-4418 (1982).
31. Chang, R. K. & Furtak, T. E. (eds.) *Surface-Enhanced Raman Scattering* (Plenum Press, New York, 1981).
32. Campion, A. & Kambhampati, P. Surface-enhanced Raman scattering. *Chem. Soc. Rev.* 27, 241-250 (1998).
33. Moskovits, M. Surface-enhanced Raman spectroscopy. *Rev. Mod. Phys.* 57, 783-824 (1985).
34. Metiu, H. & Das, P. The electromagnetic theory of surface enhanced raman scattering. *Ann. Rev. Phys. Chem* 35, 507-535 (1984).
35. Haynes, C. L. & Van Duyne, R. P. Plasmon-sampled surface-enhanced Raman excitation spectroscopy. *J. Phys. Chem. B* 107, 7426-7433 (2003).
36. Ferraro, J. R. *Introductory Raman Spectroscopy* (Academic Press, Boston, 1994).
37. Garrell, R. L. & Pemberton, J. E. (eds.) *Fundamentals and Applications of Surface Raman Spectroscopy* (VCH Publishers, Deerfield Beach, FL, 1994).
38. Osawa, M., Matsuda, K., Yoshii, K. & Uchida, I. Charge transfer resonance Raman process in surface-enhanced Raman scattering from p-aminothiophenol adsorbed on silver. *J. Phys. Chem.* 98, 12702 (1994).
39. Otto, A. in *Light Scattering in Solids IV* (eds. Cardona, M. & Gundtherodt, G.) 289-418 (Springer-Verlag, Berlin, 1984).

40. Otto, A., Mrozek, I., Grabhorn, H. & Akemann, W. Surface -enhanced Raman scattering. *J. Phys. Condens. Mater.* 4, 1143-1212 (1992).
41. Persson, B. N. J. On the theory of surface enhanced Raman scattering. *Chem. Phys. Lett.* 82, 561-565 (1981).
42. Kneipp, K. et al. Single molecule detection using surface-enhanced Raman scattering (SERS). *Phys. Rev. Lett.* 78, 1667-1670 (1997).
43. Nie, S. M. & Zare, R. N. Optical detection of single molecules. *Annu. Rev. Biophys. Biomolec. Struct.* 26, 567-596 (1997).
44. Jiang, J., Bosnick, K. A., Maillard, M. & Brus, L. E. Single molecule raman spectroscopy at the junctions of large Ag nanocrystals. *J. Phys. Chem. B* 107, 9964-9972 (2003).
45. Bartko, A. P. & Dickson, R. M. Three-dimensional orientations of polymer-bound single molecules. *J. Phys. Chem. B* 103, 3053-3056 (1999).
46. Rabin, I., Schulze, W. & Ertl, G. Absorption spectra of small silver clusters Ag-n ($n \geq 3$). *Chem. Phys. Lett.* 312, 394-398 (1999).
47. Mihalcea, C., Buchel, D., Atoda, N. & Tominaga, J. Intrinsic fluorescence and quenching effects in photoactivated reactively sputtered silver oxide layers. *J. Am. Chem. Soc.* 123, 7172-7173 (2001).
48. Crooks, R. M., Zhao, M. Q., Sun, L., Chechik, V. & Yeung, L. K. Dendrimer-encapsulated metal nanoparticles: Synthesis, characterization, and applications to catalysis. *Acc. Chem. Res.* 34, 181-190 (2001).
49. Ottaviani, M. F., Valluzzi, R. & Balogh, L. Internal Structure of Silver-Poly(amidoamine) Dendrimer Complexes and Nanocomposites. *Macromolecules* 35, 5105-5115 (2002).

50. Zheng, J., Stevenson, M. S., Hikida, R. S. & Van Patten, P. G. Influence of pH on dendrimer-protected nanoparticles. *J. Phys. Chem. B* 106, 1252-1255 (2002).
51. Varnavski, O., Ispasoiu, R. G., Balogh, L., Tomalia, D. & Goodson, T. Ultrafast time-resolved photoluminescence from novel metal- dendrimer nanocomposites. *J. Chem. Phys.* 114, 1962-1965 (2001).
52. Bonacic'-Koutecky, V., Veyret, V. & Mitric', R. Ab initio study of the absorption spectra of Ag_n (n=5-8) clusters. *J. Chem. Phys.* 115, 10450-10460 (2001).
53. Ozin, G. A. & Huber, H. Cryophotoclustering techniques for synthesizing very small, naked silver clusters Ag_n of known size (where n=2-5). The molecular metal cluster-bulk metal particle interface. *Inorg. Chem.* 17, 155-163 (1978).
54. Capadona, L. P. et al. Nanoparticle-free single molecule antistokes Raman spectroscopy. *Phys. Rev. Lett.* 94, 058301 (2005).
55. Henglein, A., Mulvaney, P. & Linnert, T. Chemistry of Ag_n Aggregates in Aqueous-Solution - Nonmetallic Oligomeric Clusters and Metallic Particles. *Faraday Discuss.*, 31-44 (1991).
56. Tiggesbaumker, J., Koller, L., Lutz, H. O. & Meiwes-Broer, K. H. Giant Resonances in Silver-Cluster Photofragmentation. *Chem. Phys. Lett.* 190, 42-47 (1992).
57. Ho, J., Ervin, K. & Lineberger, W. C. Photoelectron spectroscopy of metal cluster anions L Cu_n⁻, Ag_n⁻ and Au_n⁻. *J. Chem. Phys.* 93, 6987-7002 (1990).
58. Hild, U. et al. Time-resolved photofragmentation of stored silver clusters Ag_n⁺ (n=8-21). *Physical Review A* 57, 2786-2793 (1998).

59. Spasov, V., Lee, T. H., Maberry, J. P. & Ervin, K. M. Measurement of the dissociation energies of anionic silver clusters (Ag_n^- , $n=2-11$) by collision-induced dissociation. *J. Chem. Phys.* 110, 5208-5217 (1999).

60. Kneipp, K. et al. Population pumping of excited vibrational states by spontaneous surface-enhanced Raman scattering. *Phys. Rev. Lett.* 76, 2444-2447 (1996).

CHAPTER 6

Future work and outlook

Research on fluorescent noble metal nanoclusters has attracted more and more interest recently. Great progress has made in this field toward the fundamental understanding of size-dependence of these noble metals as well as developing the applications in bioscience and information technologies. However, as demonstrated in this thesis, a lot of work involving in better understanding and manipulating their properties needs to be done. A part of future work is listed as following:

I. Separation of fluorescent metal clusters. Since fluorescence of small noble metal nanoclusters is strongly size-dependent, separation of different fluorescent noble metal clusters will be very important to their applications. Due to well-defined molecular weights of dendrimers, dendrimer encapsulated noble metal clusters are not only easily characterized with ESI mass spectrometry but also allow relatively easy separation with different techniques such as HPLC, electrophoresis. This work should be carried on.

II. Controlling emission from fluorescent silver clusters and its mechanism. This thesis has demonstrated a simple method to create red emitting silver clusters and only red emitting silver nanoclusters were created within dendrimer/peptide

scaffolds. The mechanism for the growth of fluorescent silver clusters within organic scaffolds is still not clear and needs more investigation.

III. Correlation of emission energy of silver cluster with its size. Multicolored fluorescent silver clusters have been created within dendrimer /peptides matrices, however, quantitative correlation of emission energy with cluster size is still unclear and needs more effort to study. The studies will not only be very important to understand the photophysical properties such as ultrafast lifetimes and photostability of silver clusters but also offer opportunities to resolve the long time mystery that whether d-sp interband transitions involve into emission from silver clusters.

IV. Mechanisms for the large Raman enhancement by the fluorescent silver clusters. Strong Stokes and anti-stokes Raman scattering were observed from dendrimer/peptide encapsulated fluorescent silver clusters. However, the mechanisms for such enhancement need to be intensively investigated. Several possible processes related with small silver clusters have been mentioned in this thesis, which might have some connections with the observed large Raman enhancement. More detailed studies along this line might be helpful to eventually understand origin of Raman enhancement.

V. Emission mechanism of luminescent gold nanoparticles. Luminescent gold nanoparticles have photophysical properties different to those of small fluorescent gold nanoclusters and nonluminescent plasmonic gold nanoparticles. The quantitative explanation for the observed emission is missing and needs to be further investigated.

APPENDIX

List of publications

1. **Zheng, J.**; Dickson R.M.; “Observation of photon antibunching from gold clusters at room temperature” **2005** (In preparation)
2. **Zheng, J.**; Gao P.X., Wang, Z.L., Tzeng, Y.-L., Dickson, R.M “Biocompatible peptide encapsulated luminescent gold nanoparticles” **2005** (In Preparation)
3. **Zheng, J.** Capadona, L.A., Dickson R.M. “Fluorescent noble metal clusters” **2005** (In preparation)
4. Lee T-H., **Zheng J.**, Gonzalez J.I., Dickson R.M., Single molecule optoelectronics, *Accounts of Chemical Research* (in press)
5. **Zheng, J.**; Zhang C.W., Dickson, R.M. Highly fluorescent, water soluble, size-tunable, gold quantum dots, *Physical Review Letters*, **2004** , **93**, **077402**
6. Peyser L. **Zheng J.** Lee T-H. Dickson R.M. Nanoparticle-free single molecule antistokes Raman spectroscopy *Physical Review Letters* **2005**, **94**, **058301**
7. Petty, J. T.; **Zheng, J.**; Hud, N. V.; Dickson, R. M.; DNA-Templated Ag Nanocluster Formation; *J. Amer. Chem. Soc.*, **2004**, 126(16); 5207-5212
8. **Zheng, J.**; Petty, J. T.; Dickson, R. M.; High Quantum Yield Blue Emission from Water-Soluble Au₈ Nanodots *J. Amer. Chem. Soc.*, **2003**, 125, 7780-7781. (Highlights of recent literature in *Science*, **300**, 1849, 2003)

9. **Zheng, J.**; Dickson, R. M.;, Individual Water-Soluble Dendrimer-Encapsulated Silver Nanodot Fluorescence *J. Amer. Chem. Soc.*,**2002** 124, 13982-13983
10. Mehta, A.; Kumar, P.; Dadmun, M. D.; **Zheng, J.**; Dickson, R. M.; Thundat, T.; Sumpter, B. G.; Barnes, M. D.; Oriented Nanostructures from Single Molecules of a Semiconducting Polymer: Polarization Evidence for Highly Aligned Intramolecular Geometries *Nano Lett.*; **2003**; 3(5); 603-607.
11. Kumar, P.; Mehta, A.; Dadmun, M. D.; **Zheng, J.**; Peyser, L.; Bartko, A. P.; Dickson, R. M.; Thundat, T.; Sumpter, B. G.; Noid, D. W.; Barnes, M. D.; Narrow-Bandwidth Spontaneous Luminescence from Oriented Semiconducting Polymer Nanostructures *J. Phys. Chem. B.* ; (Communication); **2003**; 107(26); 6252-6257
12. Mehta, A.; Kumar, P.; **Zheng, J.**; Dickson, R. M.; Barnes, M. D.; Oriented luminescent nanostructures from single molecules of conjugated polymers Mater. Soc. Symp. Proc. **2003**, 771, 301-305

VITA

Jie Zheng was born in 1972 in Sichuan, China. Strongly influenced by his parents, he chooses chemistry as his career. He graduated from Inner Mongolia University with honors. After studying and conducting research in different areas in China and USA, he joined Dr. Dickson's group in 2002. Since then, he has been working on fluorescent noble metal nanoclusters for his Ph.D dissertation research. He graduated from Georgia Institute of Technology with honors and will continue pursuing his lifetime goal – making contributions to science with his maximum efforts.